# STOCHASTIC DYNAMICAL SYSTEM IDENTIFICATION

# APPLIED TO COMBUSTOR STABILITY MARGIN ASSESSMENT

A Thesis
Presented to
The Academic Faculty

by

Helio de Miranda Cordeiro

In Partial Fulfillment
of the Requirements for the Degree
Doctor of Philosophy in the
School of Aerospace Engineering

Georgia Institute of Technology
May 2009

# STOCHASTIC DYNAMICAL SYSTEM IDENTIFICATION

# APPLIED TO COMBUSTOR STABILITY MARGIN ASSESSMENT

Approved by:


Dr. Ben T. Zinn, Advisor
School of Aeroespace Engineering
*Georgia Institute of Technology*

Dr. Massimo Ruzzene
School of Aeroespace Engineering
*Georgia Institute of Technology*

Dr. Timothy C. Lieuwen
School of Aeroespace Engineering
*Georgia Institute of Technology*

Dr. Aldo A. Ferri
College of Mechanical Engineering
*Georgia Institute of Technology*

Dr. J. V. R. Prasad
School of Aeroespace Engineering
*Georgia Institute of Technology*


Date Approved: Dec 12, 2008

# ACKNOWLEDGEMENTS

I would like to express my deepest appreciation to my advisor, Dr. Ben T. Zinn, whose support and enlightening discussions have been a major contribution in the successful completion of my graduate study. I would also like to acknowledge my gratitude to Dr. Timothy C. Lieuwen, Dr. J. V. R. Prasad, Dr. Massimo Ruzzene, and Dr. Aldo A. Ferri, for kindly providing their expert guidance by serving as my committee members. I shall thank Dr. Eugene Lubarsky, Dr. Aleksander Bibik and Dmitry Sherbiky for the development of the experimental setup, and their help with the data acquisition and processing techniques. I would like to thank all my colleagues, in special John Crane, Jaecheol Kim, Santosh Schanbogue, and Baris Sen for their help during the qualifying exams preparation.

I would like to acknowledge the Air Force Office for Scientific Research (AFOSR) for the sponsorship of the experimental part of this research, and the Brazilian Council of Technological Research and Development (CNPq) for providing me my scholarship.

I would like to thank Dr. Demetrio B. Netto from National Institute of Space Research (INPE-SP), and Dr. Luis Fernando F. Silva from Pontiphical Catholic University (PUC-Rio) for their support and friendship. I knew I could count on you.

Finally, I would like to thank my parents and express my deepest love and gratitude to my wife, Edlaine Cordeiro, and daughter, Beatriz Cordeiro, for all the encouragement, motivations, and happiness that they have brought to my life.

# TABLE OF CONTENTS

ACKNOWLEDGEMENTS …….. iii

LIST OF TABLES …… iv

LIST OF FIGURES …… v

LIST OF SYMBOLS AND ABBREVIATIONS ……..vi

SUMMARY ……..vii

CHAPTER 1: INTRODUCTION ……... 1

1.1 Motivation ……6

1.2 Outline ……...9

CHAPTER 2: BACKGROUND AND LITERATURE REVIEW ……10

2.1 Thermoacoustic Instabilities ……10

2.1.1 Combustion Instabilities in Liquid Rocket Engines ……..14

2.2 Dynamical System Identification ……16

2.2.1 Dynamical Model ……..…16

2.2.2 System Identification Techniques ……19

2.3 System Identification Applied to Combustors ……..……...22

CHAPTER 3: EXPERIMENTAL DATA ...…...……...30

3.1 The Liquid Rocket Engine Combustor Simulator....…….30

3.2 Test Procedure and Preliminary Analysis ……34

3.2.1 Natural Modes in the Combustor ……..39

CHAPTER 4: THERMOACOUSTIC MODEL ……48

4.1 Nonlinear Wave Equation ……..…….49

4.2 Modal Expansion ……..……... 52

4.3 The Forcing Functions ……. 57

4.3.1 Explicit Terms ……..57

4.3.2 Flame Dynamics …….. 67

4.4 The Finite-dimension Model …….. 69

4.5 Numerical Simulations ……71

CHAPTER 5: LINEAR SYSTEM APPROXIMATION…….. ……74

5.1 State-Space Representation ……75

5.2 Stochastic Subspace Identification ……..79

5.2.1 The Block Hankel Matrix ……81

5.2.2 The Projections ……82

5.2.3 The Kalman States ……... 82

5.2.4 Estimation of the System Matrices …….. 83

5.2.5 The Model Order ……. 84

5.2.6 Implementation ……..… 86

5.3 SSI-DATA Accuracy ……..…… 88

5.3.1 Parametric Noise Investigation ……....93

5.4 Experimental Results and Operational Stability Margin …… 95

CHAPTER 6: NONLINEAR SYSTEM IDENTIFICATION ……100

6.1 Heat Release Dynamics Model …….……. 100

6.1.1 NARX Model …… 102

6.1.2 Model Identification ……...… 106

6.2 Nonlinear Dynamical Model …….. 113

6.3 System Identification Technique ……..114

6.3.1 Maximum Likelihood Estimation ……..……114

6.3.2 Extended Kalman Filter …… 116

6.4 System Identification Accuracy ……118

6.5 Experimental Results ……..…..121

6.5.1 Analysis of Initial Values for Parameters ……. 122

6.5.2 Model for Identification ……127

6.5.3 Model Parameters Estimation ……128

6.5.4 Analysis of the Results …….. 142

6.5.5 Operational Stability Margin Assessment …… 146

CHAPTER 7: CONCLUSIONS AND FUTURE WORK …. …..……. 150

APPENDIX A: Equations of Motion ……..154

REFERENCES ……158

# LIST OF TABLES


Page

Table 3.1: Wave numbers for transverse modes of oscillations in cylindrical … 41

Table 3.2: Theoretically estimated natural frequencies in the LRECS 42

Table 5.1: Effect of parametric noise upon damping ratio estimates. 94

Table 6.1: Comparison between actual and estimated values of the system … 119

Table 6.2: Theoretical values of the parameters $A_{mij}$ and $B_{mij}$ for coupling… 124

Table 6.3: Thermodynamical and kinematic flow properties and combustor … 126

# LIST OF FIGURES


Page

Figure 1.1: Examples of pressure oscillation time-history. 2

Figure1. 2: Schematic example of a stability map. 4

Figure 1.3: Dependence of the pressure oscillations amplitude upon… 4

Figure 1.4: Bifurcation diagram depicting behavior for the system (Equation 1.2). 7

Figure 1.5: Schematic of the developed approach. 8

Figure 2.1: Schematic of the feedback mechanism driving combustion instabilities. 12

Figure 2.2: Dependence of oscillatory energy flux upon pressure... 13

Figure 2.3: Schematic of a spring-mass-damper system. 17

Figure 3.1: Schematic of the liquid rocket engine combustor simulator 31

Figure 3.2: Details of the "smart" fuel injectors. 32

Figure 3.3: Dependence of the spray pattern upon changes in the control … 32

Figure 3.4: Stability map for the LRE combustor simulator for increasing … 36

Figure 3.5: Time history of: a) control parameter $K$ ; b) dynamic pressure… 37

Figure 3.6: Dependence of the RMS pressure oscillations upon changes in… 38

Figure 3.7: Cross amplitude spectral density from sensors $FOP_1'$ and $P_1'$ during… 43

Figure 3.8: Cross amplitude spectral density from sensors $FOP_1'$ and $P_1'$ during… 44

Figure 3.9: Cross amplitude spectral density from sensors $FOP_1'$ and $P_1'$ during… 45

Figure 3.10: Cross amplitude spectrogram sensors $FOP_1'$ and $P_1'$ during… 46

Figure 5.1: Example of the model order selection plot in MATLAB® 87

Figure 5.2: Effect of the number of data points in damping estimation for… 90

Figure 5.3: Effect of the SNR in damping estimation for simulated frequency… 91

Figure 5.4: Dependence of the estimated frequencies upon changes in simulated… 92

Figure 5.5: Dependence of the estimated damping ratio upon changes in simulated... 93

Figure 5.6: Dependence of the estimated damping ratio of the quarter wave… 97

Figure 5.7: Dependence of the estimated damping ratio of the first tangential … 98

Figure 6.1: Input-output modeling of the heat release dynamics. 101

Figure 6.2: Time history of: a) dynamic pressure oscillations; and b) heat release … 109

Figure 6.3: Amplitude spectral density from sensors: a) $FOP_1'$; and b) $P_1'$, during… 110

Figure 6.4: Comparison between the measured output and the predicted values... 111

Figure 6.5: System response: a) time history; and b) amplitude spectral density. 120

Figure 6.6: Dependence of the estimated parameters from non-linear gasdynamics... 130

Figure 6.7: Dependence of the estimated modal frequencies upon changes in swirl… 136

Figure 6.8: Dependence of the estimated modal damping ratios upon changes in… 138

Figure 6.9: Dependence of the estimated model parameters related to the source… 139

Figure 6.10: Dependence of the estimated model parameters $c_{1L}$ and $c_{1T}$ upon … 140

Figure 6.11: Dependence of the estimated model parameters $b_1$ upon changes … 141

Figure 6.12: Dependence of the estimated model parameters $b_2$ and $b_3$ upon … 143

Figure 6.13: Stationary heat release profiles at different values of swirl flow ratio … 145

Figure 6.14: Comparison between the predicted modal amplitude via continuation …148

# LIST OF SYMBOLS AND ABBREVIATIONS

$\mathbf{O}$ = matrix of zeros $\in \Re^{N \times N}$

$\mathbf{A_c}$ = continuous-time state space matrix

$\mathbf{A}_d$ = discrete time state space matrix

$\overline{a}$ = speed of sound

$\mathbf{C_c}$ = continuous time observation matrix

$\mathbf{C}_d$ = discrete time observation matrix

$e_j(t)$ = noise from measurements in the *j-th* sensor

$f_i$, $\tilde{f}_i$ = frequency of mode *"i"*, effective frequency of mode *"i"*

$(F_i)^{\mathrm{NLGD}}$ = non-linear contributions due to gas dynamics

$(F_i)^{\mathrm{NL}}_{\mathrm{Comb}}$ = non-linear contributions due to combustion

$\mathbf{I}$ = identity matrix $\in \Re^{N \times N}$

$k$ = discrete time instant

$K$ = swirl flow ratio

$L$ = number of pressure sensors

$N$ = number of excited modes

$p'$ = unsteady dynamic pressure oscillations

$p'_j$ = unsteady dynamic pressure measured by the *j-th* sensor

$\dot{Q}'$ = unsteady rate of heat release

$R$ = gas Constant/ radius of the combustor

$R_{XX}$ = auto-correlation function

$\mathbf{R_{k|k-1}}$ = matrix of covariances

$T_{ad}$ = adiabatic temperature

$\mathbf{u}_k$ = discrete unknown excitations $\in \Re^{2N\times 1}$

$u(t)$ = dynamical system input

$\mathbf{v}$ = mode shapes matrix $\in \mathrm{C}^{N\times 2N}$

$\mathbf{x}_k$ = discrete state vector $\in \Re^{2N\times 1}$

$\mathbf{x}_t = \mathbf{x}(t)$ = continuous state vector $\in \Re^{2N\times 1}$

$\mathbf{w}_k$ = discrete measurement noise $\in \Re^{L\times 1}$

$\mathbf{y}_k$ = sampled output vector $\in \Re^{L\times 1}$

$\mathbf{y}_t = \mathbf{y}(t)$ = continuous output vector $\in \Re^{L\times 1}$

$y(t)$ = dynamical system output

$\mathbf{Y_{k-1}}$ = vector of sampled outputs

$\Delta t$ = sampling time

$\eta_i$ = pressure oscillation amplitude of mode *"i"*

$\phi$ = equivalence ratio

$\gamma$ = ratio of specific heat

$\kappa_{mn}, \nu_{mn}$ = wave numbers of transverse acoustic modes

$\lambda_i$ = continuous-time complex eigenvalues

$\mathbf{\Lambda}_d$ = diagonal matrix of discrete-time eigenvalues $\in \mathrm{C}^{2N\times 2N}$

$\mu_i$ = discrete-time complex eigenvalues

$\psi_i$ = mode shape of mode "*i*"

$\boldsymbol{\theta}$ = vector of model parameters

$\sigma^2$ = variance

$\omega_i$, $\tilde{\omega}_i$ = angular frequency of mode *"i"*, effective angular frequency of mode *"i"*

$\xi_i$, $\tilde{\xi}_i$ = damping ratio of mode *"i"*, effective damping ratio of mode *"i"*

$\zeta_i(t)$ = multiplicative noise related to displacement of mode *"i"*

$\zeta_i^v(t)$ = multiplicative noise related to velocity of mode *"i"*

$\Pi_1, \Pi_2$ = control parameters (operational conditions)

$\amalg_{L\times N}$ = matrix of ones

$\Xi_i(t)$ = additive noise of mode *"i"*

$\Psi$ = eigenvectors matrix $\in \mathrm{C}^{2N\times 2N}$

AR = Autoregressive Model

CMIF = Complex Mode Indication Function

CASD = Cross Amplitude Spectral Density

EMA = Experimental Modal Analysis

EKF = Extended Kalman Filter

FFT = Fast Fourier Transform

IV = Instrument Variable

LRE = Liquid rocket engine

LRECS = Liquid rocket engine combustor simulator

ML = Maximum Likelihood

NARX = Non-linear Autoregressive Model with Exogenous Input

ODE = Ordinary Differential Equation

OMA = Operational Modal Analysis

PDE = Partial Differential Equation

PEM = Predictor Error Method

PMT = Photo-multipliers

PP = Peak-picking

RD = Random Decrement

RMS = Root Mean Squared

SDE = Stochastic Differential Equation

SDDE = Stochastic Delay Differential Equation

SID = System Identification

SL = Stability Limit

SM = Stability Margin

SNR = Signal-to-Noise Ratio

SSI = Stochastic Subspace Identification

SSI-DATA = Data Driven Stochastic Subspace Identification

SVD = Singular Value Decomposition

ZMWN = Zero Mean White Noise

ZOH = Zero Order Hold

# SUMMARY

Thermoacoustic instabilities in propulsion systems have been studied for more than sixty years, but their understanding and control still represent challenging problems. One of the outstanding issues regarding thermoacoustic instabilities is the estimation of the operational stability margin of a combustor; that is, its susceptibility to instability. More specifically, when a laboratory scale combustor or a full scale combustor is operating stably, the operators generally do not know where the stability boundary is. Therefore, there is a need for a methodology which would be able to estimate the operational stability margin in those cases. This research developed a new approach for the determination of combustor's stability margin, which is based on three steps.

The first step consists of a gray-box modeling in which a thermoacoustical model for the combustor is derived from first principles. The dynamical system behavior depends on the values of the model parameters. The second step consists in applying modern System Identification techniques to experimental data in order to validate the model and estimate its parameters. The application of these techniques to experimental data under different operating conditions allowed us to determine the functional dependence of the model parameters upon changes in a control parameter.

Finally, the third step consists in using that functional dependence to predict the response of the system at different operating conditions and, ultimately, estimate its stability margin. The methodology was applied to determine the stability margin of a laboratory scale combustor. The results indicated that a low-order stochastic non-linear model including two excited modes has been identified and the combustor operational stability margin could be estimated by applying a continuation method.

# CHAPTER 1

# INTRODUCTION

Detrimental combustion instabilities have been excited in many types of propulsion and power generation systems for a long time and considerable research has been performed in order to understand and develop solutions to the problem. While significant progress has been made in this field, the current understanding of the fundamental processes that control the performance and stability of such systems remains limited. The reason for that is the complexity of the several simultaneous and interacting physicochemical processes which control these instabilities; e.g., injection, atomization, vaporization, mixing, chemical reactions, expansion, and acoustics.

In general, combustion instability assumes the form of pressure oscillations whose amplitudes have a tendency to grow and settle down to a certain limit value (i.e., limit cycle amplitude) due to the feedback coupling between two dominant processes: acoustics and oscillatory combustion process heat release. That explains the term thermoacoustic instability. Depending on how those processes interact with each other, the limit cycle amplitude can vary from small to very large values. Since small amplitude pressure oscillations are always present and usually do not represent a problem to the combustor, one assumes that a combustor is unstable when the pressure oscillations amplitude exceeds a certain threshold value. This value is somewhat arbitrary and varies from one combustor to another. Above the threshold limit performance degradation or even catastrophic system failure can occur. Figure 1.1 shows examples of measured pressure oscillations for stable and unstable operations. The black line indicates the

threshold limit, which in this case was set at $p' = 0.2$ psi (RMS) and the green and red lines indicate the measured RMS pressure.

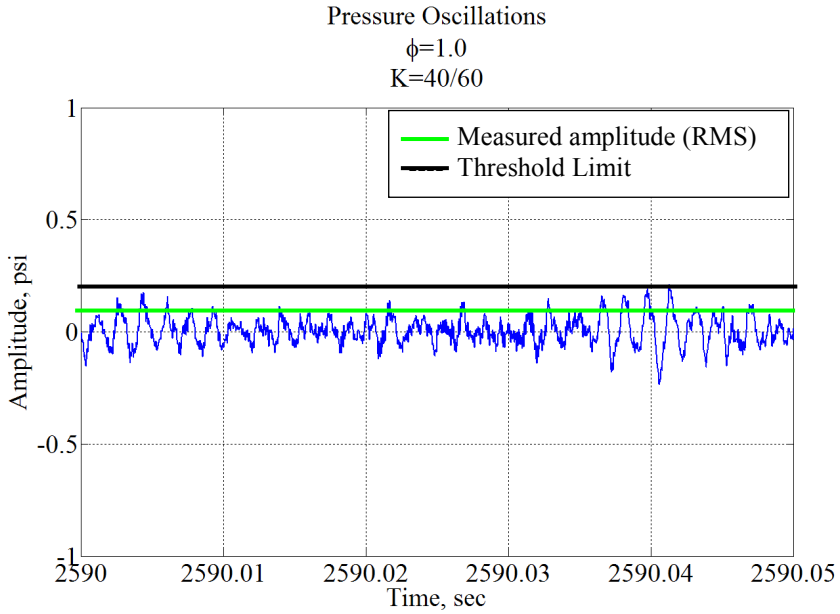


a) stable operation: measured amplitude (RMS) below the threshold limit.

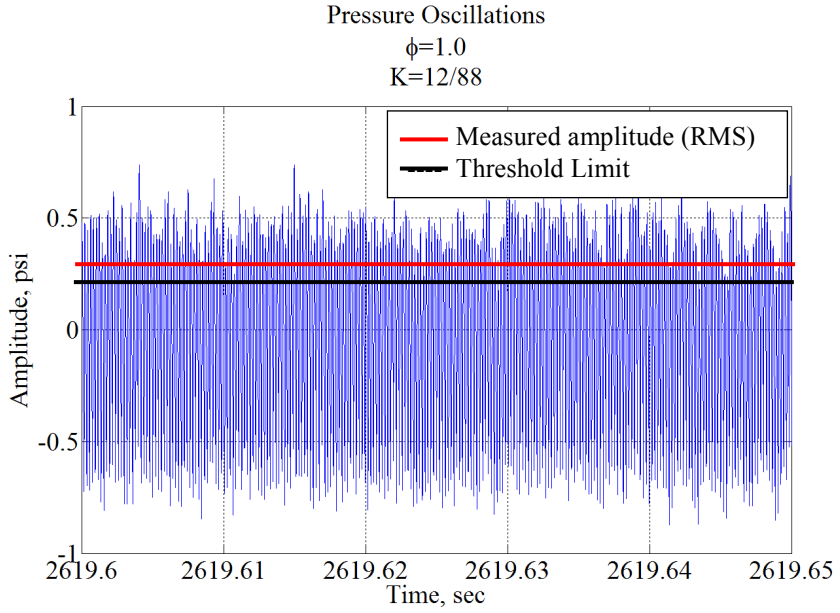


b) unstable operation: measured amplitude (RMS) above the threshold limit.

Figure 1.1: Examples of pressure oscillation time-history.

Changes in instability behavior are typically attributed to combustor modifications or changes in operating conditions. For a particular combustor one wants to know which operating conditions lead to unstable behavior; i.e., under which operating conditions the amplitudes of the oscillations exceed the specified threshold limit. In this sense, we are dealing with operational stability in this thesis and it is usual to determine the stability characteristics of the combustor from experiments. In these experiments the pressure oscillations amplitude are measured as a function of changes in a pair of control parameters in operating conditions (e.g., equivalence ratio, fuel/oxidizer temperature, etc.). The results are used to build operational stability maps that indicate for which pairs of control parameters the combustor is stable, unstable or marginally stable (in the case of occurrence of hysteresis).

Figure 1.2 shows an example of a operational stability map. In order to plot it, one starts by measuring the pressure oscillations amplitude for a situation in which the control parameter $\Pi_2$ is varied from $\Pi_{2,I}$ to $\Pi_{2,V}$ while the control parameter $\Pi_1$ remains constant (see the blue line in Figure 1.2). Figure 1.3 shows typical observed changes in the pressure oscillations amplitude (root mean squared) as we move along the blue line.

Since the threshold for the operational stability ( $P'_{SL}$ ) has been set, the value of the changing control parameter at the stability limit can be estimated ( $\Pi_{2,SL}$ ). Repeating this procedure for different values of $\Pi_1$, the stability map can be determined. For example, in Figure 1.2, the gray region represents the range of operating conditions for which the combustor is unstable. The dashed red line represents the operational stability boundary.

Since the operational stability map has been plotted, one can estimate the operational stability margin (SM) of the combustor at a given operational condition. The

operational stability margin of the combustor is defined herein as its "distance" from the operational stability boundary (SB) or its susceptibility to instability. Therefore, looking at Figure 1.3, one can say the operational stability margin of the combustor decreases when moving from point I to point II ($|\Pi_{2,SL}-\Pi_{2,I}| > |\Pi_{2,SL}-\Pi_{2,II}|$). Since the operational stability limit was known in this example, the determination of the operational stability margin was simple.

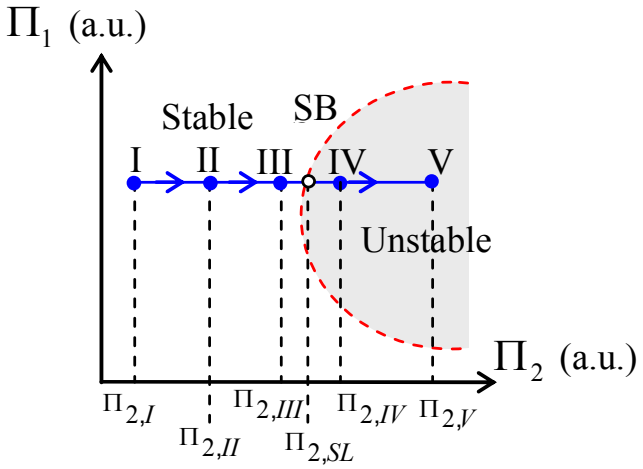


Figure 1.2: An example of a stability map.

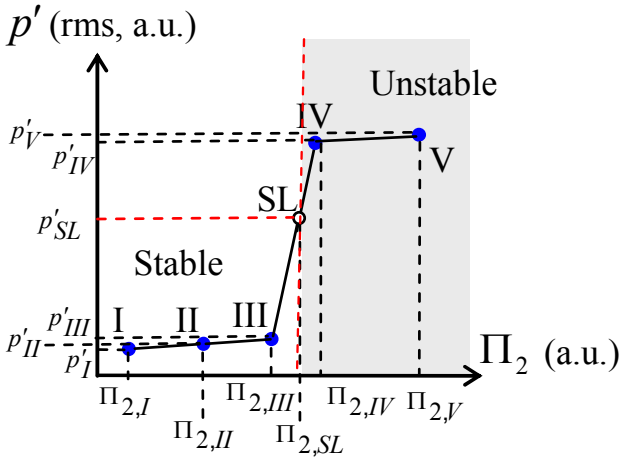


Figure 1.3: Dependence of the pressure oscillations amplitude upon changes in control parameter $\Pi_2$.

This research addresses a usual situation in which we do not know where the operational stability limit is. That is the case when we just started performing tests to determine the stability map. We start at point I in Figure 1.2 and move along the blue line towards point III. Even though a slight increase in the pressure oscillations amplitude can sometimes be noticed as we move from point I to III, it does not provide any information about the location of the stability limit. A further increase in the parameter from $\Pi_{2,III}$ to $\Pi_{2,IV}$ was accompanied by a large "jump" in the amplitude of the oscillations, as shown in Figure 1.3. As a consequence the threshold limit ( $p'_{SL}$ ) was exceeded characterizing the onset of the combustion instability.

As mentioned before, since combustion instabilities often excite pressure oscillations that damage the combustor, unstable operation must be prevented; that is, operation must be restricted to the left side of the operational stability boundary in Figure 1.2. Therefore, it is necessary to develop a methodology for determining the operational stability boundary of a combustor under different operating conditions without getting into the combustion instability zone. Due to the behavior shown in Figure 1.3, it is clear that the simple extrapolation of the data points I, II and III, will not provide a good estimate for the stability limit ( $\Pi_{2,,SL}$ ). That is, the amplitude of the pressure oscillations is not a simple function of the control parameter $\Pi_2$.

In fact, the measured pressure oscillations represent the response of a dynamical system (the combustor in this case). We anticipate that the system response it is not only a simple function of the control parameter $\Pi_2$. It is determined by a more complex expression, usually in the form of differential equations; that is

$$p' = f(\ddot{p}', \dot{p}', p', \boldsymbol{\theta} = \boldsymbol{\theta}(\Pi_2)) \tag{1.1}$$

where the right-hand-side of Equation (1.1) represents the dynamical model of the system and $\boldsymbol{\theta}(\Pi_2)$ is the vector of model parameters which are functions of $\Pi_2$.

### 1.1 Motivation

The motivation for this work is the problem of estimating the operational stability margin of a combustor from experimental data before the onset of the instability. Therefore, the main goal of this research is to develop a methodology that would enable one to achieve this goal. We should keep in mind that a combustor is a dynamical system and, as such, can be represented by a mathematical model, as shown in Equation (1.1). In general, this mathematical model has parameters, $\boldsymbol{\theta}(\Pi_2)$, whose values determine the overall dynamical behavior of the system.

For example, consider the dynamical system represented in polar form by the following system of differential equations (mathematical model)[1]

$$\begin{aligned} \dot{r} &= r(\mu - 0.2r^6 + 1.05r^4 - 1.3r^2) \\ \dot{\theta} &= \omega \end{aligned} \tag{1.2}$$

where $r$ is the amplitude of the system response, $\omega$ is the angular frequency of the oscillatory response, and $\mu$ is the only varying model parameter. The qualitative behavior of this system is described in Figure 1.4, which shows the dependence of the amplitude of the system response, $r$, upon $\mu$ as it increases from -0.6 to 1.2.

Figure 1.4 shows that for negative values of $\mu$, the origin ($r = 0$) is a stable focus and the only steady-state solution. As $\mu$ passes from negative to positive values, the origin loses stability and a stable limit cycle appears. The amplitude of the limit cycle oscillations increases as $\mu$ increases. When $\mu$ reaches a value of 0.48 there is a sudden jump to a larger-amplitude limit cycle. Increasing the value of $\mu$ from 0.48 to 1.2 causes

a slight increase in the amplitude of the limit cycle. At $\mu=0$ we say the system has undergone a supercritical Hopf bifurcation and at $\mu=0.48$ it has undergone a saddle-node bifurcation[1].

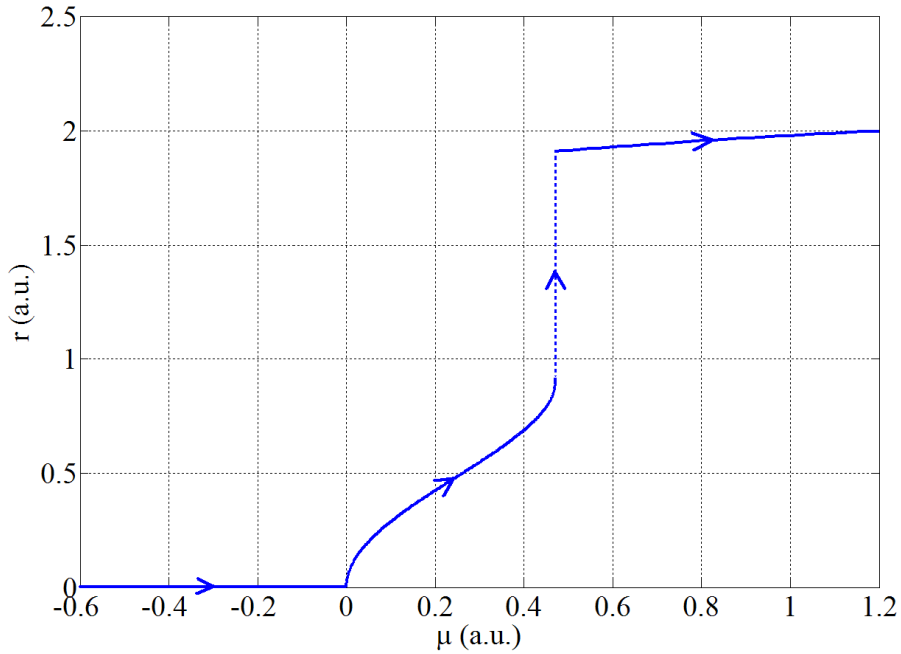


Figure 1.4: Bifurcation diagram depicting behavior for the system in Equation (1.2).

Now, comparing Figures 1.3 and 1.4 we can see the remarkable similarity between the typical behavior of a combustor system and the behavior of the system defined by Equation (1.2). Therefore, one can conclude that the behavior of the combustor system (and ultimately its stability boundary) could be predicted via bifurcation diagram (or even numerical simulations), if a proper mathematical model for the system and the dependence of the model parameters upon changes in operating conditions are provided. The mathematical model must be validated and its parameters

obtained from the available experimental data. The more effective way to achieve this is by a combination of analytical, numerical and experimental tools.

Therefore, this research introduces a new approach for assessing the operational stability margin of a combustor which depends on three basic steps. The first step in the developed approach is the derivation of a mathematical model which describes the combustion system dynamics. In general, the model has parameters which vary as we change the operational conditions. The second step in the approach is to extract the maximum amount of information from a set of experimental data, in order to validate/invalidate the assumed model and estimate its parameters. This process is called *System Identification* (SID). Since the model and the dependence of the model parameters upon changes in operating conditions have been determined applying modern SID techniques, the third (and last) step consists of estimating the operational stability boundary (or stability margin) by using bifurcation diagrams and/or numerical simulations. The approach is described schematically in Figure 1.5 and it will be further detailed in the following chapters.

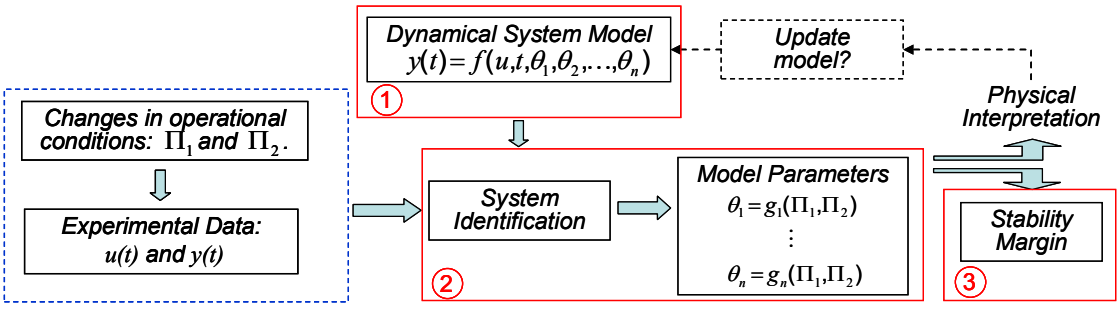


Figure 1.5: Schematic of the developed approach.

The main motivation for using system identification techniques in this study is the significant progress in the field during the past decade, mainly propelled by improvements in computational resources. The currently available SID techniques can handle a variety of dynamical system models from deterministic linear systems to stochastic nonlinear systems. That allows a much more realistic representation of the combustion system dynamics as will be shown later.

## 1.2 Outline

The outline of this thesis is as follow. An introduction to thermoacoustic instabilities with basic concepts and literature review, some background on SID techniques, and a literature review on parameters estimation in combustion systems are presented in Chapter 2. In Chapter 3 we present the experimental setup, the collected data, and a preliminary analysis of the stability characteristics of the combustor to which the SID techniques will be applied. In Chapter 4 we present the derivation of a thermoacoustic model for the combustor along with the theory about stochastic differential equations behind the numerical algorithm used to simulate the behavior of the thermoacoustic model. In Chapter 5, we assume that under stable operation the combustor behaves as a linear stochastic system. Then an appropriate SID technique is implemented, its accuracy is verified, and experimental results are shown. The more complex and realistic non-linear stochastic system is approached in Chapter 6 in which a SID technique is implemented, its accuracy and issues involving initial values of the non-linear model parameters are investigated, and experimental results are presented. Finally, the conclusions and recommendations for future works are described in Chapter 7.

# CHAPTER 2

# BACKGROUND AND LITERATURE REVIEW

The objective of this chapter is to provide the reader with some background in the combustion instabilities and dynamical system identification matters. Besides a literature review, the fundamental concepts of these subjects are covered. Thus, the information presented in this chapter provides an introduction to the subjects to be covered in Chapters 4, 5, and 6. In particular, Section 2.4 presents a review of some pioneering works in the field of dynamical system identification related to combustion systems and their main results are analyzed.

## 2.1 Thermoacoustic Instabilities

The chronology of combustion instabilities in propulsion systems indicates that this problem has been studied for more than sixty years since such instabilities were first observed in liquid and solid propellant in the late 1930 and earlier 1940[2]. Therefore, a comprehensive review of the literature on this subject will be not presented here. Nevertheless, to provide some necessary background information, important pioneering works in the field of combustion instabilities are cited, in particular those related to combustion instabilities in liquid rocket engines (LRE), as well as a brief review of the fundamental concepts of thermoacoustic instabilities.

Under unstable operation, a combustor can experience intense vibrations which can damage primary structures and sensitive electronic components such as the guidance system. Other detrimental effects such as unexpected forces and torques, system performance degradation, and increased heat transfer which can be sufficient to destroy

portions of a combustion system can also occur. Therefore, there exist urgent needs for investigations that can elucidate the mechanisms that lead to such detrimental oscillations and find means to prevent them.

The literature shows that combustion-driven acoustic oscillations were recognized by Higgins[3] in 1802. It was observed that sound could be produced while setting a flame inside an open-ended or closed-ended tube. The phenomenon was called the "singing flame". Years later, Rijke[4], a professor of physics at the University of Leyden in the Netherlands, invented the Rijke tube by placing a hot gauze in the lower half of open-ended vertical tube. It was observed that the sound coming out of the tube was more or less intense depending on the placement of the heat-source at different locations. Even though there was no flame in his experiment, a heat source was determinant in producing the sound.

The physical explanation of how the sound was stimulated was only presented in the book of Lord Rayleigh[5] published in 1878. According to Rayleigh's observations when flames are confined in a combustion chamber, combustion instability may be driven by a positive feedback between acoustics and heat release oscillations, which is typically referred to as a thermoacoustic loop. That was the basis for the formulation of the principle that came to be known as Rayleigh's criterion. An updated review of several investigations about Rijke tube up to 1993 was presented by Raun et al.[6], which contains a good number of references, useful comments on the observed physical behavior, and experimental confirmation of Rayleigh's Criterion.

The thermoacoustic loop is described in Figure 2.1. It shows the feedback mechanism which is a necessary condition for combustion instabilities to occur in any

combustor. An oscillation in a given flow or thermodynamic variable drives oscillations in heat release. Due to the flame dynamics, there exists a coupling between the unsteady heat release and acoustic pressure oscillations which propagate away from the combustion region exciting the flow variable and completing the positive feedback loop.

The underlying flame-acoustics interaction, responsible for the coupling between the unsteady heat release and acoustic pressure oscillations, is complex and can be regarded as an energy transfer problem[7]. In this sense, there exist processes responsible for adding oscillatory energy to the system and other responsible for the dissipation of such energy. The amplitude of the oscillations will grow or decay depending on the balance between those addition/removal processes.

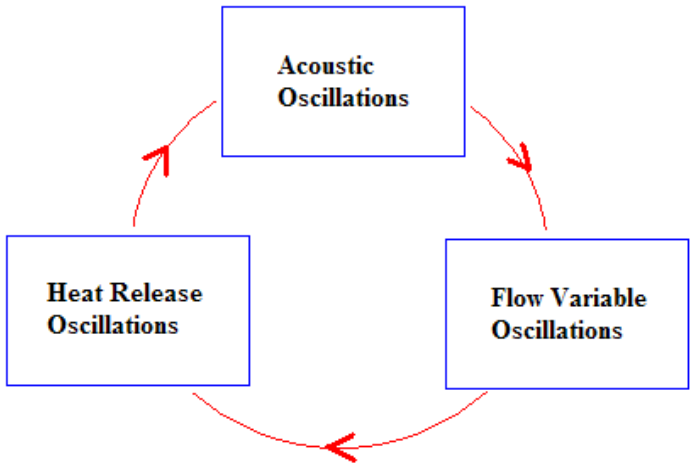


Figure 2.1: Schematic of the feedback mechanism driving combustion instabilities.

Once a thermoacoustic loop has been initiated, energy is added to the initial disturbance at each cycle and its amplitude would grow indefinitely. However, in real combustion systems this unbound growth is never observed. The reason for this is the

fact that combustion chambers are nonlinear dynamical systems in which the nonlinearities appear in the dependence of the oscillatory energy added to the system, $E_{add}(A)$, and the energy dissipated by the system, $E_{dis}(A)$, upon the amplitude of the oscillations.

Figure 2.2 shows examples of curves representing the dependence of the added and dissipated energy upon changes in the amplitude of the oscillations. It shows that when the amplitude of the oscillations in the system is larger than a certain threshold value, $A_{cr}$, the system starts operating in positive feedback loop; i.e., the energy added to the system is larger than the energy dissipated by it. The amplitude increases until it reaches a certain amplitude value, $A_{LC}$, where the system's energy losses equal its energy gains and the instability amplitude saturates at the system's limit cycle oscillations.

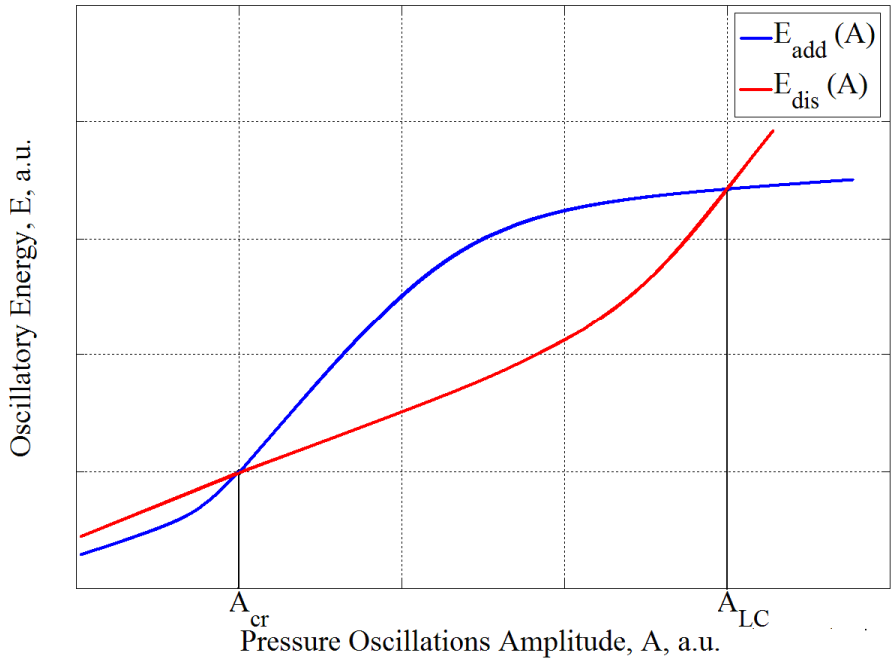


Figure 2.2: Dependence of oscillatory energy flux upon pressure oscillations amplitude.

Clearly, the processes responsible for initiating and saturating the instability are important in determining the overall behavior of an unstable combustion system. This is true for every type of combustion system; however, to better understand and develop methods to control and/or prevent combustion instabilities in a specific combustor system, we need to considerably increase the level of driving feedback loop shown in Figure 2.1. Following the definitions by Williams[8] we can classify combustion instabilities as system instabilities, which means a system-sensitive phenomenon. They are not determined by the characteristics of only one component of the combustor system, but by the complex interactions of all relevant components of the system. Although the source of acoustic oscillations is the heat release from combustion, the properties of these oscillations are determined by the design and dimensions of the combustion system, reactants properties, operating pressure, etc. Consequently, the causes of instability and its consequences vary from one system to another.

### 2.1.1 Combustion Instabilities in Liquid Rocket Engines

Since in the rest of this work we will be dealing with combustion instabilities in a liquid rocket engine combustor simulator (LRECS), the main aspects of this problem need to be discussed. The first theoretical and experimental approach to the problem was presented by Crocco[9],[10] who suggested that a time-dependent sensitive time-lag could be incorporated into the driving mechanism of the oscillations. Some years later, Crocco and Cheng[11] presented a comprehensive monograph whose discussions regarding the subject were, however, limited to small amplitude oscillations; that is, linear behavior.

During the course of the above discussed investigations it was very common to experience phenomena which could not be explained by means of the proposed linear

theories. As a matter of fact, as already mentioned, the phenomenon of combustion instabilities must involve nonlinearities. As mentioned by Culick[12], sources of nonlinearities can be attributed to processes such as gasdynamics and combustion. This indicates that the conclusions and predictions obtained by applying linear approaches should be used carefully. There is clearly a need for a theory that can handle the nonlinear regime (finite oscillations).

To address the nonlinear regime, the work at NASA Research Center[13] presented a completely new approach in which the nonlinear equations describing the unsteady flow in a chamber were numerically integrated in time, and an arbitrary disturbance was provided as the initial conditions. If the disturbance increased with time the system was unstable and vice-versa. In this sense, the result depended on the particular disturbance used, so that it was not a general approach.

Searching for such general approach, a series of investigations performed at Princeton proposed to apply the time-lag concept to the non-linear problem. Experimental results with gas-fueled rockets had shown the presence of discrete sharp-fronted waves, suggesting a model that could be analyzed using the method of characteristics. The investigations by Sirignano[14] and Sirignano and Crocco[15] dealt with the motion of a shock wave in a rocket chamber having planar combustion concentrated at the head end and terminating in a choked nozzle. While still analyzing the same problem but, importantly, without a shock wave Zinn[16] applied a Galerkin method to calculate the results for a class of three-dimensional unsteady motions with the flow taken to be irrotational. As for most of the Princeton analyses of combustion instabilities, the time-lag model was assumed for the unsteady combustion response. All of those works

introduced tools and methodologies which have since been commonly applied to address the problem of nonlinear instabilities.

All the references cited so far form the background of thermoacoustic instabilities in a liquid rocket engine (LRE). We should also mention that a more comprehensive review of combustion instabilities in LREs can be found in the compilation by Harrje and Reardon[17] and more recently in Culick and Yang[2]. In fact, it is expected that all the information gathered throughout reading the cited literature should be useful in formulating/proposing a mathematical model which captures the physical behavior of the combustor of a LRE. This will be accomplished later in this thesis in more details.

The validity of the proposed mathematical model will be verified applying dynamical system identification techniques, which relate the mathematical model to the available experimental data as shown in Figure 1.5.

## 2.2 Dynamical System Identification

### 2.2.1 Dynamical Model

The first and perhaps the most important step in dynamical system identification (SID) problems is the definition of a dynamical model for the system, sometimes referred to as model structure. The behavior of the system depends on the values of the dynamical model parameters. When applying SID techniques, we are ultimately interested in estimating the model parameters from the measured experimental data.

Figure 2.3 shows a schematic of a simple dynamical system. The spring-mass-damper represent the dynamical system that is excited by the arbitrary force, $u(t)$, which is called the input to the system. Assume that the spring is linear with spring constant $k$

and the damper is represented by a linear viscous dashpot model with coefficient of viscous damping $c$. The response of the system is given by the displacement, $y(t)$, which is called the output of the system. The question now is how the input and the output data are related and how one can express this relationship.

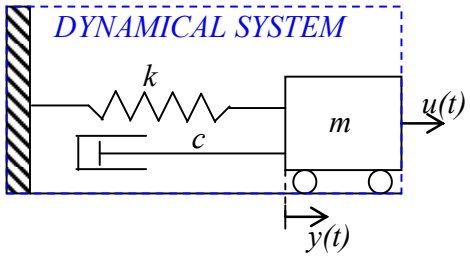


Figure 2.3: Schematic of a spring-mass-damper system.

Dynamical models describe the relationship between one or more measured input signals, *u(t)*, and one or more measured output signals, *y(t)*. The data can be measured in the time-domain or frequency-domain and have single or multiple inputs and outputs. In real systems, there may be additional inputs that you cannot measure or control, which affect the system's output. Such unmeasured inputs are called disturbances or noise. In a broad sense, a dynamical model is a "box" containing the mathematical laws that link the inputs to the outputs.

For the system shown in Figure 2.3, applying the Newton's Second Law we can derive the following equation

$$m\ddot{y}(t)+c\dot{y}(t)+ky(t)=u(t) \tag{2.1}$$

Equation (2.1) represents the dynamical model of the forced spring-mass-damper system. This type of model is called a "white-box" model since it was derived directly from first

principles. In general, white-box models are typically described by ordinary differential or difference equations and the model parameters have a physical meaning. As mentioned before, the physical behavior of the system is controlled by the values of the model parameters *m*, *c*, and *k*.

In the given example, the dynamical model could be easily obtained from Newton's Second Law. However, in many problems the physical modeling is a complex procedure, or even there are no first principles available to derive a model. For these cases, the alternative is to use the so called "black-box" models (a common situation in economics and physiology).

As an example, consider the case where we want to build a model of how the voltage applied to an electric heater affects the temperature in a room. The voltage is the input, $u(t)$, and the temperature is the output, $y(t)$. A white-box modeling would require writing down all equations relating to the power of the heater, heat transfer, heat convection, unknown heat transfer coefficients, etc. Instead, the following black-box model (in general a difference equation) provides good results[18]

$$y(t)=\theta_1 y(t-1)+\theta_2 y(t-2)+\theta_3 u^2(t-1)+\theta_4 u^2(t-2) \tag{2.2}$$

where $\theta_1$, $\theta_2$, $\theta_3$, and $\theta_4$ are the model parameters. In contrast with the previous case, parameters of black-box models have no physical meaning. The model represented by Equation (2.2) indicates the temperature at a discrete-time instant "*t*" depends on the temperature at the previous discrete-time instants "$t-1$" and "$t-2$" as well as the square of the voltage at those same instants.

When the system can be assumed linear, the task of finding a black-box model is not difficult. However, when the system is non-linear, we usually need some sort of

physical insight into the system to find a good black-box model. In the previous example, one knows that it is the heater power rather than the voltage that causes the temperature to change. That is why the input is squared in the model. When this happens we have a "gray-box" model (neither completely black nor white) that is obtained from a semi-physical modeling approach. We also consider gray-box when the structure of the model is built on physical grounds but has a certain number of parameters to be estimated from measured data.

Deriving a model for the system may be hard. However, some things should be considered to make the task easier. First, we must analyze the available data since non-linear effects can often be detected immediately. Second, when working with black-box models, a good engineering principle is to *try simple things first*; i.e., one should try linear models or models with small number of parameters. Then transition from simpler to more complex models until a valid one is found. Finally, we should always look into the physics of the problem and try some gray-box model. In this thesis, we had the opportunity to apply all of those principles.

### 2.2.2 System Identification Techniques

Since the data were collected and a dynamical model was proposed, the next step is the implementation of a system identification technique which provides a means of estimating unknown parameters in the dynamic model equations, as a product of the process of minimizing the difference between measured and predicted responses. When the experimental data are used in the time or covariance domain, the identification methods are usually based upon least squares, maximum likelihood and related techniques. When the data are used in the frequency domain, one is usually concerned

with spectral estimates and fitting models to the estimated frequency response characteristics.

In general, these techniques consist on numerical algorithms with a particular set of functions which are called according to the task to be performed in the identification procedure. However, the availability, complexity and accuracy of the techniques to be implemented depend upon such issues as the presence of non-linearities in the dynamical model and the availability of the input data, that is, whether the excitation force is measured or not.

When both input and output signals are measured, the system is called deterministic. For deterministic systems, several SID techniques are available to estimate the parameters of both linear and non-linear models. The results for linear models are much more accurate and the frequency domain techniques are more easily implemented. When dealing with non-linear models the computational time to estimate the parameters is larger and the accuracy decreases. A good review and comparison of the many different techniques can be found in the books of Bendat[19] (frequency domain data) and Ljung[20].

When the input signal is not measured, SID techniques are available only if the input can be assumed to be a stochastic process; i.e., the system is stochastically excited. Additionally, if the dynamical model is linear the procedure of system identification is known as Operational Modal Analysis (OMA) in Civil Engineering and Experimental Modal Analysis (EMA) in Mechanical Engineering. The identified model is in this case a *modal model* consisting of eigenfrequencies, damping ratios, and mode shapes.

The first SID methods applied to OMA were based on the frequency domain data. According to the chronological application we had the Peak Picking[21] (PP) and the Complex Mode Indication Function[22] (CMIF) spectrum-driven methods. Then, covariance-driven methods such as the Random Decrement[23] (RD) and the Instrument Variable[20] (IV) were developed. More recently, the Stochastic Subspace Identification (SSI) methods both covariance-driven[24] and data-driven[24] were developed. The data-driven SSI will be discussed in details later in this thesis. Comprehensive reviews about system identification applied to stochastically excited linear systems can be found in the book of Ljung[20] and the thesis of Peeters[25].

System identification of stochastically excited non-linear systems is a much harder problem. The application of spectral methods to stochastic linear models is already a non-linear optimization problem. Therefore, their use for stochastic non-linear models is not advised. There are a number of suitable time domain methods available in the literature for solving such non-linear problems[20]. The general approach in those time domain methods applies the *Predictor Error Method* (PEM) along with the *Extended Kalman Filter* (EKF) to estimate the model parameters.

Recently, energy-based identification techniques have been proposed by Roberts and Vasta[26],[27] and Rudinger and Krenk[28] to estimate parameters of stochastically excited non-linear dynamical systems. The methods rely on the fact that for lightly damped systems the energy envelope of the system response is approximately a one-dimensional Markov process. Then, expressions relating the model parameters and properties of the energy envelope of the system response can be obtained analytically.

Finally, analyzing the energy envelope provided by the experimental data and fitting it to the analytical expressions allows the estimation of the model parameters.

### 2.3 System Identification Applied to Combustors

In this section, we present some previous works in which combustors were considered dynamical systems represented mathematically by a thermoacoustical model and analyzed by system identification techniques to validate the model and estimate its parameters. These studies are presented here in increasing order of model complexity; that is, from linear to non-linear models.

Use of system identification in the field of combustor dynamics seems to have been developed first by Russian groups as part of their development of liquid rocket engines, beginning perhaps as early as the 1950s but certainly in the 1960s[29]. Thus, we begin this review with the investigation performed by Karmalita and Furletov[30]. Based on a mathematical model derived from first principles, they assumed that, under stable operation, the combustor chamber behaves as a stochastically excited linear dynamical system, represented by a system of uncoupled second order stochastic differential equation. The dynamics of each mode of the pressure oscillations is described by

$$\ddot{X} + 2\tilde{\xi}\tilde{\omega}\dot{X} + \tilde{\omega}^2 X = F(t) \tag{2.3}$$

where $\tilde{\xi}$ is an effective modal damping ratio, $\tilde{\omega}$ is an effective modal angular frequency and $F(t)$ is the stochastic forcing assumed a white noise. A formal derivation of Eq. (2.3) will be presented later in this thesis.

The idea was to estimate the model parameters (i.e., effective modal frequencies and damping ratios) from the measured dynamic pressure data and to use the estimated

modal damping ratios (or decrement) as a measure of the stability margin. However, the methodology implemented by them did not estimate the parameters of the gray-box model directly. Using results from time-series analysis[31], a second order system formulated in continuous time may be represented in the discrete time by a second order Autoregressive model - AR(2) - given by

$$X(t)=a_1X(t-1)+a_2X(t-2)+\varepsilon(t) \tag{2.4}$$

where $X(t)$ represents the system response at the discrete time "$t$", $X(t-1)$ and $X(t-2)$ the response at discrete-times "$t-\Delta t$" and "$t-2\Delta t$", respectively, $\Delta t$ equal to the sampling time, $a_1$ and $a_2$ are the autoregressive parameters and $\varepsilon(t)$ is a time series of independent Gaussian distributed noise with zero mean and variance $\sigma_\varepsilon^2$.

Equation (2.4) is a black-box model so that one needs to find, if any, a relationship between the AR model parameters, $a_1$ and $a_2$, and the modal parameters of interest $\tilde{\xi}$ and $\tilde{\omega}$. In order to establish this relationship Karmalita and Furletov[30] proposed the following approach. Multiply Equation (2.4) by $X(t-\Gamma\Delta t)$ and take the expected value of the resultant expression in both sides of equation. In the left-hand-side we have the definition of the autocorrelation function $R_{XX}(\Gamma)=E[X(t)X(t-\Gamma\Delta t)]$. Similarly, in the right-hand-side one obtains terms involving autocorrelation functions as shown below

$$\begin{aligned}
&E[X(t)X(t-\Gamma\Delta t)]=E[a_1X(t-\Delta t)X(t-\Gamma\Delta t)\\
&+E[a_2X(t-2\Delta t)X(t-\Gamma\Delta t)]+E[\varepsilon(t)X(t-\Gamma\Delta t)]\\
&\Rightarrow R_{XX}(\Gamma)=a_1E[X(t)X[t-(\Gamma-1)\Delta t]]\\
&+a_2E[X(t)X[t-(\Gamma-2)\Delta t]]+E[\varepsilon(t)X(t-\Gamma\Delta t)]\\
&\Rightarrow R_{XX}(\Gamma)=a_1R_{XX}(\Gamma-1)+a_2R_{XX}(\Gamma-2)+E[\varepsilon(t)X(t-\Gamma\Delta t)]
\end{aligned} \tag{2.5}$$

Since the value of $\varepsilon(t)$ is independent of $X(t-\Gamma\Delta t)$, the last term in the right-hand-side vanishes and we end up with

$$R_{XX}(\Gamma)=a_1R_{XX}(\Gamma-1)+a_2R_{XX}(\Gamma-2) \tag{2.6}$$

Equation (2.6) is known as Yule-Walker equation and the AR parameters are estimated by implementing an algorithm based on least squares minimization to fit the autocorrelation function of the experimental data to the AR model. Box and Jenkins[32] have shown that the following expression can be used to estimate the autocorrelation function in Equation (2.6)

$$R_{XX}(\Gamma)=\frac{(|a_1|/a_1)^{\Gamma}(\sqrt{-a_2})^{\Gamma}\sin(\tilde{\omega}\tau+\theta)}{\sin\theta} \tag{2.7}$$

where $\tan\theta=\frac{1-a_2}{1+a_2}\tan\tilde{\omega}$

In the other hand, taking the Fourier transform of Equation (2.3) and applying the Wiener-Khinchin relations, one can derive the following expression for the autocorrelation function of $X(t)$ [21]

$$R_{XX}(\Gamma)=\frac{\exp(-\tilde{\xi}\tilde{\omega}\Gamma)\sin[(\tilde{\omega}\sqrt{1-\tilde{\zeta}^2})\Gamma+\phi)]}{\sin\phi} \tag{2.8}$$

Thus, comparing Equations (2.7) and (2.8) and assuming that the value of the damping is small (i.e., $\tilde{\xi}^2<<1$), the following expressions were derived

$$\tilde{\omega}=\frac{1}{\Delta t}\cos^{-1}\left(\frac{a_1}{2\sqrt{-a_2}}\right) \tag{2.9}$$

$$\tilde{\xi}=-\frac{1}{2\tilde{\omega}\Delta t}\ln(-a_2) \tag{2.10}$$

A similar approach was presented by Lieuwen[33]. The combustor was also assumed to behave as a stochastically excited linear system in which the dynamics of the excited modes of oscillation were given by Equation (2.3), so that the autocorrelation function can be calculated from Equation (2.8). Therefore, for a lightly damped mode, the autocorrelation oscillates at a frequency very close to $\tilde{\omega}$ and its envelope decays as $\exp(-\tilde{\xi}\tilde{\omega}\Gamma)$. The envelope of the oscillatory autocorrelation was calculated via its Hilbert transformation. After the envelope of the oscillatory signal has been determined, the effective modal damping ratio can be estimated from the best fit of the equation $\exp(-\tilde{\xi}\tilde{\omega}\Gamma)$ by implementing a least squares minimization procedure.

The main problem with all methods based on the autocorrelation function of the output data is the presence of significant noise in the signal. Even if we use a bandpass filter to filter the data around a center frequency, the filtered data will still contain noise (band limited white noise theoretically). Bendat and Piersol[21] have shown that a correction term needs to be added to the expression of the autocorrelation function in Equation (2.8) to address this noise issue. Then the corrected expression is given by

$$R_{XX}(\Gamma) = \frac{\exp(-\tilde{\xi}\tilde{\omega}\Gamma)\sin[(\tilde{\omega}\sqrt{1-\tilde{\zeta}^2})\Gamma + \phi)]}{\sin\phi} + GB\left(\frac{\sin\pi B\Gamma}{\pi B\Gamma}\right)\cos(\tilde{\omega}\Gamma) \qquad (2.11)$$

where $G$ is the power of the band limited white noise (assumed constant) and $B$ is the filter bandwidth.

Equation (2.11) shows that while the frequency of the oscillations of the autocorrelation function does not change, its decay will change depending on the values of $G$ and $B$. The results also showed that the accuracy of both presented methods became problematic as the combustor was becoming unstable. Additionally, these techniques

required that one excited mode in the output signal be analyzed at a time; i.e., the output signal had to be filtered and the characteristics of the filter can affect the accuracy of the estimates.

The linear system assumption was also adopted in the work of Murugappan et al[34]. They considered that in a neighborhood of the limit-cycle oscillations, a linear model combining the acoustics, heat release, fuel injector and solid state relay into a lumped transfer function, could accurately predict the combustor response and therefore could be used to design a controller that reduces the amplitude of these oscillations.

Due to the need for fast and accurate model estimations, the following black-box deterministic model was proposed

$$y(t) = \sum_{i=1}^{n_a} a_i y(t - i\Delta t) + \sum_{i=n_k}^{n_k+n_b} b_i u(t - i\Delta t) + \sum_{i=0}^{n_c} c_i \varepsilon(t - i\Delta t) \tag{2.12}$$

where $u(t)$ is input to the system given by the voltage to the fuel injector, $y(t)$ is the output given by the dynamic pressure oscillations, $\varepsilon(t)$ is a white noise, $\Delta t$ is the sampling time, $n_a$, $n_b$, $n_c$, and $n_k$ represent the number of poles, zeros, order of noise and delay in the combustor, respectively, and $a_i$, $b_i$, and $c_i$ are the model parameters.

The model parameters estimation was performed by implementing a two-level iteration scheme. The first level of iteration is in the parameter space, defined as $\boldsymbol{\theta}=[a_1,\ldots,a_{n_a},b_1,\ldots,b_{n_b},c_1,\ldots,a_{n_c}]$ for a given dimension space defined by $D=[n_a,n_b,n_c,n_k]$, whereas the second level of iteration is in the dimension space. The results confirmed that a deterministic linear black-box model can be used when active control is to be performed.

Another approach developed for application in active control was proposed by

Cammarata et al[35], with a non-linear black-box as the dynamical model. They assumed that the combustor's dynamics behavior could be captured by three different and interrelated NARX models (non-linear autoregressive with exogenous input) for the three different outputs of the combustion system: the emission of CH radicals and the internal and external pressure oscillations. Each NARX model was defined by

$$y(t)=F[y(t-\Delta t),\ldots,y(t-n_y\Delta t),u(t-\Delta t),\ldots,u(t-n_u\Delta t)] \tag{2.13}$$

where $F$ is a non-linear function and $n_y$ and $n_u$ are the dimension space parameters to be estimated.

The identification of the system was implemented using a neural network and the results showed that the models were able to give satisfactory descriptions of the experimental data. The predictive capability of the models was limited to a few steps ahead and varied with the variable considered. However, they have shown that the time period for which satisfactory predictions were achieved was sufficient for the implementation of the neural models in their control scheme.

A limited number of studies have approached combustion instability problems using stochastic non-linear system models. Using a gray-box modeling Dunstan[36] and Savaresi[37] derived the following set of equations for the dynamics of each acoustic mode

$$\begin{aligned} &\ddot{\eta}_i + 2\xi_i\omega_i\dot{\eta}_i + \omega_i^2\eta_i = N_i\frac{d}{dt}q_t \\ &q_t = \Phi[\frac{d}{dt}p_t(t-\tau)] \\ &p_t = \sum_{i=1}^{N}\eta_i(t) \end{aligned} \tag{2.14}$$

where $\xi_i$, $\omega_i$, and $N_i$ are the damping ratio, angular frequency and scaling factor of the second-order oscillator representing the acoustic mode amplitude ($\eta_i$) in the combustor, $q_t$ is the heat release rate measured by an optical sensor, $\Phi[.]$ is an input-output static non-linear mapping, $p_t$ is the measured dynamic pressure, and $\tau$ is a convective time delay.

Notably, there is no stochastic excitation in the model. They used a common approach in which the dynamical model is represented by a self-excited system in closed loop and split the structure in two blocks. The block with the forward loop contains the linear acoustics, and the block with the feedback loop includes the convective time delay and the nonlinear heat release model. A linear system identification technique was applied to identify the model parameters in the forward loop and tools of non-linear analysis were used to fit a continuously differentiable function representing the non-linear mapping to sets of input-output data. Results showed that the simulated pressure oscillations using the estimated model parameters and non-linear mapping was in good agreement with their experimental data.

This research follows some of the ideas presented in the studies aforementioned, mainly in the non-linear system identification approach. However, we make use of the recent advances in the field of SID which allowed the implementation of more robust and accurate SID techniques as well as the identification of more complex systems. In this sense, using a stepwise approach this research includes some features in the combustor's dynamical model which were not treated in the previous studies. In particular, the following issues are taken into account: 1) the influence of the stochastic excitation; 2)

the presence of coupling between excited modes in the dynamic model; and 3) the need for a dynamic model to express the non-linearities due to unsteady heat release.

# CHAPTER 3

# EXPERIMENTAL DATA

The experimental data used in this work were collected in a parallel and related study at Georgia Tech in which the stability characteristics of a liquid rocket engine combustor simulator (LRECS) was investigated. In the next sections the experimental setup, the tests procedures are described. A preliminary analysis of the collected data and some comments about the overall behavior of the system are also presented.

## 3.1 The Liquid Rocket Engine Combustor Simulator

Figure 3.1 presents a schematic of the LRECS used in this study. The combustor includes a circular injector plate on which seven “smart” injectors are symmetrically distributed, as shown in the detail (top view A) in Figure 3.1. The combustor chamber is a quartz tube having internal diameter of 104mm and length of 325mm. Jet-A was used as the liquid fuel and injected into a swirled preheated ($T = 200^{o}C$) air stream, which served as the oxidizer.

The concept and development of the “smart” injectors arouse from the idea of a “slow" active control approach for preventing the onset of detrimental combustion instabilities in LREs. In this sense, the idea is to "actively" damp the instability by modifying the properties of the combustion process. This approach was motivated by the knowledge that one of the conditions for the occurrence of combustion instabilities is that the characteristic combustion time (e.g., time required to evaporate and burn a typical droplet) approximately equal the characteristic acoustic time (i.e., period of the unstable mode). Consequently, if one could change the characteristic combustion time in an

engine, the instability would be damped because the combustion time would no longer equal the acoustic time.

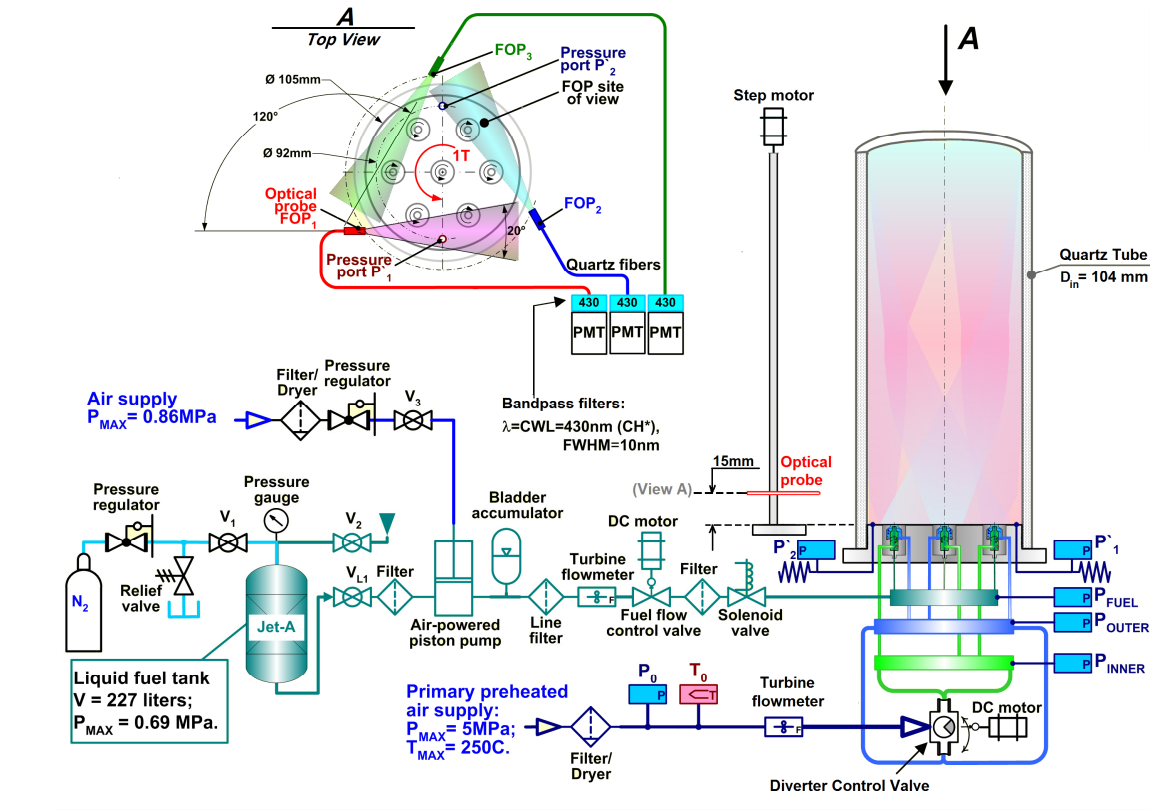


Figure 3.1: Schematic of the liquid rocket engine combustor simulator.

The "smart" injectors have capabilities for changing the characteristics of their spray and, thus, the combustion time. They are double-staged, air-assisted injectors, as shown in Figure 3.2. Swirl was imparted to both inner and outer air streams in opposite directions through separate sets of tangentially oriented orifices. These swirlers shared common manifolds, allowing a diverter valve to simultaneously adjust the mass flow rate of air between the inner and outer swirling air streams for all injectors. To atomize the fuel, the primary air flow was injected with swirl into the fuel stream near the exit of the

fuel nozzle. The secondary air flow was injected with a counter swirl into an annular space downstream of the primary stream injection location, further atomizing the fuel at the primary injector's exit plane.

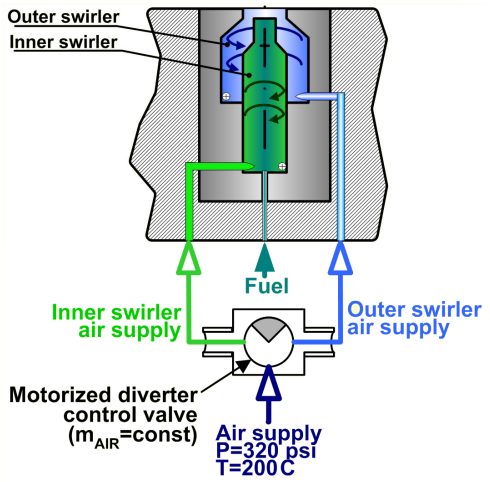


Figure 3.2: Details of the "smart" fuel injectors.

Because the orifices in each swirler in each injector had equal cross sectional area and the air flow through these orifices was choked at most of operating conditions, the ratio of the pressures measured in he inner and outer swirlers was assumed to be the same as the mass flow rate ratio between the entire set of inner and outer swirlers. The control parameter, *K*, called swirl flow ratio was defined as

$$K = \frac{\dot{m}_{air,inner}}{\dot{m}_{air,outer}} = \frac{p'_{inner}}{p'_{outer}} = \frac{\dfrac{100 \times p'_{inner}}{(p'_{inner} + p'_{outer})}}{\dfrac{100 \times p'_{outer}}{(p'_{inner} + p'_{outer})}} \tag{3.1}$$

The reactants spray pattern could be controlled by changing the swirl flow ratio as shown in Figure 3.3. Visualization of the spray was achieved with a vertical laser sheet positioned at the centerline of the spray; therefore, these images depict a thin center slice

of the spray. When the air flow mostly through the outer swirler (e.g., $K = 25/75$) the spray exits the injector orifice nearly radially as shown if Figure 3.3a. As the inner air flow is increased, the spray pattern transitions sharply into a hollow cone which becomes narrower as the inner air flow is further increased, as shown in Figures 3.3b and 3.3c. Subsequent increases in the inner air flow rate causes a solid cone spray be formed, as shown in Figure 3.3d for $K = 75/25$.

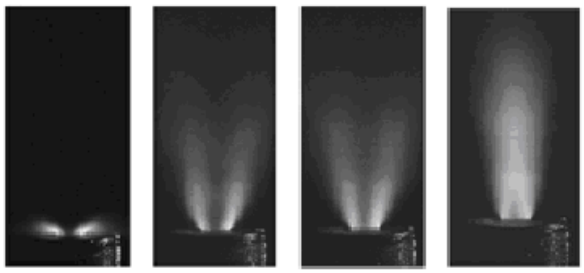


Figure 3.3: Dependence of the spray pattern upon changes in the control parameter *K*.

Pressure oscillations in the combustor were measured using two air-cooled piezoelectric pressure transducers (Kistler-211B5) through the pressure ports positioned on the opposite sides of the diameter of the injector plate, at 8 mm from the wall of the quartz tube as shown in Figure 3.1 (top view A). The transducers were installed on "semi-infinite tubes" at a distance of 270 mm from the injector face to provide a flat frequency response and protect them from overheating. Measured dynamic pressures were recorded with high resolution at sampling frequency 48 KHz using Sony SIR-1000i data recorder simultaneously with the signals of photo-multipliers (PMT) collecting chemiluminescence of the flame.

The time and spatial dependence of the flame chemiluminescence was primarily measured to determine the reaction zone behavior. More specifically, these data were used to observe spinning tangential instability in the combustor. For this purpose three fiber optic probes ( $FOP'_{1,2,3}$ ) were strategically located around quartz combustor wall covering 3 x 120° segments of the reaction zone as shown in the Figure 3.1 (top view A). They were placed in the plane 15mm downstream the injector face to characterize fluctuations of flame radiation near the maximum of the reaction rate in case of tangential instability. Probes were connected to photomultipliers through identical bandpass filters (CWL=430nm, FWHM=10nm) collecting $CH^*$ chemiluminescence from the flame. The intensity of the collected CH* chemiluminescence has been widely used for measuring both local and overall rates of heat release[38]. In this research it was used as a measure of the rate of the unsteady heat release, $\dot{Q}'$ .

### 3.2 Test Procedure and Preliminary Analysis

It had been demonstrated that by changing $K$ and, thus, the spray properties, the "smart" injector was able to control the amplitude of combustion instabilities by varying the characteristics of the combustion process in a single-injector combustor[39]. Then a series of tests were performed to assess the stability characteristics of the multi-injector LRECS using the apparatus described in the previous section.

The first set of experiments was designed to provide the data that would determine the stability maps. The control parameters chosen as coordinates were the equivalence ratio, $\phi$, and the swirl flow ratio, $K$. During each run in the test, the equivalence ratio was set up in the control panel and held constant. This was done by fixing the fuel and the air flow rates.

The fuel flow rate was controlled by a precision metering valve driven by a DC motor. Air supply pressure was set at 276psi and its temperature was ~$200^0$C. Air supply pressure and temperature was controlled using laboratory control units. While the total air flow rate was set by a measuring orifice. Once the equivalence ratio was set, the swirl flow ratio was varied by acting on the diverter valve driven by a DC motor. At each run, the swirl flow ratio was swept; i.e., it started at 60/40, decreased to 12/88, and finally brought back to 60/40, thus the cycle.

The signals from the pressure transducers inside the combustor were collected at each cycle for several different equivalence ratios, and after processing those data stability maps could be plotted. Usually, we split the data into increasing and decreasing part of the swirl flow ratio cycle to search for differences in the system behavior. Figure 12 shows the stability map of the LRECS considering only the increasing part of the swirl flow ratio cycle; i.e., from 12/88 to 60/40.

The measured data was divided into three classes of stability. Stable combustion operation was defined as operating conditions where the peak-to-peak pressure amplitude in the atmospheric combustor does not exceed 2% of the static pressure in the combustor. That is equivalent to the requirement that the amplitude level would not exceed 0.1 psi (RMS). Above this threshold, the combustor was considered unstable. The unstable combustor would experience moderate instabilities when the amplitude level was larger than 0.15 psi (RMS) and smaller than 0.4 psi (RMS), and severe instabilities when the amplitude level exceeded 0.4 psi (RMS).

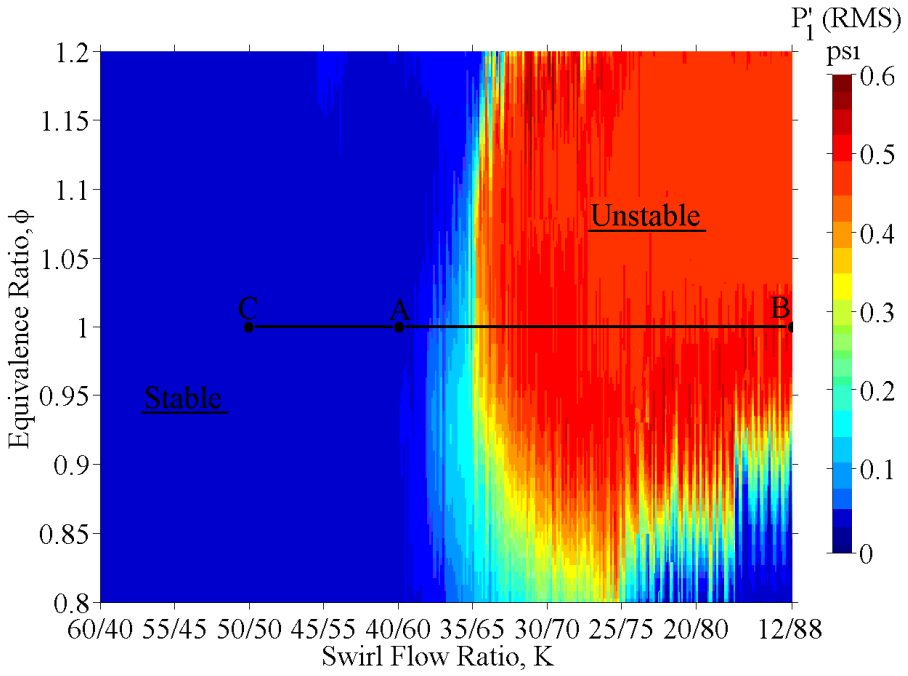


Figure 3.4: Stability map for the LRE combustor simulator for increasing values of the control parameter *K*.

In order to investigate the onset and decay of the combustion instability in the LRECS, let us consider a specific set of the experimental data which reveals interesting characteristics. This set corresponds to the run in which the equivalence ratio was held constant and equal to unity (i.e., $\phi = 1$), while the swirl flow ratio was decreased from 40/60 to 12/88 (going from point A to B in the Figure 3.4) and then increased from 12/88 to 52/48 (going from point B to C in the Figure 3.4). The variation in the swirl flow ratio was performed in a stepwise manner, to provide short time interval (about 1.5 seconds) when the combustor operation did not change.

Figure 3.5a, 3.5b and 3.5c show the time history of the swirl flow ratio, dynamic pressure oscillations (sensor $P_1'$), and heat release rate oscillations (sensor $FOP_1'$) respectively, during the above test run. As one can notice, as we increased the air flow

through the outer swirler (decreasing $K$) excitation of instability and significant growth of the amplitude of the pressure and heat release rate oscillations were observed. On the other hand, increasing the air flow through the inner swirler usually had a stabilizing effect.

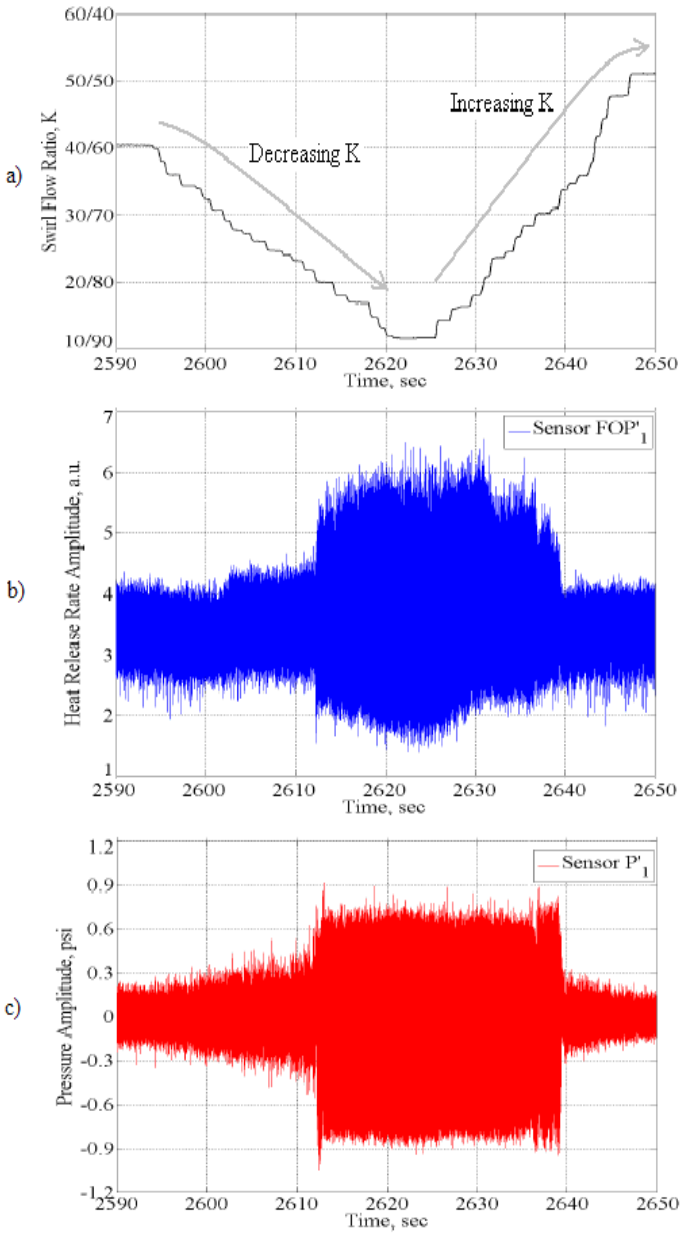


Figure 3.5: Time history of: a) control parameter $K$; b) dynamic pressure; and c) heat release rate oscillations.

Working with the dynamic pressure oscillations and swirl flow ratio data shown in the Figure 3.5, we can eliminate the time dependence and provide the plot in Figure 3.6. It shows the dependence of the pressure oscillations amplitude (RMS) upon the swirl flow ratio. A very important observation made from this plot is that the value of $K$ at which the onset and decay of the instability occurred depends on if $K$ was increasing or decreasing. That produces a "loop" in the plot that is also known as bistable region, bistability or hysteresis. To create hysteresis there must be some history in the dynamical system; i.e., the response of the system to changes in a given parameter is history-dependent. The presence of hysteresis indicates two important ingredients in the system: nonlinearity and feedback.

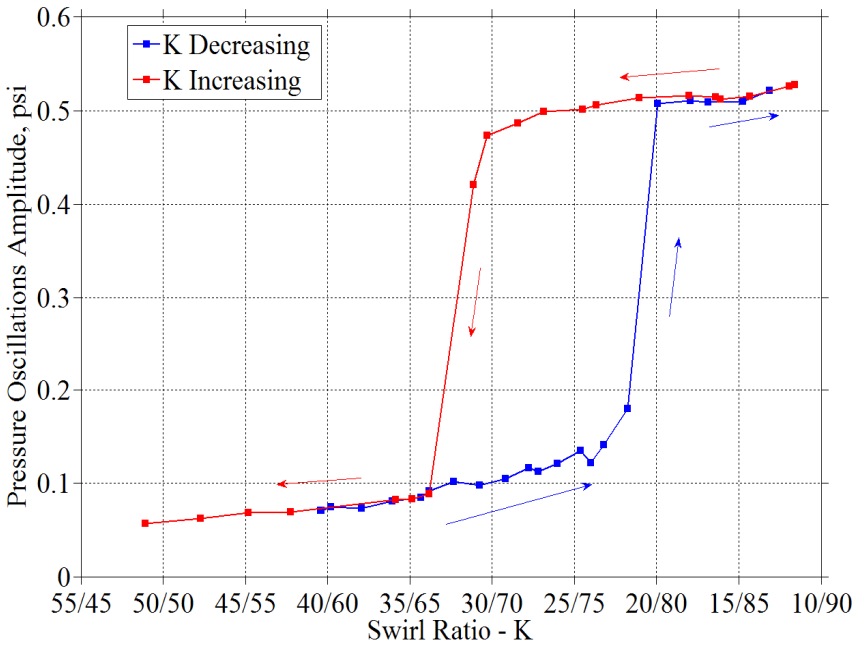


Figure 3.6: Dependence of the RMS pressure oscillations upon changes in the control parameter K

As will be shown later in this thesis, we can represent the combustor dynamics by the following equation

$$\dot{p}' = F(p', K) \tag{3.2}$$

where the behavior of the system, given by the amplitude of the pressure oscillations (RMS) is described by the function *F,* which combines nonlinearities and feedback, and depends upon the control parameter, *K*. The jumps in the Figure 3.5, characterizing the changes in stability of the system, are called bifurcations and the values of the control parameter at which the system stability changes corresponds to the so-called bifurcation points. In this sense, Figure 3.6 can be considered a bifurcation diagram which shows how the system dynamics are affected by the value of the control parameter.

### 3.2.1 Natural modes in the combustor

The results of the preliminary analysis presented so far have provided important information which can be used later in the derivation of the dynamical model. For this purpose, the identification of the excited modes in the combustor can also be useful. The natural frequencies of the longitudinal, transverse and mixed longitudinal-transverse oscillations in the LRECS can be estimated by correlating them with classical acoustic mode oscillations in a cylindrical pipe of diameter *D* and length *L* that is closed at the injectors plate and open at the combustor exit. The reasoning for this approximation will be discussed in the next chapter. The modal frequencies depend on the geometrical dimensions of the combustor, boundary conditions on the walls, and the speed of sound ($\overline{a}$) inside the combustor which is given by

$$\overline{a} = \sqrt{\gamma R T_{ad}} \tag{3.3}$$

where $\gamma$ is the ratio of the specific heats of the products of combustion (also known as isentropic exponent), $R$ is the gas constant, and $T_{ad}$ is the adiabatic temperature of the products of Jet-A and air reaction.

For purely longitudinal modes, we have

$$f_p = \frac{(2p-1)\bar{a}}{4L} \tag{3.4}$$

Indicating that the longitudinal modes have only odd harmonics with the fundamental being the quarter wave mode, the first harmonic the three quarters wave mode and so on.

Equation (3.4) is only an approximation, mainly because the behavior of the waves at the ends of a tube (especially at an open end as the LRECS) depends on factors such as the diameter of the tube and the frequency of the waves, and the ends of the tubes are not exactly nodes and antinodes. In other words, the exact point at which a sound wave is reflecting at an open end is not perfectly at the end section of the tube, but a small distance outside the tube. To account for this fact, $L$ was replaced by $L + 0.4D$ in the frequency equation to obtain a more accurate description of the resonant frequencies of the standing waves in a tube. Using this correction, Equation (3.4) becomes

$$f_p = \frac{(2p-1)\bar{a}}{4(L+0.4D)} \tag{3.5}$$

For transverse modes (tangential, radial and combined tangential-radial), we have[37]

$$f_{mn} = \frac{\bar{a}\,\nu_{mn}}{\pi D} \tag{3.6}$$

where $\nu_{mn}$ is the wave number for transverse modes of oscillation in a cylindrical pipe with unity radius, and $\bar{a}$ is the speed of sound. The subscript $m$ denotes tangential

modes whereas $n$ refers to radial modes. The wave numbers for purely transverse modes of oscillations are calculated from the boundary conditions on the walls in terms of the wall impedance. The values of the wave numbers for some of these modes are given in Table 3.1.

Table 3.1: Wave numbers for transverse modes of oscillations in cylindrical pipes with rigid walls.

| | | $n$ | | | |
|---|---|---|---|---|---|
| | | 0 | 1 | 2 | 3 |
| $m$ | 0 | 0.000 | 3.832 | 7.016 | 10.172 |
| | 1 | 1.841 | 5.331 | 8.537 | 11.705 |
| | 2 | 3.054 | 6.707 | 9.068 | 13.169 |
| | 3 | 4.200 | 8.014 | 11.344 | 14.743 |

Finally, for mixed longitudinal-transverse modes we have

$$f_{pmn} = \frac{\bar{a}}{D}\sqrt{\left(\frac{\nu_{mn}}{\pi}\right)^2 + \left(\frac{2p-1}{4(L+0.4D)/D}\right)^2} \tag{3.7}$$

Next, we will analyze the set of experimental data obtained in the run in which the equivalence ratio at $\phi = 1$ while the swirl flow ratio was decreased from 40/60 to 12/88. Using Equations (3.1-3.6) and the thermodynamic data related to the combustion of the mixture Jet-A/Air at that equivalence ratio, we can estimate some the natural frequencies inside the combustor. The results are shown in the Table 3.2. These values are important since they can be used as initial guesses in system identification algorithms which require such data as inputs.

As one can realize the number of acoustic modes which can be present inside the combustor is theoretically infinite. However, just a few of those modes are usually

excited. Consequently, we are interested in determining which modes are excited in the system and their natural frequencies. In order to determine which modes are excited, the chemiluminescence data was processed along with the dynamic pressure data and several estimates of the cross amplitude spectral density (CASD) of these discrete-time signals were performed using the Welch's averaged[31], modified periodogram method of spectral estimation. The cross amplitude spectral density is the distribution of the square root of power per unit frequency. The signals were filtered so that components at frequencies below 200 Hz and above 15 KHz were eliminated.

Table 3.2: Theoretically estimated natural frequencies in the LRECS.

| **Combustor Geometry (no nozzle)** | | | | | |
|---|---|---|---|---|---|
| $L = 325mm$ | | | $D = 104mm$ | | |
| **Thermodynamic Data: Jet-A/Air (@ $p$ = 1atm, $\phi = 1$ , $T_{in,air} = 473K$ )**[40] | | | | | |
| $T_{ad} = 2348.7K; \gamma = 1.1680; R = 290.82J/KgK \Rightarrow \bar{a} = 893.2m/s$ | | | | | |
| **Acoustic Mode of Oscillation** | $p$ | $m$ | $n$ | **Equation** | **Natural Frequency (Hz)** |
| 1st Longitudinal mode | 1 | - | - | 19 | 609.11 |
| 2nd Longitudinal mode | 2 | - | - | 19 | 1827.33 |
| 3rd Longitudinal mode | 3 | - | - | 19 | 3045.55 |
| 1st Tangential mode | - | 1 | 0 | 20 | 5032.92 |
| 2nd Tangential mode | - | 2 | 0 | 20 | 8349.01 |
| 1st Radial mode | - | 0 | 1 | 20 | 10475.90 |
| 1st Longitudinal – 1st Tangential mode | 1 | 1 | 0 | 21 | 16425.51 |
| 2nd Radial mode | - | 0 | 2 | 20 | 19180.30 |

From analysis of the data, five regimes of combustor dynamics were identified in the tests whose time history was presented in Figure 3.5. The first regime corresponds to the stable operation at the beginning of the test where $K$ is decreasing. Figure 3.7 shows the CASD of the data when the LRECS operated under this regime. In spite of the low

level of oscillations amplitude in the combustor, the spectrum reveals distinctive peaks at the frequencies around $f = 600Hz$, $f = 1800Hz$, $f = 2800Hz$, $f = 4800Hz$, $f = 7800Hz$ and $f = 9600Hz$, which likely correspond to the six first natural frequencies estimated in Table 3.2. It should be noted, however, that these peaks in the spectrum are "visible" due to the scale applied to the amplitude axis. The spectrum also reveals a certain level of background noise at all frequencies.

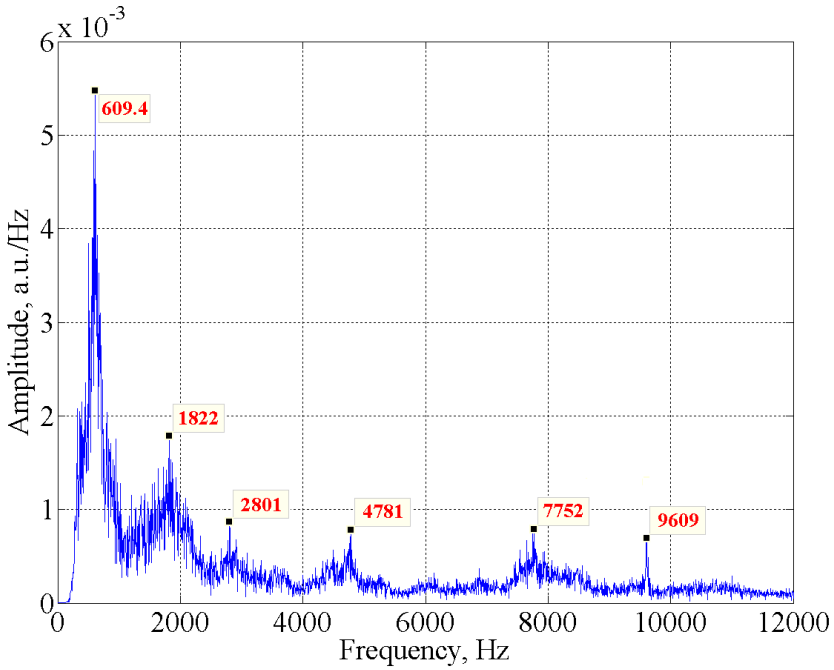


Figure 3.7: Cross amplitude spectral density from sensors $FOP_1'$ and $P_1'$ during stable operation of the combustor ($\phi = 1; K = 40/60$).

The second regime corresponds to the transition from stable to unstable combustion. Figure 3.8 shows the CASD describing the second regime. The spectrum shows an increase in the amplitude of the $f \approx 600Hz$ mode, which can be identified as the quarter wave longitudinal mode (¼L). The excitation of the longitudinal mode during

transition from stable to unstable operation is accompanied by the appearance of a significant peak at $f \approx 5000Hz$, which closely matches the frequency of the first tangential mode (1T). The amplitude of this peak is approximately 50% of the dominating quarter wave longitudinal peak. A certain increase in spectrum amplitude is also observed at $f \approx 7800Hz$, which closely corresponds to second tangential mode (2T).

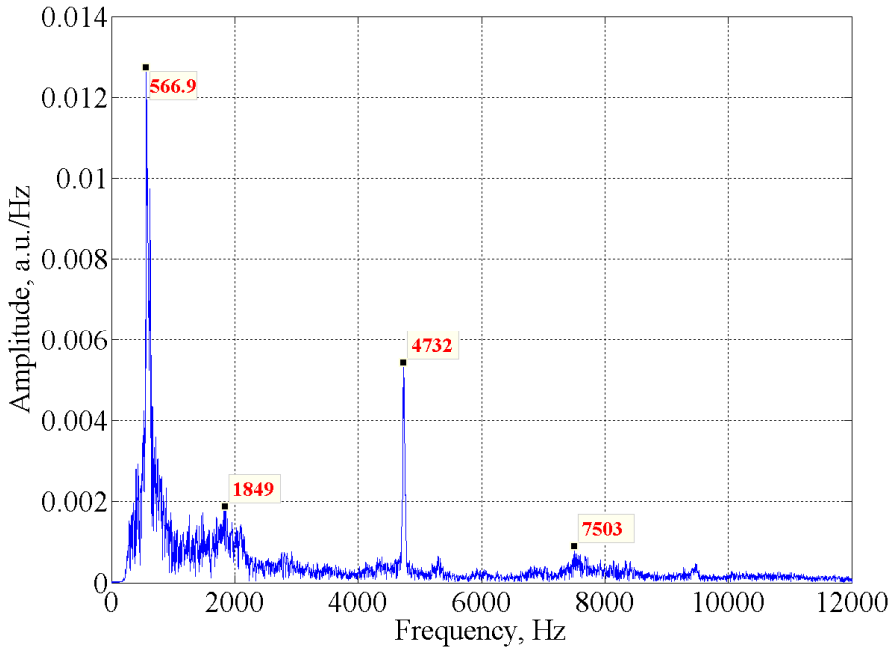


Figure 3.8: Cross amplitude spectral density from sensors $FOP_1'$ and $P_1'$ during the transition regime in the combustor ($\phi = 1; K = 25/75$).

The third regime corresponds to the severely unstable operation after the transition regime. The cross amplitude spectrum density presented in Figure 3.9 indicates that the instability was dominated by the oscillations of the first tangential mode at frequency around $f = 5000Hz$ and its first harmonic. A very small peak corresponding

to the ¼ L mode is also present. In addition to the agreement between the measured frequency and the estimated value in Table 3.2, the excitation of the first tangential mode oscillations was supported by the phase in the cross spectrum calculated at this frequency from the signals of the two dynamic pressure sensors. The cross spectrum indicated anti-phase (out-phase) signals at that frequency, which was expected for the first tangential mode since the sensors were located at diametrically opposite positions.

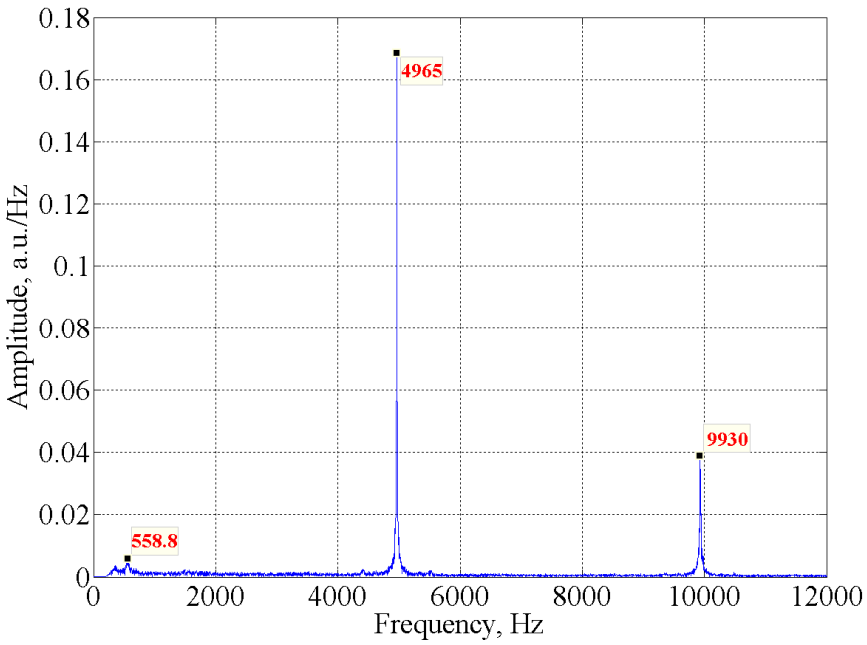


Figure 3.9: Cross amplitude spectral density from sensors $FOP_1'$ and $P_1'$ during unstable operation of the combustor ($\phi = 1; K = 16/84$).

The forth and fifth regimes describe the unstable operation just before the decay of the tangential mode instability and stable operation just after the decay of the instability, respectively. The spectra of these regimes are very similar to those presented in Figures 3.8 and 3.9. An important observation is the presence of the same modes, in all

of these regimes; i.e., the peaks occurred at approximately the same frequencies in the spectrum which characterize stable operation of the combustor just before and immediately after instability decayed. However, the amplitudes of those modes varied. That will be used later as a guide to model possible coupling and triggering between modes when deriving the dynamical model.

Figure 3.10 shows the cross power spectrogram of the chemiluminescence and dynamic pressure data shown in Figure 3.5. One can see the sudden changes in frequency content as the combustor goes from stable to unstable and vice-versa.

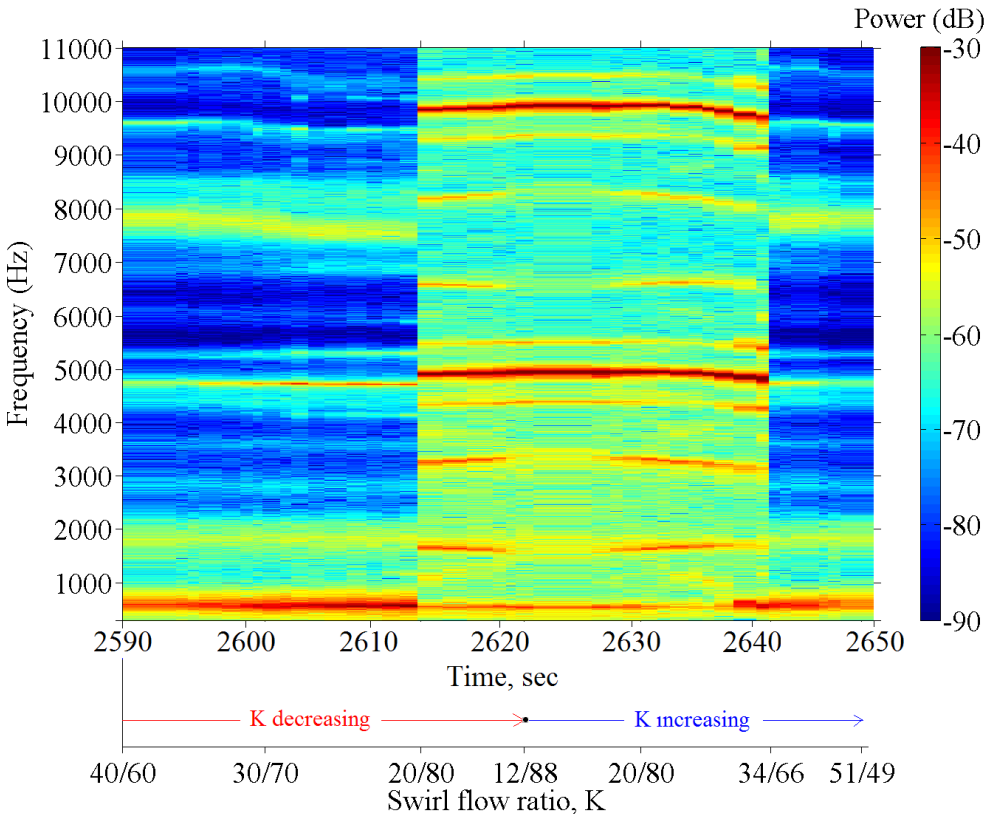


Figure 3.10: Cross amplitude spectrogram sensors $FOP_1'$ and $P_1'$ during the whole period of test.

Since the developed approach in this research is based on gray-box modeling, the following findings collected by the preliminary analysis of the experimental data will play a role in the development of the dynamical model for the system:

1) The excited modes are very well approximated by the natural acoustic modes of an open-closed end tube whose frequencies and mode shapes can be estimated from solutions of the linear wave equation.
2) Even at stable operation, peaks in the spectrum corresponding to acoustics modes are present with amplitudes much larger than the amplitude level of the background noise, implying a high value of signal-to noise ratio (SNR) in the collected signals.
3) The number of excited modes whose power in the spectral analysis accounts for more than 95% of the total power in the collected signals is not larger than eight, indicating that only a few well defined modes are responsible for most of the acoustic energy content in the signals.
4) The presence of hysteresis implies the presence of nonlinearities and feedback in the system. This indicates that the dynamical model should take into account that the response of the system to changes in a given parameter is history-dependent to allow the presence of bi-stability.

# CHAPTER 4

# THERMOACOUSTIC MODEL

The representation of a dynamical system by a mathematical model is one of the most important aspects in dynamical system identification. In this work, we are interested in deriving a model that captures the behavior of the LRECS, to allow assessment of its stability margin. In particular, we seek to develop a gray-box model, i.e., its derivation is based on the physics of the problem.

The analytical framework followed here is based upon more than fifty years of research in the field of combustion instabilities. This formalism has led to the most widely used methods for analyzing and interpreting combustor dynamics. The basic idea is to represent unsteady motions inside a combustor in terms of the acoustic modes of the chamber, so that the unsteady field can be expressed as a synthesis of classical acoustic modes with time-varying amplitudes. Then, we search for an approach for calculating the changes of these amplitudes due to changes in operating conditions. The approach is quite general and can be applied to most of combustor chambers (LREs, gas turbines, etc.).

Due to the intricate physical and chemical processes taking place inside the combustor, the classical acoustic representation is an approximation. However, one can show those processes have small effects, producing small departures from the classical acoustic frequencies and, more significantly, small fractional changes of the modal amplitudes during a period of oscillation[2]. Therefore, combustion instabilities can be seen as perturbations of classical acoustics and the gray-box modeling must include the

derivation of some kind of wave equation. This will be carried out in the next two sections.

### 4.1 Nonlinear Wave Equation

All gray-box models are based upon the physics of the system. The best way to start this kind of modeling is writing the conservation equations for the problem. Since the system contains condensed phase (i.e., liquid fuel) the equations of motion must be written for the two phases (the gas and a condensed phase comprising the liquid droplets). The properties of each phase are represented as mass averages of the properties of all member species. Consequently, the gases are treated as one gas and the condensed species as a liquid.

Following the work of Culick[12], we can combine the equations for two-phase flow and construct a system of equations representing a single fluid. The procedure is described in Appendix A. As a result, we can treat combustor dynamics under broad conditions as unsteady motions of a fluid having the mass-averaged properties of the actual medium. The governing equations are:

- Conservation of Mass: $$\frac{D\rho}{Dt} = -\rho\nabla.\mathbf{u} + \mathcal{W} \tag{4.1}$$

- Conservation of Momentum: $$\rho\frac{D\mathbf{u}}{Dt} = -\nabla p + \mathcal{F} \tag{4.2}$$

- Conservation of Energy: $$\rho C_v \frac{DT}{Dt} = -p\nabla.\mathbf{u} + \mathcal{Q} \tag{4.3}$$

- Equation of State: $$p = \rho RT \tag{4.4}$$

where the substantial derivative is defined in terms of the gas velocity,

$$\frac{D}{Dt} = \frac{\partial}{\partial t} + \mathbf{u}.\nabla \tag{4.5}$$

and the definitions of the variables and the source functions $\mathcal{W}$, $\mathcal{F}$, and $Q$ are also given in Appendix A. The source functions account for all relevant physical processes in the system to be analyzed.

Now, multiplying Equation (4.1) by $RT$, Equation (4.3) by $R/C_\upsilon$ and summing the resulting expressions one obtains

$$\begin{aligned} RT\frac{D\rho}{Dt} &= -\rho RT\nabla.\mathbf{u} + \mathcal{W}RT \\ &+ \\ \rho R\frac{DT}{Dt} &= -\frac{pR}{C_\upsilon}\nabla.\mathbf{u} + \frac{Q_R}{C_\upsilon} \\ \Rightarrow RT\frac{D\rho}{Dt} + \rho R\frac{DT}{Dt} &= -(1+R/C_\upsilon)p\nabla.\mathbf{u} + \mathcal{W}RT + \frac{Q_R}{C_\upsilon} \end{aligned} \tag{4.6}$$

Taking the substantial derivative of Equation (4.4) we have

$$\frac{Dp}{Dt} = \rho R\frac{DT}{Dt} + RT\frac{D\rho}{Dt} + \rho T\frac{DR}{Dt} = \rho R\frac{DT}{Dt} + RT\frac{D\rho}{Dt} + p\frac{D\ln(R)}{Dt} \tag{4.7}$$

Substituting Equation (4.6) into (4.7), one obtains the equation for the pressure

$$\frac{Dp}{Dt} = -\gamma p\nabla.\mathbf{u} + \mathcal{P} \tag{4.8}$$

where $\mathcal{P} = \mathcal{W}RT + \frac{Q_R}{C_\upsilon} + p\frac{D\ln(R)}{dt}$.

These governing equations can be used to derive the nonlinear wave equation for the combustor pressure. The derivation starts by writing all dependent variables as the sum of a mean (or averaged value) and a small-amplitude fluctuating (or perturbation) parts. So we get,

$$p(\mathbf{r},t) = \overline{p}(\mathbf{r}) + p'(t) \tag{4.9}$$

$$\rho(\mathbf{r},t)=\bar{\rho}(\mathbf{r})+\rho'(\mathbf{r},t) \tag{4.10}$$

$$\mathbf{u}(\mathbf{r},t)=\bar{\mathbf{u}}(\mathbf{r})+\mathbf{u}'(\mathbf{r},t) \tag{4.11}$$

$$\mathcal{F}(\mathbf{r},t)=\bar{\mathcal{F}}(\mathbf{r})+\mathcal{F}'(\mathbf{r},t) \tag{4.12}$$

$$\mathcal{P}(\mathbf{r},t)=\bar{\mathcal{P}}(\mathbf{r})+\mathcal{P}'(\mathbf{r},t) \tag{4.13}$$

Next, we assume the mean pressure is uniform inside the chamber, which implies the average Mach number of the mean flow is small, and that the average density is also uniform. All mean terms are independent of time and assumed to satisfy their corresponding mean equations. Thus, the mean parts of Equations (4.2) and (4.8) are

$$\bar{\rho}\frac{D\bar{\mathbf{u}}}{Dt}=-\nabla\bar{p}+\bar{\mathcal{F}} \tag{4.14}$$

$$\frac{D\bar{p}}{Dt}=-\gamma\bar{p}\nabla.\bar{\mathbf{u}}+\bar{\mathcal{P}} \tag{4.15}$$

Substituting Equations (4.10) to (4.13) into (4.2) and (4.8) yields equations that contain many terms with higher orders in the fluctuating variables. However, since previous studies[41] have shown that adequate description of the system can be obtained if only terms up to second order in fluctuations are retained, the following equations are obtained:

$$(\bar{\rho}+\rho')\frac{\partial\mathbf{u}'}{\partial t}=-\nabla p'-\bar{\rho}\mathbf{u}'.\nabla\mathbf{u}'-(\bar{\rho}+\rho')(+\mathbf{u}'.\nabla\bar{\mathbf{u}}+\bar{\mathbf{u}}.\nabla\mathbf{u}')-\rho'\bar{\mathbf{u}}.\nabla\bar{\mathbf{u}}+\mathcal{F}' \tag{4.16}$$

$$\frac{\partial p'}{\partial t}+\gamma\bar{p}\nabla.\mathbf{u}'+\gamma p'\nabla.\mathbf{u}'+\gamma p'\nabla.\bar{\mathbf{u}}=-\mathbf{u}'.\nabla p'-\bar{\mathbf{u}}.\nabla p'+\mathcal{P}' \tag{4.17}$$

Differentiating Equation (4.17) with respect to time gives

$$\begin{aligned}&\frac{\partial^2 p'}{\partial t^2}+\gamma(\bar{p}+p')\nabla.\frac{\partial\mathbf{u}'}{\partial t}+\gamma\frac{\partial p'}{\partial t}\nabla.\mathbf{u}'+\gamma\frac{\partial p'}{\partial t}\nabla.\bar{\mathbf{u}}=-\frac{\partial\mathbf{u}'}{\partial t}.\nabla p'\\&-\mathbf{u}'.\nabla\frac{\partial p'}{\partial t}-\bar{\mathbf{u}}.\nabla\frac{\partial p'}{\partial t}+\frac{\partial\mathcal{P}'}{\partial t}\end{aligned} \tag{4.18}$$

Assuming that the isentropic relation can be used

$$\rho' \approx \frac{p'}{\bar{a}^2} \tag{4.19}$$

Substituting for $\frac{\partial \mathbf{u}'}{\partial t}$ from Equation (4.16) into Equation (4.18) and applying (4.19) we obtain the following nonlinear wave equation for pressure oscillations [42],[43]

$$\nabla^2 p' - \frac{1}{\bar{a}^2}\frac{\partial^2 p'}{\partial t^2} = \mathcal{H} \tag{4.20}$$

which must satisfy the following boundary condition

$$\mathbf{n}.\nabla p' = -\mathcal{B} \tag{4.21}$$

The boundary condition for the pressure field is found by taking the scalar product of the outward normal vector, $\mathbf{n}$, at the chamber boundary, with the momentum equation. In these equations, $\mathcal{H}$ and $\mathcal{B}$ are, in general, nonlinear functions given by

$$\begin{aligned}\mathcal{H} = &-\bar{\rho}\nabla.(\mathbf{u}'.\nabla\bar{\mathbf{u}} + \bar{\mathbf{u}}.\nabla\mathbf{u}') + \frac{1}{\bar{a}^2}\bar{\mathbf{u}}.\nabla\frac{\partial p'}{\partial t} + \frac{\gamma}{\bar{a}^2}\frac{\partial p'}{\partial t}\nabla.\bar{\mathbf{u}} - \bar{\rho}\nabla.(\mathbf{u}'.\nabla\mathbf{u}' + \frac{p'}{\gamma\bar{p}}\frac{\partial \mathbf{u}'}{\partial t}) \\ &+ \frac{1}{\bar{a}^2}\frac{\partial}{\partial t}(\mathbf{u}'.\nabla p') + \frac{\gamma}{\bar{a}^2}\frac{\partial}{\partial t}(p'\nabla.\mathbf{u}') + \nabla.\mathcal{F}' - \frac{1}{\bar{a}^2}\frac{\partial \mathcal{P}'}{\partial t}\end{aligned} \tag{4.22}$$

$$\mathcal{B} = \bar{\rho}\frac{\partial \mathbf{u}'}{\partial t}.\mathbf{n} + \bar{\rho}(\mathbf{u}'.\nabla\bar{\mathbf{u}} + \bar{\mathbf{u}}.\nabla\mathbf{u}' + \mathbf{u}'.\nabla\mathbf{u}').\mathbf{n} + \frac{p'}{\bar{a}^2}\frac{\partial \mathbf{u}'}{\partial t}.\mathbf{n} - \mathcal{F}'.\mathbf{n} \tag{4.23}$$

## 4.2 Modal Expansion

The nonlinear wave equation just derived is a partial differential equation (PDE). Since the dynamical system identification techniques in this work will deal with time-series of experimental data, the developed dynamical models should be represented in terms of ordinary differential equations (ODEs) or algebraic difference equations. The transformation of the PDE into a set of equivalent ODEs can be accomplished by

applying a spatial averaging technique based on a modified Galerkin's method proposed by Powell and Zinn[44].

The Galerkin method is a special case of the Method of Weighted Residuals (MWR). We start by writing the wave equation and its boundary condition in the form of residuals as

$$\begin{aligned} E(p') &= 0 \\ B(p') &= 0 \end{aligned} \tag{4.24}$$

where

$$\begin{aligned} E(p') &:= \nabla^2 p' - \frac{1}{\bar{a}^2}\frac{\partial^2 p'}{\partial t^2} - \mathsf{H} \\ B(p') &:= \mathbf{n}.\nabla p' + \mathsf{B} \end{aligned} \tag{4.25}$$

Now, we approximate the dependent variable, $p'$, as an expansion in a set of basis functions $\varphi_n$. In this sense, we consider $\tilde{p}'$ as an approximation of the actual pressure perturbation, $p'$, and express it as an expansion modal expansion truncated to $N$ terms. Thus, we can write

$$\tilde{p}' = \sum_{m=1}^{N} a_m \phi_m \Rightarrow p' = \lim_{N\to\infty} \tilde{p}' = \lim_{N\to\infty} \sum_{m=1}^{N} a_m \phi_m \tag{4.26}$$

The MWR consists of spatial averaging, with a weighting function $\Theta_m$, of Equation (4.25), that employs the approximation for $\tilde{p}'$ and requiring that the result be zero; i.e.,

$$\iiint_V E(\tilde{p}')\Theta_m dV = 0 \tag{4.27}$$

Next, the unknown coefficients $a_m$ in Equation (4.26) are determined in a way that minimizes the residual in some sense. If the boundary conditions are simple (i.e.,

homogeneuous), it is often possible to find an approximate solution $\tilde{p}'$ that satisfies the boundary conditions. In this case the averaging process applied to the boundary condition is already identically zero. That is not the case in combustion instabilities problems where the boundary conditions are complex.

The Galerkin method is a special case of the MWR since the weighting functions are the same as the basis functions used in the modal expansion; i.e., $\Theta_m = \varphi_m$. A modified Galerkin method was proposed[44] to account for the averaging process applied to boundary conditions as well. The coefficients $a_m$ are determined by solving the following equation

$$\iiint_V (\nabla^2 \tilde{p}' - \frac{1}{\bar{a}^2}\frac{\partial^2 \tilde{p}'}{\partial t^2} - \mathcal{H})\phi_m dV - \oiint_S (\mathbf{n}.\nabla\tilde{p}' + \mathcal{B})\phi_m dS = 0 \tag{4.28}$$

If we apply Green's theorem to the first term on the left-hand side, we obtain

$$\iiint_V \nabla^2 \tilde{p}'\phi_m dV = \oiint_S (\tilde{p}'\nabla\phi_m + \phi_m\nabla\tilde{p}').\mathbf{n}dS - \iiint_V \tilde{p}'\nabla^2\phi_m dV \tag{4.29}$$

and substituting the result into Equation (4.28) we have

$$\begin{aligned}
&\oiint_S (\tilde{p}'\nabla\phi_m + \phi_m\nabla\tilde{p}').\mathbf{n}dS - \iiint_V \tilde{p}'\nabla^2\phi_m dV \\
&-\iiint_V \frac{1}{\bar{a}^2}\frac{\partial^2 \tilde{p}'}{\partial t^2}\phi_m dV - \iiint_V \mathcal{H}\,\phi_m dV - \oiint_S (\mathbf{n}.\nabla\tilde{p}' + \mathcal{B})\phi_m dS = 0 \qquad (4.30)\\
&\Rightarrow \oiint_S (\tilde{p}'\nabla\phi_m.\mathbf{n})dS - \iiint_V \tilde{p}'\nabla^2\phi_m dV - \iiint_V \frac{1}{\bar{a}^2}\frac{\partial^2 \tilde{p}'}{\partial t^2}\phi_m dV = \iiint_V \mathcal{H}\,\phi_m dV + \oiint_S \mathcal{B}\phi_m dS
\end{aligned}$$

The next step is to choose the mode shape $\psi_N$ as the weighting function. The equations which define the mode shapes can be obtained from classical acoustics by setting $\mathcal{H} = \mathcal{B} = 0$ in the wave equation and its boundary condition.

$$\nabla^2\psi_N + k_N^2\psi_N = 0 \tag{4.31}$$

$$\mathbf{n}.\nabla \psi_N = 0 \tag{4.32}$$

where $k_N$ is the wave number for the N$^{th}$ mode.

Now substituting $\phi_m = \psi_N$ into Equation (4.30) and using the Equations (4.31) and (4.32) one can write

$$\iiint_V \frac{1}{\overline{a}^2}\frac{\partial^2 \tilde{p}'}{\partial t^2}\psi_N dV + k_N^2 \iiint_V \tilde{p}'\psi_N dV = -\left\{\iiint_V \mathcal{H}\psi_N dV + \oiint_S \mathcal{B}\psi_N dS\right\} \tag{4.33}$$

To proceed with the solution of Equation (4.33) the modal expansion $\tilde{p}'$ must be specified. Assuming that the solution of Equations (4.20) and (4.21) do not significantly differ from the corresponding classical acoustic solutions (i.e., the classical normal mode solutions for which $\mathcal{H} = \mathcal{B} = 0$ ) or a combination of them, we express $\tilde{p}'$ as a finite sum of acoustic modes; i.e.,

$$\tilde{p}'(\mathbf{r},t) = \sum_{m=1}^{M} a_m \varphi_m = \overline{p}\sum_{m=1}^{M} \eta_m(t)\psi_m(\mathbf{r}) \tag{4.34}$$

which in the limit when $M \to \infty$ becomes

$$p'(\mathbf{r},t) = \overline{p}\sum_{m=1}^{\infty} \eta_m(t)\psi_m(\mathbf{r}) \tag{4.35}$$

It is further assumed that the normal modes in Equation (4.35) are orthogonal, so that the following relationship holds

$$\iiint_V \psi_m(\mathbf{r})\psi_n(\mathbf{r})dV = \delta_{mn}\iiint_V \psi_n^2(\mathbf{r}) = E_n^2\delta_{mn} \tag{4.36}$$

The corresponding modal expansion for the acoustic velocity fluctuation can be obtained from the classical acoustics, so that term by term the chosen expansion for $p'$ and $\mathbf{u}'$ satisfies the classical acoustic momentum equation given by

$$\frac{\partial p'}{\partial t}+\gamma\bar{p}\nabla.\mathbf{u}'=0 \tag{4.37}$$

If we assume that the acoustic velocity is approximated by

$$\mathbf{u}'(\mathbf{r},t)=\sum_{m=1}^{\infty}\frac{\dot{\eta}_m(t)}{\gamma k_m^2}\nabla\psi_m(\mathbf{r}) \tag{4.38}$$

and substituting Equations (4.38) and (4.36) into (4.37) we obtain

$$\frac{\partial}{\partial t}\left[\bar{p}\sum_{m=1}^{\infty}\eta_m(t)\psi_m(\mathbf{r})\right]+\gamma\bar{p}\nabla.\left[\sum_{m=1}^{\infty}\frac{\dot{\eta}_m(t)}{\gamma k_m^2}\nabla\psi_m(\mathbf{r})\right]=\bar{p}\sum_{m=1}^{\infty}\dot{\eta}_m(t)[\psi_m(\mathbf{r})+\frac{\nabla^2\psi_m(\mathbf{r})}{k_m^2}]=0 \tag{4.39}$$

which is always satisfied according to Equation (4.31), thus indicating that the assumed expression for the acoustic velocity is correct.

Substituting the expression for the pressure, Equation (4.35), into Equation (4.33) and applying the orthogonality property, Equation (4.36), Culick[43] obtained the following equation for the $N^{th}$ mode

$$\frac{d^2\eta_N}{dt}+\omega_N^2\eta_N=F_N \tag{4.40}$$

where $\omega_N=\bar{a}k_N$ is the natural angular frequency of the $N^{th}$ mode, and

$$F_N=-\frac{\bar{a}^2}{\bar{p}E_N^2}\{\iiint_V\mathcal{H}\psi_N dV+\oiint\mathcal{B}\psi_N dS\} \tag{4.41}$$

is the forcing function, which represents the deviation from unperturbed acoustic modes and provides the mechanisms which allows for initiated oscillations to grow or decay. The forcing function is, in general, a nonlinear function that may depend on other modes (not only the $N^{th}$ mode), thus generating coupling between modes, as will be demonstrated later.

In principle, an infinite number of modes may be excited in the combustor. Therefore, the dynamical model for a general unsteady motion in a combustor can be

represented by the time-evolution of a system of an infinite coupled nonlinear oscillators. The left-hand side of Equation (4.40) describes the motion of an undamped linear oscillator, whereas the forcing function on its right-hand-side will, in general, contain terms representing linear and nonlinear damping, springiness and inertia.

Thus, it is important to understand the connections between parameters that describe the oscillators, the characteristics of the modes, and the definitions provided in the process of spatial averaging. Different problems are distinguished mainly in two respects: geometry of the combustor; and the form of the forcing function. The geometry and the boundary conditions determine the modal expansion functions, or mode shapes $\psi_m(\mathbf{r})$, and the natural frequencies, $\omega_N$. On the other hand, the forcing function explicitly accounts for the influence of gasdynamical effects and includes other processes that need to be described by models, either derived form theory (physically based) or based on experimental results (system identification based). The next section describes the gray-box modeling of the forcing functions in order to write them in a more useful form for system identification purposes.

## 4.3 The Forcing Functions

### 4.3.1 Explicit Terms

Substituting Equations (4.22) and (4.23) into (4.41) we obtain the following expression for the forcing function[41]:

$$-\frac{\overline{p}E_N^2}{\overline{a}^2}F_N = \overline{\rho}(I_1+I_3)+\frac{1}{\overline{a}^2}(I_2+I_4)-\iiint_V \mathcal{F}'.\nabla\psi_N dV+\oiint \overline{\rho}\frac{\partial \mathbf{u}'}{\partial t}.\mathbf{n}dS+\frac{1}{\overline{a}^2}\iiint_V \frac{\partial \mathcal{P}'}{\partial t}\psi_N dV \quad (4.42)$$

where

$$I_1 = \iiint_V (\mathbf{u}'.\nabla\overline{\mathbf{u}} + \overline{\mathbf{u}}.\nabla\mathbf{u}').\nabla\psi_N dV \tag{4.43a}$$

$$I_2 = \frac{\partial}{\partial t}\iiint_V (\gamma p'\nabla.\overline{\mathbf{u}} + \overline{\mathbf{u}}.\nabla p')\psi_N dV \tag{4.43b}$$

$$I_3 = \iiint_V (\mathbf{u}'.\nabla\mathbf{u}' + \frac{\rho'}{\overline{\rho}}\frac{\partial\mathbf{u}'}{\partial t}).\nabla\psi_N dV \tag{4.43c}$$

$$I_4 = \frac{\partial}{\partial t}\iiint_V (\gamma p'\nabla.\mathbf{u}' + \mathbf{u}'.\nabla p')\psi_N dV \tag{4.43d}$$

Following the approach of Chu and Kovasznay[45], we can represent a disturbance in a compressible flowing medium as a combination of three modes of propagation; i.e., acoustic, vorticity, and entropy waves. Thus, we can write

$$p' = p'_a + p'_\Omega + p'_s \tag{4.44a}$$

$$s' = s'_a + s'_\Omega + s'_s \tag{4.44b}$$

$$\Omega' = \Omega'_a + \Omega'_\Omega + \Omega'_s \tag{4.44c}$$

$$\mathbf{u}' = \mathbf{u}'_a + \mathbf{u}'_\Omega + \mathbf{u}'_s \tag{4.44d}$$

where the subscripts $a$, $\Omega$, and $s$ represent the acoustic, vorticity and entropy modes. Assuming small amplitude motions, we can use a zero-order approximation for the flow variables as follow:

$$p' = p'_a = \overline{p}\sum_{m=1}^{\infty}\eta_m(t)\psi_m(\mathbf{r}) \tag{4.45a}$$

$$s' = s'_s \tag{4.45b}$$

$$\Omega' = \Omega'_\Omega \tag{4.45c}$$

$$\mathbf{u}' = \mathbf{u}'_a + \mathbf{u}'_\Omega + \mathbf{u}'_s = \sum_{m=1}^{\infty}\frac{\dot{\eta}_m(t)}{\gamma k_m^2}\nabla\psi_m(\mathbf{r}) + + \mathbf{u}'_\Omega + \mathbf{u}' \tag{4.45d}$$

The density fluctuation contains a contribution from the entropy fluctuation (related to the temperature). From the formula for the entropy of a perfect gas, we have

$$s - s_0 = c_p \log \frac{(p/p_0)^{1/\gamma}}{\rho/\rho_0} \tag{4.46}$$

Thus, expanding Equation (4.46) and assuming a first order approximation in the pressure fluctuations, the following expression can be derived for the density fluctuations

$$\frac{\rho'}{\bar{\rho}} = \frac{1}{\gamma}\frac{p'}{\bar{p}} - \frac{s'}{c_p} \tag{4.47}$$

which leads to the following equations

$$\frac{\rho'_a}{\bar{\rho}} = \frac{1}{\gamma}\frac{p'_a}{\bar{p}} \tag{4.48a}$$

$$\frac{\rho'_s}{\bar{\rho}} = -\frac{s'_s}{c_p} \tag{4.48b}$$

Next, substituting Equations (4.45a-d) into (4.43a-d), one obtains the following results[41]:

$$I_1 = I_1^a + I_1^\Omega + I_1^s \tag{4.49a}$$

$$I_2 = I_2^a \tag{4.49b}$$

$$I_3 = I_3^{aa} + I_3^{a\Omega} + I_3^{as} + I_3^{\Omega a} + I_3^{\Omega\Omega} + I_3^{\Omega s} + I_3^{sa} + I_3^{s\Omega} + I_3^{ss} \tag{4.49c}$$

$$I_4 = I_4^{aa} + I_4^{a\Omega} + I_4^{as} + I_4^{\Omega a} + I_4^{\Omega\Omega} + I_4^{\Omega s} + I_4^{sa} + I_4^{s\Omega} + I_4^{ss} \tag{4.49d}$$

where the definitions of each one of integrals are given in reference[41].

The contributions of all linear processes in the forcing function are included in terms involving first order fluctuations in the acoustic components. Thus, they are combined in the integrals $I_1^a$ and $I_2^a$. Therefore, we can write

$$F_N^L = -\frac{\bar{a}^2}{\bar{p}E_N^2}\left\{\bar{\rho}I_1^a + \frac{1}{\bar{a}^2}I_2^a\right\} = \sum_{i=1}^{\infty}(D_{Ni}\dot{\eta}_i + E_{Ni}\eta_i) \tag{4.50}$$

where the coefficients $D_{Ni}$ and $E_{Ni}$ representing all linear processes in H and B are given by[46]

$$D_{Ni} = \iiint_V \left\{\frac{k_N^2}{k_i^2}\psi_N \bar{\mathbf{u}}.\nabla\psi_i - \psi_i(\bar{\mathbf{u}}.\nabla\psi_N) - \frac{1}{k_i^2}[\nabla\psi_i \times (\nabla\times\bar{\mathbf{u}})].\nabla\psi_N] + (\gamma-1)\psi_N\psi_i\nabla.\bar{\mathbf{u}}\right\}dV + L_D \tag{4.51}$$

$$E_{Ni} = L_E \tag{4.52}$$

where the coefficients $L_D$ and $L_E$ denote the net contribution of terms which are linear in $\dot{\eta}$ and $\eta$, respectively, arising from all sources in the system. In particular, one can show that $D_{NN} = 2\xi_N\omega_N$ and $E_{NN} = 2\theta_N\omega_N$, where $\xi_N$ is the modal damping ratio, $\omega_N$ is the modal angular frequency and $\theta_N$ is the modal frequency shift.

Burnley[41] showed that the effects of linear coupling ($N \neq i$) described by Equation (4.50) are of higher order and could be neglected. Thus, in this approach linear coupling will be neglected so that only $D_{NN} = 2\xi_N\omega_N$ and $E_{NN} = 2\theta_N\omega_N$ will be included in the model.

Similarly, the contributions of the nonlinear gasdynamics to second-order involve terms with second order in acoustic fluctuations. Thus, they are combined in the integrals $I_3^{aa}$ and $I_4^{aa}$ so that

$$F_N^{NL,GD} = -\frac{\bar{a}^2}{\bar{p}E_N^2}\left\{\bar{\rho}I_3^{aa} + \frac{1}{\bar{a}^2}I_4^{aa}\right\} = -\sum_{i=1}^{\infty}\sum_{j=1}^{\infty}[A_{Nij}\dot{\eta}_i\dot{\eta}_j + B_{Nij}\eta_i\eta_j] \tag{4.53}$$

where the coefficients $A_{Nij}$ and $B_{Nij}$ describe gasdynamical nonlinearities and are given by[46]

$$A_{Nij} = \frac{I_{Nij}}{4\gamma E_N^2 k_i^2 k_j^2}[(k_i^2 + k_j^2) - k_N^4 - 4\gamma k_i^2 k_j^2] \tag{4.54}$$

$$B_{Nij} = \frac{I_{Nij}\overline{a}^2}{2\gamma E_N^2}(\gamma - 1)(k_i^2 + k_j^2) \tag{4.55}$$

where $I_{Nij} = \iiint_V \psi_N \psi_i \psi_j dV$ .

The remaining integrals that are not included in Equations (4.50) and (4.53) have terms involving $\mathbf{u}'_\Omega$ and $\mathbf{u}'_s$. Since, the sources of noise in the combustor can be associated with the presence of vorticity and entropy fluctuations, the terms involving these integrals will act as source terms for the noisy part of the acoustic field. Then, the integrals $I_1^\Omega$ and $I_1^s$ which contain only first-order terms in non-acoustic fluctuations can be combined into a noise source term as

$$F_N^{noise,1} = -\frac{\overline{a}^2}{\overline{p}E_N^2}\left\{\overline{\rho}(I_1^\Omega + I_1^s)\right\} = \Xi_N^{(1)}(t) \tag{4.56}$$

Similarly, we combine integrals which contain only second-order terms in non-acoustic fluctuations yielding

$$F_N^{noise,2} - \frac{\overline{a}^2}{\overline{p}E_N^2}\left\{\overline{\rho}(I_3^{\Omega\Omega} + I_3^{\Omega s} + I_3^{s\Omega} + I_3^{ss})\right\} = \Xi_N^{(2)}(t) \tag{4.57}$$

Finally, we combine integrals which contain terms with non-acoustic fluctuations multiplied by acoustic fluctuations and derive the multiplicative noise terms as

$$\begin{aligned} F_N^{noise,3} - \frac{\overline{a}^2}{\overline{p}E_N^2}\left\{\overline{\rho}(I_3^{\Omega a} + I_3^{a\Omega} + I_3^{as} + I_3^{sa}) + \frac{1}{\overline{a}^2}(I_4^{\Omega a} + I_4^{a\Omega} + I_4^{as} + I_4^{sa})\right\} = \\ = -\sum_{i=1}^{\infty}[\Xi_{Ni}^{(3)}\eta_i + (\Xi_{Ni}^{(4)} + \Xi_{Ni}^{(5)})\dot{\eta}_i] \end{aligned} \tag{4.58}$$

Applying the simplification adopted by Burnley[41], we neglect cross-coupling terms in multiplicative noise (i.e., $N \neq i$) in Equation (4.58). Then, we have

$$F_N^{noise,3} - \frac{\bar{a}^2}{\bar{p}E_N^2}\left\{\bar{\rho}(I_3^{\Omega a} + I_3^{a\Omega} + I_3^{as} + I_3^{sa}) + \frac{1}{\bar{a}^2}(I_4^{\Omega a} + I_4^{a\Omega} + I_4^{as} + I_4^{sa})\right\} \approx \tag{4.59}$$
$$\approx -[\Xi_N^{(3)}\eta_N + (\Xi_N^{(4)} + \Xi_N^{(5)})\dot{\eta}_N]$$

Next, we combine the additive noises and the multiplicative noises by defining

$$\Xi_N^0 = \Xi_N^{(1)} + \Xi_N^{(2)} \tag{4.60a}$$

$$\Xi_N^1 = \Xi_N^{(3)} \tag{4.60b}$$

$$\Xi_N^2 = \Xi_N^{(4)} + \Xi_N^{(5)} \tag{4.60c}$$

The expressions derived so far for the terms of the forcing function, allow us to write the nonlinear wave equation as

$$\ddot{\eta}_N + \omega_N^2\eta_N = F_N^L + F_N^{NL-GD} + F_N^{noise,1} + F_N^{noise,2} + F_N^{noise,3} + (F_N)^{\mathrm{NL}} \quad N = 1,2,...,N_m \tag{4.61}$$

where $(F_N)^{\mathrm{NL}}$ accounts for all other nonlinear terms which could not be modeled explicitly (including combustion), and $N_m$ is the total number of excited modes in the combustor.

Substituing Equations (4.50), (4.53), (4.56), (4.57) and (4.59) into Equation (4.61), one obtains the following set of equations where the linear coupling from gasdynamics has been neglected for reasons stated before

$$\ddot{\eta}_N + \underbrace{2\xi_N\omega_N\dot{\eta}_N}_{1} + \underbrace{(\omega_N^2 + 2\theta_N\omega_N)\eta_N}_{2} + \underbrace{\sum_{i=1}^{N_m}\sum_{j=1}^{N_m}(A_{Nij}\dot{\eta}_i\dot{\eta}_j + B_{Nij}\eta_i\eta_j)}_{3} - (F_N)^{\mathrm{NL}} = \tag{4.62}$$
$$= \underbrace{\Xi_N^2\dot{\eta}_N}_{4} + \underbrace{\Xi_N^1\eta_N}_{5} + \underbrace{\Xi_N^0}_{6} \qquad N = 1,2,...,N_m$$

At this point, one can note that the system of equations representing the dynamics of the modes have several terms with different contributions from gasdynamics (linear

represented by terms 1 and 2; nonlinear represented by term 3) and combustor background noise (terms 4, 5, and 6). All of these terms were taken into account explicitly.

4.3.1.1 Stochastic Excitation

Examination of the right hand side of Equation (4.62) shows the presence of two multiplicative noise terms, $\Xi_N^1$ and $\Xi_N^2$, also known as parametric excitation, and one additive noise term, $\Xi_N^0$, also known as external excitation. They represent stochastic processes which are responsible for the background noise found in the power spectra shown in the last chapter. In this thesis, all stochastic processes were modeled as mutually independent zero mean white noise (ZMWN) processes.

As the experimental data is discrete, we consider each stochastic excitation term as a sequence of independent random numbers, $W_i$, with Gaussian distribution and variance $\sigma_W^2$. The continuous time stochastic process, $W(t)$, is obtained via a zero-order-hold in which we consider

$$W(t) = W_i \text{ for } t_i \le t \le t_{i+1} \tag{4.63}$$

where the sampling time is defined by $\Delta t = t_{i+1} - t_i$. In this sense, the noise terms are represented by

$$\Xi_N(t) = W_0(t);\ \Xi_N^1(t) = W_1(t);\text{ and } \Xi_N^2(t) = W_2(t) \tag{4.64}$$

with corresponding intensities calculated as

$$S_{00} = \sigma_0^2 \frac{\Delta t}{2\pi};\ S_{11} = \sigma_1^2 \frac{\Delta t}{2\pi};\text{ and } S_{22} = \sigma_2^2 \frac{\Delta t}{2\pi} \tag{4.65}$$

Using these relationships, we can rewrite Equation (4.62) for the *N*-th mode in the following form

$$\ddot{\eta}_N + f(\eta_N, \dot{\eta}_N) = b_j(\eta_N, \dot{\eta}_N) W_j(\mathrm{t}) \qquad j = 0,1,2 \tag{4.66}$$

where the repeated index "*j*" implies summation and assuming that the nonlinear terms in $F_N^{NL}$ are also functions of $\eta_N$ and/or $\dot{\eta}_N$. In general, the damping and stiffness of the system are included in the internal force function $f(\eta_N, \dot{\eta}_N)$. The right hand side of Equation (4.66) also includes excitation $W_j(t)$ due to white noise processes that is multiplied by the excitation coefficient functions, $b_j(\eta_N, \dot{\eta}_N)$. When we measure the system response and estimate the system parameters via SID techniques, the estimated parameters are called *apparent* values. Since parametric excitation is assumed to have influence upon the apparent damping and/or stiffness, an *effective* value for these parameters needs to be estimated.

To determine these effects, we follow the work of Zhu and Lin[47]. First, we recall the definition of the covariance function of white noise processes given by

$$E[W_i(t) W_j(\mathrm{t}+\tau)] = 2\pi \mathrm{S}_{ij} \delta(\tau) \tag{4.67}$$

where $E[.]$ is the mean (or expected) value operator, $\mathrm{S}_{ij}$ is the correlation between the noise processes and $\mathrm{S}_{ii} = \mathrm{S}_i$ is the intensity of the noise. Using the above definition, we can replace Equation (4.66) by

$$\ddot{\eta}_N + f(\eta_N, \dot{\eta}_N) = \sigma(\eta_N, \dot{\eta}_N) W(\mathrm{t}) \tag{4.68}$$

where $W(\mathrm{t})$ is a unit white noise (zero mean and unit variance) and $\sigma(\eta_N, \dot{\eta}_N)$ is called the excitation amplitude function defined as[48]

$$\sigma^2(\eta_N, \dot{\eta}_N) = 2\pi S_{ij} b_i(\eta_N, \dot{\eta}_N) b_j(\eta_N, \dot{\eta}_N) \tag{4.69}$$

Next, multiplying Equation (4.68) by $\dot{\eta}_N$ we obtain

$$\begin{aligned} &\ddot{\eta}_N\dot{\eta}_N + f(\eta_N,\dot{\eta}_N)\dot{\eta}_N = \sigma(\eta_N,\dot{\eta}_N)W(\mathrm{t})\dot{\eta}_N \\ &\Rightarrow \frac{d}{dt}\left[\frac{1}{2}\dot{\eta}_N^2 + \int_0^{\eta_N} g(x)dx\right] = \sigma(\eta_N,\dot{\eta}_N)W(\mathrm{t})\dot{\eta}_N - [f(\eta_N,\dot{\eta}_N) + g(\eta_N)]\dot{\eta}_N \end{aligned} \tag{4.70}$$

where $g(\eta_N)$ is the stiffness function, so that $G(\eta_N) = \int_0^{\eta_N} g(x)dx$ defines the potential energy in the system. Equation (4.70) can be rewritten in the form of an energy balance equation

$$\frac{d\Lambda}{dt} = \sigma(\eta_N,\dot{\eta}_N)W(\mathrm{t})\dot{\eta}_N - [f(\eta_N,\dot{\eta}_N) + g(\eta_N)]\dot{\eta}_N \tag{4.71}$$

where $\Lambda$ is the mechanical energy of the system.

Taking the expected value of Equation (4.71) conditional to a certain displacement level, and applying results from the associated non-homogeneous Fokker-Planck equation, Zhu and Lin[47] derived the following expression for the effective stiffness function of the system

$$g(\eta_N) = \int_{-\infty}^{+\infty}\left[f(\eta_N,\dot{\eta}_N) - \frac{1}{4}\frac{\partial\sigma^2(\eta_N,\dot{\eta}_N)}{\partial\dot{\eta}}\right]p_{\dot{\eta}_N|\eta_N}d\dot{\eta}_N \tag{4.72}$$

where $p_{\dot{\eta}_N|\eta_N}$ is the marginal probability density of $\dot{\eta}_N$ for a given value of $\eta_N$. The second term inside the integral is the well known Wong-Zakai[48] correction of the internal force function and it accounts for the presence of parametric noise in the system.

Similarly, taking the expected value of Equation (4.71) conditional to a certain mechanical energy level, Zhu and Lin[47] derived the following expression for the effective damping ratio of the system

$$\varsigma = \frac{1}{\Lambda}\int_{-\infty}^{+\infty}\left[f(\eta_N,\dot{\eta}_N)\dot{\eta}_N - \frac{1}{4}\frac{\partial\sigma^2(\eta_N,\dot{\eta}_N)}{\partial\dot{\eta}}\right]p_{\dot{\eta}_N|\Lambda}d\dot{\eta}_N \tag{4.73}$$

where $p_{\dot{\eta}_N|\Lambda}$ is the marginal probability density of $\dot{\eta}_N$ for a given energy level, $\Lambda$. Again, the second term inside the integral is the Wong-Zakai[48] correction of the internal force function and which accounts for the presence of parametric noise in the system.

A practical application of these equations was performed by Rudinger and Krenk[49] who have estimated the effective stiffness and damping of a linear stochastically excited system with additive and parametric noises represented by

$$\ddot{X} + [2\xi\omega_0 - W_2(t)]\dot{X} + [\omega_0^2 - W_1(t)]X = W_0(t) \tag{4.74}$$

In this case, the excitation amplitude function is given by[49]

$$\sigma^2(X, \dot{X}) = 2\pi(S_{00} + X^2 S_{11} + 2X\dot{X}S_{12} + \dot{X}^2 S_{22}) \tag{4.75}$$

Applying Equations (4.72) and (4.73) they derived the following expressions for the effective stiffness and damping of the system represented by Equation (4.74)

$$g(X) = (1 - \pi \frac{S_{12}}{\omega_0^2})\omega_0^2 X \tag{4.76}$$

$$\xi_{eff} = \xi - \frac{1}{2}\pi \frac{S_{22}}{\omega_0^3} \tag{4.77}$$

Equation (4.76) shows that the correction in the stiffness due to parametric noise depends on the correlation of the two parametric noise processes (i.e., $W_1(t)$ and $W_2(t)$). This result has also been reported for more complex system involving nonlinearities[28]. Since we assumed that the noise sources are mutually independent (i.e., $S_{12} = 0$) their influence upon the effective natural angular frequency of the system vanishes according to the Equation (4.76).

Equation (4.77) indicates that the effective damping depends on the spectral intensity of the parametric noise $W_2(t)$. For sufficiently large values of the spectral

intensity of the parametric noise, the effective damping is smaller than the actual damping of the system. This is also known as noise-induced drift. There is also the possibility of destabilization of a stable system ($\xi > 0$) by parametric excitations, since the effective damping can be negative. So, the parametric excitation, $W_2(t)$, would have impact upon the dynamical behavior of the system.

However, for usual values of noise spectral intensity, the correction presented in Equation (4.77) is very small. In Chapter 5 we will present some results which confirm this small effect. Therefore, we moved the parametric excitation from the right hand side of our model equation and lumped its effect on an effective damping ratio. The stiffness is also represented by an effective stiffness which accounts for the frequency shift. With the simplifications and notations presented above, Equation (4.62) reduces to

$$\ddot{\eta}_N + 2\tilde{\xi}_N \tilde{\omega}_N \dot{\eta}_N + \tilde{\omega}_N^2 \eta_N + \sum_{i=1}^{N_m}\sum_{j=1}^{N_m}(A_{Nij}\dot{\eta}_i\dot{\eta}_j + B_{Nij}\eta_i\eta_j) = (F_N)^{\mathrm{NL}} + \sigma_{0,N}W \quad N = 1,2,...,N_m \quad (4.78)$$

where $\tilde{(\,)}$ represents effective values.

### 4.3.2 Flame Dynamics

As mentioned before, $(F_N)^{\mathrm{NL}}$ contains processes that need to be modeled. In this research we focused on presenting a model only for the most important process, which accounts for the influence of the unsteady heat release associated with the chemical reactivity of the flow. The temporal rate of change of the heat release, also referred as flame dynamics, is the most complex part of the modeling process due to the complexity of chemical kinetics and physical transport processes. Experiments have shown that acoustic modes are excited with harmonics and sub-harmonics due to nonlinear flame

effects. Some other frequency peaks and modulations can also be introduced by flame dynamics.

Fluctuations in the rate of heat release appears in $(F_N)^{\mathrm{NL}}$ as the following energy addition term[11]

$$(F)^{NL} \cong F_N^Q = \frac{\gamma - 1}{\overline{p} E_N^2} \iiint_V \psi_N \frac{\partial \dot{Q}'}{\partial t} dV \tag{4.79}$$

where the rate of heat release, $\dot{Q}'$, depends on local fluctuations of the flow variables. Therefore, it cannot be determined just from elementary considerations of chemical kinetics.

The first model describing the coupling between heat release and flow-field perturbations in liquid-fueled systems was proposed by Crocco[11] and it is referred to as the time-lag or $n-\tau$ model. The model assumes that at time $t$ the pressure in the combustor chamber suddenly decreases, causing an increase in fuel flow through the injectors. The increased mass burns at some later time ($t+\tau$), where $\tau$ is the time lag.

The presence of the time delay transforms the dynamical system equations into a set of stochastic differential delay equations (SDDEs). Systems with delays, commonly called infinite-dimension systems, impose some restrictions upon the application of SID techniques. In general, only input-output identification can be applied in this case. As in this work we are primarily interested in performing stochastic system identification, a finite-dimension model needs to be presented.

More details about the flame dynamics model used in this research will be presented in Chapter 6. Here, we just assume that the heat release is uniformly distributed in a small region close to the injector plate. The dimensions of this region depend on the

type of excited mode. For example, if a longitudinal is excited we can assume that the heat release is uniformly distributed in a thin sheet located at $x_f$ downstream the injector plate. So, for a longitudinal mode Equation (4.79) can be rewritten as

$$F_N^Q = \frac{\gamma-1}{\bar{p}E_N^2}\iiint_V \psi_N \frac{\partial \dot{Q}'}{\partial t} dV = \frac{\gamma-1}{\bar{p}E_N^2}\iiint_V \psi_N \frac{\partial \dot{Q}'_f(t)\delta(x-x_f)}{\partial t} dV = a_N \frac{\partial \dot{Q}'_f}{\partial t} \tag{4.80}$$

where $\frac{\partial \dot{Q}'_f}{\partial t} = \frac{\partial \dot{Q}'}{\partial t}\bigg|_{x=x_f}$, $a_N = \frac{\gamma-1}{\bar{p}E_N^2} A_{ch}\psi_N(x_f)$, and $A_{ch}$ is the transversal area of the chamber.

We also anticipate that the dynamics of the heat release oscillations will be represented by a nonlinear dependence upon the acoustic velocity given by the following expression

$$\frac{d\dot{Q}'_f}{dt} = g(\dot{Q}'_f, \dot{\eta}_1, \ldots, \dot{\eta}_{N_m}) \tag{4.81}$$

### 4.4 The Finite-dimensional Model

The amplitude of the dynamic pressure oscillations measured by the pressure transducers is the synthesis of all the excited modes. To account for the presence of measurement noise, the measured dynamic pressure oscillations are expressed by

$$p'_j(\mathbf{r}_j, t) = \bar{p}\sum_{i=1}^{N_m} \eta_i(t)\psi_i(\mathbf{r}_j) + e_j(t) \tag{4.82}$$

where $p'_j$ represents the pressure measured by the j-th sensor, $e_j(t)$ is the corresponding noise from measurements which is also assumed ZMWN, and $\psi_i(\mathbf{r}_j)$ is the mode shape of he mode calculated at the j-th sensor location. The mode shapes are given by

$$\psi_i(\mathbf{r}) = \psi_{pmn}(x, r, \theta) = \cos(k_p x)\cos(m\theta)J_m(\kappa_{mn} r) \tag{4.83}$$

The subscripts *p*, *m*, *n* correspond to the longitudinal, tangential and radial modes respectively and $J_m$ is the Bessel function of first kind and order *m*. The values of transverse wave numbers, $\kappa_{mn}$, are calculated by solving the boundary condition which ensures that the radial velocity vanishes at the wall

$$\left.\frac{dJ_m(\kappa_{mn}r)}{dr}\right|_{r=R} = 0 \tag{4.84}$$

Therefore, substituting Equation (4.80) into (4.78), the complete finite-dimensional gray-box model for the LRECS with $N_m$ excited modes is described by the following set of equations:

$$\ddot{\eta}_N + 2\tilde{\xi}_N\tilde{\omega}_N\dot{\eta}_N + \tilde{\omega}_N^2\eta_N + \sum_{i=1}^{N_m}\sum_{j=1}^{N_m}(A_{Nij}\dot{\eta}_i\dot{\eta}_j + B_{Nij}\eta_i\eta_j) = a_N\frac{d\dot{Q}'_f}{dt} + \sigma_{0,N}W \quad N = 1,2,...,N_m \tag{4.85a}$$

$$\frac{d\dot{Q}'_f}{dt} = g(\dot{Q}'_f, \dot{\eta}_1, \ldots, \dot{\eta}_{N_m}) \tag{4.85b}$$

$$p'_j(\mathbf{r}_j, t) = \bar{p}\sum_{i=1}^{N_m}\eta_i(t)\psi_i(\mathbf{r}_j) + e_j(t) \tag{4.85c}$$

The model just presented has some of the main features of a thermoacoustic instability problem. The combustor acoustic modes are excited by the inherent combustion noise and by the unsteady heat release, as shown in Equation (4.85a). Additionally, the unsteady heat release is coupled with the combustor acoustics by the acoustic velocity fluctuations as given by the Equation (4.85b). Thus, there is feedback between the unsteady heat release and the acoustics. Clearly, the number of parameters that need to be estimated in this model is very large. Depending on the flame dynamics model, the number of parameters to be estimated can be even larger, even if only a few excited modes are considered.

## 4.5 Numerical Simulations

The gray-box dynamical model for the LRECS is represented by Equations (4.85a-c). The next step in this research is the implementation of appropriate system identification (SID) technique, which would fit the experimental data to the dynamical model providing estimates of the models parameters. Using such approach it is necessary to determine the accuracy of those parameters estimates. Therefore, before applying any SID technique to the experimental data, the accuracy of the estimated parameters should be evaluated. A reasonable way for performing such an evaluation is to apply the developed SID technique to a numerically simulated response of the system.

The main aspect to be taken into account when performing numerical simulations of this system is the presence of the stochastic differential equations. SDEs appear in various disciplines in sciences and engineering and usually have two additive terms. The first, the so-called drift term, describes a deterministic function of the state variables and model parameters. The second term, the so called noise term or in a slightly narrower sense the diffusion term, describes a stochastic function. A clearer distinction between these two terms will be given next when representing the system in matrix form.

The main issue about solving SDEs numerically is the fact that the rules of deterministic calculus do not apply to stochastic calculus. Consequently, the use of conventional ODEs solvers is not recommended. In order to solve numerically the system of SDEs, we need to use the proper mathematical tools.

Firstly, we define the following vector of state variables

$$\mathbf{x_t} = \mathbf{x(t)} = [\eta_1 \quad \dots \quad \eta_{N_m} \quad \frac{d\eta_1}{dt} \quad \dots \quad \frac{d\eta_{N_m}}{dt} \quad \dot{Q}]^T \tag{4.86}$$

Then we represent the system of Equations (4.85a-c) in the following generic matrix form

$$\dot{\mathbf{x}}_t = \mathbf{f}(\mathbf{x}_t, \boldsymbol{\theta}) + \mathbf{g}(\mathbf{x}_t, \boldsymbol{\theta})\mathbf{W}_t \Rightarrow d\mathbf{x}_t = \mathbf{f}(\mathbf{x}_t, \boldsymbol{\theta})dt + \mathbf{g}(\mathbf{x}_t, \boldsymbol{\theta})\mathbf{W}_t dt \tag{4.87}$$

where $\boldsymbol{\theta} \in |^p$ is the vector of model parameters, $\mathbf{f}(\mathbf{x}_t, \boldsymbol{\theta}) \in \mathbb{R}^{2N_m+1}$ is the vector of drift functions given by

$$\mathbf{f}(\mathbf{x}_t, \boldsymbol{\theta}) = [\dot{\eta}_1 \quad \cdots \quad \cdots \quad \dot{\eta}_{N_m} \quad f_1(\mathbf{x}_t, \boldsymbol{\theta}) \quad \cdots \quad f_{N_m}(\mathbf{x}_t, \boldsymbol{\theta}) \quad f_{\dot{Q}'}(\mathbf{x}_t, \boldsymbol{\theta})]^T \tag{4.88}$$

$\mathbf{g}(\mathbf{x}_t, \boldsymbol{\theta}) \in \mathbb{R}^{2N_m+1 \times 2N_m+1}$ is the diagonal matrix of diffusion or noise functions defined as

$$\mathbf{g}(\mathbf{x}_t, \boldsymbol{\theta}) = \begin{bmatrix} 0 & 0 & 0 & \cdots & \cdots & 0 & 0 & 0 \\ 0 & \ddots & & & & & & 0 \\ 0 & & 0 & & & & & 0 \\ \vdots & & & 0 & & & & \vdots \\ \vdots & & & & g_1(\mathbf{x}_t, \boldsymbol{\theta}) & & & \vdots \\ 0 & & & & & \ddots & & 0 \\ 0 & & & & & & g_{N_m}(\mathbf{x}_t, \boldsymbol{\theta}) & 0 \\ 0 & 0 & 0 & \cdots & \cdots & 0 & 0 & 0 \end{bmatrix} \tag{4.89}$$

and $\mathbf{W}_t \in \mathbb{R}^{2N_m+1}$ is a vector of standard Wiener process (unit ZMWN).

$$\mathbf{W}_t = [0 \quad \cdots \quad 0 \quad 0 \quad W_1(t) \quad \cdots \quad W_{N_m}(t) \quad 0]^T \tag{4.90}$$

The definition of a standard Wiener process (also called Brownian motion), $W(t) = W_t$ on $[0,T]$, requires that $W(0) = W_0 = 0$ and for any $0 \le s < t \le T$, the increment $W_t - W_s$ is a Gaussian random variable with zero mean and variance equal to *t*-*s*. For numerical purposes we discretized the Wiener process in a time step $dt$ such that

$$dW_t = \sqrt{dt}\, N(0,1) \tag{4.91}$$

where $N(0,1)$ is the standard normal Gaussian distribution.

Since $W_n(t)$ were assumed to be ZMWN with variances $\sigma^2_{W_n}$, we can write

$$W_n dt = \sigma_{W_n} N(0,1) dt = \sigma_{W_n} \sqrt{dt}\, dW_t = \sigma_n dW_t \tag{4.92}$$

Substituting Equation (4.92) into (4.87) provides the system in Ito formulation[50]

$$d\mathbf{x_t} = \mathbf{f}(\mathbf{x_t}, \boldsymbol{\theta}) dt + \boldsymbol{\sigma}\mathbf{g}(\mathbf{x_t}, \boldsymbol{\theta}) \mathbf{dW_t} \tag{4.93}$$

where $\mathbf{dW_t} \in \mathbb{R}^{2N_m+1}$ is a standard Wiener increment vector and $\boldsymbol{\sigma} \in \mathbb{R}^{2N_m+1 \times 2N_m+1}$ is a diagonal matrix of noise intensities. However, the solution of the system in Ito formulation is accurate when there is no parametric noise; i.e., when $\mathbf{g} = \mathbf{g}(\boldsymbol{\theta})$. This is the case in our developed model. When parametric noise is taken into account, there will be a correlation between the noise and the system response, and the Stratonovich[50] formulation should be used. The system in the Ito formulation given by Equation (4.93) can be converted to the Stratonovich formulation as

$$d\mathbf{x_t} = \bar{\mathbf{f}}(\mathbf{x_t}, \boldsymbol{\theta}) dt + \boldsymbol{\sigma}\mathbf{g}(\mathbf{x_t}, \boldsymbol{\theta}) \circ \mathbf{dW_t} \tag{4.94}$$

where

$$\bar{f}_i(\mathbf{x_t}, \boldsymbol{\theta}) = f_i(\mathbf{x_t}, \boldsymbol{\theta}) - \frac{1}{2} \sum_{j=1}^{2N_m+2} \sum_{k=1}^{2N_m+2} g_{jk}(\mathbf{x_t}, \boldsymbol{\theta}) \frac{\partial g_{jk}}{\partial x_j}(\mathbf{x_t}, \boldsymbol{\theta}), \qquad i = 1, \ldots, 2N_m \tag{4.95}$$

A MATLAB® code was developed to solve the system of SDEs in both Ito and Stratonovich formulations. We need to provide the following inputs: the number of excited modes; drift and diffusion functions (and corresponding parameters); intensity of the noise excitations; initial state variables vector; initial and final times; sampling time; and number of outputs with corresponding intensities of the measurement noises. The program provides state variable vectors as solutions according to the number of simulated outputs. The simulated response at each output of the system is obtained by summing the solutions for all mode amplitudes ($\eta_1, \ldots, \eta_{N_m}$) multiplied by the corresponding mode shapes and adding a ZMWN.

# CHAPTER 5

# LINEAR SYSTEM APPROXIMATION

Initially, to study the validity of the developed approach, this study investigated the "linear version" of the developed model. Specifically, we simplified the developed model as much as possible, while still accounting for critical physical processes describing the system. This initial study is discussed in this chapter.

Experimental results have shown that under stable operating conditions the amplitudes of the oscillations are small. Combustion chambers are nonlinear dynamical systems in which the nonlinear processes determine the dependence of the balance between energy added to and dissipated by the system upon the amplitude of the oscillations. For small values of the amplitude the curves representing addition and dissipation of energy can be approximated by straight lines and nonlinear effects can be neglected, implying that terms involving coupling between modes can be neglected. Similar approach was used in the works of Karmalita and Furletov[30] and Lieuwen[33].

Consequently, under stable conditions the LRECS would be a stochastically excited linear system, which is described by the following dynamical model based on Equations (4.85a-c)

$$\ddot{\eta}_N + 2\tilde{\xi}_N \tilde{\omega}_N \dot{\eta}_N + \tilde{\omega}_N^2 \eta_N = \sigma_{0,N} W \quad N = 1,2,...,N_m \tag{5.1}$$

$$p'_j(\mathbf{r}_j, t) = \overline{p} \sum_{i=1}^{N_m} \eta_i(t) \psi_i(\mathbf{r}_j) + e_j(t) \tag{5.2}$$

## 5.1 State-Space Representation

The behavior of such a dynamical system is primarily determined by the modal effective damping ratios and angular frequencies. In this study, a different representation of the model will be carried out so that a specific SID technique can be implemented to estimate the modal parameters.

Following the approach for the derivation of Equation (4.87), we rewrite Equation (5.1) as

$$\dot{\mathbf{x}}_\mathbf{t} = \mathbf{f}(\mathbf{x}_\mathbf{t}, \boldsymbol{\theta}) + \mathbf{W}_\mathbf{t} = \begin{bmatrix} \mathbf{O} & \mathbf{I} \\ -\mathbf{K} & -\mathbf{C} \end{bmatrix} \mathbf{x}_\mathbf{t} + \mathbf{W}_\mathbf{t} \Rightarrow \dot{\mathbf{x}}_\mathbf{t} = \mathbf{A}_\mathbf{c}\mathbf{x}_\mathbf{t} + \mathbf{W}_\mathbf{t} \tag{5.3}$$

where the state variable vector, $\mathbf{x}_\mathbf{t} \in \mathbb{R}^{2N_m}$, is

$$\mathbf{x}_\mathbf{t} = [\eta_1 \quad \cdots \quad \eta_{N_m} \quad \frac{d\eta_1}{dt} \quad \cdots \quad \frac{d\eta_{N_m}}{dt}]^T \tag{5.4}$$

$\mathbf{K} \in \mathbb{R}^{N_m \times N_m}$ is the mass-normalized stiffness matrix

$$\mathbf{K} = \begin{bmatrix} \tilde{\omega}_1^2 & 0 & \cdots & 0 \\ 0 & \tilde{\omega}_2^2 & \cdots & 0 \\ \vdots & \vdots & \ddots & \vdots \\ 0 & 0 & \cdots & \tilde{\omega}_N^2 \end{bmatrix} \tag{5.5}$$

$\mathbf{C} \in \mathbb{R}^{N_m \times N_m}$ is the mass-normalized damping matrix

$$\mathbf{C} = \begin{bmatrix} 2\tilde{\xi}_1\tilde{\omega}_1 & 0 & \cdots & 0 \\ 0 & 2\tilde{\xi}_2\tilde{\omega}_2 & \cdots & 0 \\ \vdots & \vdots & \ddots & \vdots \\ 0 & 0 & \cdots & 2\tilde{\xi}_N\tilde{\omega}_N \end{bmatrix} \tag{5.6}$$

$\mathbf{W}_\mathbf{t} \in \mathbb{R}^{2N_m}$ is a vector of standard Wiener process (unit ZMWN)

$$\mathbf{W}_\mathbf{t} = [0 \quad \cdots \quad 0 \quad W_1(t) \quad \cdots \quad W_{N_m}(t)]^T \tag{5.7}$$

$\mathbf{O} \in \mathbb{R}^{N_m \times N_m}$ is a matrix of zeros, $\mathbf{I} \in \mathbb{R}^{N_m \times N_m}$ is the identity matrix, and $\mathbf{A_c} \in \mathbb{R}^{2N_m \times 2N_m}$ is the continuous-time state space matrix.

Assuming the system's response is simultaneously measured by "*L*" sensors placed at different positions in the combustor, we can rewrite Equation (4.82) as follows

$$[p_1(t) \quad \dots \quad p_L(t)]^T = \begin{bmatrix} \coprod & \mathbf{O} \end{bmatrix} \mathbf{x_t} + [e_1(t) \quad \dots \quad e_L(t)]^T \Rightarrow \mathbf{y_t} = \mathbf{C_c x_t} + \mathbf{e_t} \tag{5.8}$$

where $\coprod \in \mathbb{R}^{L \times N_m}$ is a matrix whose rows are formed by the row vector $[\overline{p}\psi_1(\mathbf{r_j}) \quad \cdots \quad \overline{p}\psi_{N_m}(\mathbf{r_j})]$, $\mathbf{O} \in \mathbb{R}^{L \times N_m}$ is a matrix of zeros, $\mathbf{y_t} \in \mathbb{R}^L$ is the continuous time output vector, $\mathbf{C_c} \in \mathbb{R}^{L \times 2N_m}$ is the observation matrix, and $\mathbf{e_t} \in \mathbb{R}^L$ is the vector of continuous time measurement noises.

Equations (5.3) and (5.8) form the *continuous-time stochastic state space model* of the system, which are repeated below for convenience

$$\begin{aligned} \dot{\mathbf{x}}_\mathbf{t} &= \mathbf{A_c x_t} + \mathbf{W_t} \\ \mathbf{y_t} &= \mathbf{C_c x_t} + \mathbf{e_t} \end{aligned} \tag{5.9}$$

Consider now the eigenvalue decomposition of the state space matrix $\mathbf{A_c}$ resulting from the standard eigenvalue problem

$$\mathbf{A_c \psi} = \boldsymbol{\psi \Lambda_c} \Rightarrow \mathbf{A_c} = \boldsymbol{\psi \Lambda_c \psi^{-1}} \tag{5.10}$$

where $\mathbf{\Lambda_c} \in \mathbb{C}^{2N_m \times 2N_m}$ is a diagonal matrix of complex continuous-time eigenvalues, $\lambda_j \in \mathbb{C}$ $(j = 1,\ldots,2N_m)$, and $\mathbf{\Psi} \in \mathbb{C}^{2N_m \times 2N_m}$ is a modal matrix containing the corresponding eigenvectors of $\mathbf{A_c}$. Andersen[51] presented a good derivation showing that the effective angular frequencies and damping ratios of the *N*-th underdamped mode are related to these complex eigenvalues by the relationships

$$\begin{aligned}\lambda_N &= -\tilde{\xi}_N\tilde{\omega}_N + \tilde{\omega}_N\sqrt{1-\tilde{\xi}_N^2}\,i \\ \lambda_{N_m+N} &= -\tilde{\xi}_N\tilde{\omega}_N - \tilde{\omega}_N\sqrt{1-\tilde{\xi}_N^2}\,i\end{aligned} \quad \text{for} \quad N=1,2,...,N_m. \tag{5.11}$$

and the mode shapes, $\mathbf{V}\in\mathbb{C}^{L\times 2N_m}$ , can be calculated by

$$\mathbf{V}=\mathbf{C}_\mathbf{c}\boldsymbol{\psi} \tag{5.12}$$

While the above derived equations are expressed in continuous time, measured data are taken at discrete time instants. In order to fit models to measurements by applying SID techniques, these models need to be also expressed in discrete time. Discrete models are also needed for performing numerical simulations. If it would be possible to find an analytical solution for the response of a structure to a given input, this analytical expression could be evaluated at any time instant *t*, without the need to convert the model to discrete time. However, in most cases there is no analytical solution and one has to rely upon a numerical solution method to simulate the response of a dynamical system.

We define a fixed sampling period, $\Delta t$ , so that the continuous equations are discretized and solved at all discrete time instants *k*, where $t=k\Delta t,\ k\in\mathbb{N}$ . Typical for the sampling of a continuous time equation is that a certain behavior of the time-dependent variables between two samples has to be assumed. If a zero-order hold (ZOH) assumption is applied, the input is piecewise constant over the sampling period. Under this assumption, the continuous-time state-space model in Equation (5.9) is converted to the *discrete-time state-space model*[51]

$$\begin{aligned}\mathbf{x}_{k+1} &= \mathbf{A}_\mathbf{d}\mathbf{x}_k + \mathbf{W}_k \\ \mathbf{y}_k &= \mathbf{C}_\mathbf{d}\mathbf{x}_k + \mathbf{e}_k\end{aligned} \tag{5.13}$$

where the subscript $k$ indicates sampled or discrete-time vectors. Based upon the assumptions for the continuous time model, the noise vectors are both immeasurable vector signals assumed to be ZMWN so that

$$E\left[\begin{pmatrix}\mathbf{W}_p\\ \mathbf{e}_p\end{pmatrix}\begin{pmatrix}\mathbf{W}_q^T & \mathbf{e}_q^T\end{pmatrix}\right]=\begin{pmatrix}\mathbf{Q} & \mathbf{S}\\ \mathbf{S}^{\mathbf{T}} & \mathbf{R}\end{pmatrix}\delta_{pq} \tag{5.14}$$

where $\mathbf{Q}\in\mathbb{R}^{2N_m\times 2N_m}$, $\mathbf{S}\in\mathbb{R}^{2N_m\times L}$, and $\mathbf{R}\in\mathbb{R}^{L\times L}$ are covariance matrices, $\delta_{pq}$ is the Kronecker delta and $p$ and $q$ are two arbitrary time instants.

Therefore, the SID technique will estimate the discrete-time matrices $\mathbf{A_d}$ and $\mathbf{C_d}$. They are related to their continuous time counterparts by[25]

$$\mathbf{A_d}=e^{\mathbf{A_c}\Delta t} \tag{5.15}$$

$$\mathbf{C_d}=\mathbf{C_c} \tag{5.16}$$

Consequently, the eigenvalue decomposition of the discrete state matrix $\mathbf{A_d}$ can be found by inserting the eigenvalue decomposition of the continuous state matrix $\mathbf{A_c}$ into Equation (5.15) and applying the series expansion of the exponential function as

$$\mathbf{A_d}=e^{\mathbf{\Psi\Lambda_c\Psi^{-1}}\Delta t}=\Psi e^{\mathbf{\Lambda_c}\Delta t}\Psi^{\mathbf{-1}}=\Psi\mathbf{\Lambda_d}\Psi^{\mathbf{-1}} \tag{5.17}$$

One may note that the discrete eigenvectors are equal to the continuous ones. Consequently, the observed mode shapes are the same in discrete as in continuous time and estimated by

$$\mathbf{V}=\mathbf{C_d}\boldsymbol{\psi} \tag{5.18}$$

Equation (5.17) implies that the discrete eigenvalues, which we denote as $\mu_j$, are related to the continuous eigenvalues by the following relationship:

$$\begin{bmatrix} \mu_1 & \cdots & 0 \\ \vdots & \ddots & \vdots \\ 0 & \cdots & \mu_{2N_m} \end{bmatrix} = \mathbf{\Lambda_d} = e^{\mathbf{\Lambda_c}\Delta t} \Rightarrow \mu_j = e^{\lambda_j \Delta t} \Rightarrow \lambda_j = \frac{\ln \mu_j}{\Delta t} \tag{5.19}$$

From Equations (5.11) and (5.19) one can realize that the model parameters can also be recovered from the eigendecomposition of the discrete-time matrix $\mathbf{A_d}$, using the following expressions

$$\tilde{\omega}_N = \left|\lambda_N\right| \tag{5.20}$$

$$\tilde{\xi}_N = -\frac{\mathrm{Re}(\lambda_N)}{|\lambda_N|} \tag{5.21}$$

## 5.2 Stochastic Subspace Identification - SSI

The stochastic identification problem is now defined. For a given set of measurements of the output generated by the unknown stochastic system of order $N_m$ (number of excited modes) represented by Equation (5.13) with $\mathbf{W_k}$ and $\mathbf{e_k}$ assumed ZMWN sequences with covariance matrix given by Equation (5.14), we need to determine: the order of the unknown system; that is, the number of excited modes ($N_m$) and the system matrices $\mathbf{A_d} \in \mathbb{R}^{2N_m \times 2N_m}$, $\mathbf{C_d} \in \mathbb{R}^{L \times 2N_m}$, $\mathbf{Q} \in \mathbb{R}^{2N_m \times 2N_m}$, $\mathbf{S} \in \mathbb{R}^{2N_m \times L}$, and $\mathbf{R} \in \mathbb{R}^{L \times L}$. This is exactly what Stochastic Subspace Identification (SSI) algorithms were developed for; that is, they determine state space models from given output-only data.

The SSI technique implemented in this work is a time domain method also called SSI-DATA. It works directly with time-series of experimental data, without the need to convert them to correlations, covariances or spectra. In general, subspace identification methods involve geometric operations on subspaces spanned by the column or row vectors of certain block Hankel matrices formed by the input and/or output data. The

main theorem of the subspace theory shows how the Kalman filter states can be obtained from input and/or output data using tools from linear algebra. The operations are performed numerically in a reliable way based on robust numerical techniques such as singular value decomposition (SVD) and QR factorization[20]. Once these states are known, the identification problem becomes a linear least-squares problem that calculates the system matrices.

The SSI-DATA is considered to be the most powerful class of known identification techniques for modal analysis in the time domain. However, as aforementioned, its mathematical framework presented in the book of Van Overschee and De Moor[24] can be difficult to understand for people with a classical background in structural dynamics. In the following, the SSI-DATA technique will be presented from a stochastic point of view. Specifically, its fundamental steps are presented based on the use of stochastic theory for Gaussian distributed stochastic processes, where everything is completely described by correlation functions in time domain.

Considering the continuous-time stochastic state space model of the system given by Equation (5.9, whose solution can be calculated as

$$\mathbf{x_t} = \exp(\mathbf{A_c} t\mathbf{x}_0) + \int_0^t \exp[\mathbf{A_c}(t-\tau)]\mathbf{W}(\tau)d\tau \tag{5.22}$$

where the first term is the solution to the homogenous equation and the last term is the particular solution. To take this solution to discrete-time, we sampled all variables like $\mathbf{y}_k = \mathbf{y}(k\Delta t)$ so that the solution to the homogenous equation becomes

$$\mathbf{x}_k = \exp(\mathbf{A_c} k\Delta t\mathbf{x}_0) \tag{5.23}$$

Thus, from Equations (5.13), (5.15) and (5.16) we can write

$$\begin{aligned} \mathbf{x}_k &= \exp(\mathbf{A_c} k\Delta t \mathbf{x}_0) = \mathbf{A_d}^k \mathbf{x}_0 \\ \Rightarrow \mathbf{y_k} &= \mathbf{C}\mathbf{A_d}^k \mathbf{x}_0 \end{aligned} \tag{5.24}$$

### 5.2.1 The Block Hankel Matrix

In discrete time, the system response is normally represented by the data matrix

$$\mathbf{Y} = [\mathbf{y_1} \quad \mathbf{y_2} \quad \cdots \quad \mathbf{y_N}] \tag{5.25}$$

where $\mathbf{Y} \in \mathbb{R}^{L \times N}$, $L$ is the number of output sensors, and $N$ is the number of data points. To understand the meaning of the Block Hankel matrix, it is useful to consider a more simple case where we perform the product between two matrices that are modifications of the $N$ data matrix given by Equation (5.25). Let $\mathbf{Y}_{(1:N-k)}$ be the data matrix where we have removed the last $k$ data points, and similarly, let $\mathbf{Y}_{k|N}$ be the data matrix where we have removed the first $k$ data points, then

$$\hat{\mathbf{R}}_k = \frac{1}{n-k} \mathbf{Y}_{(1:N-k)} \mathbf{Y}^{\mathbf{T}}_{(k:N)} \tag{5.26}$$

is an unbiased estimate of the correlation matrix at time lag $k$. This follows directly from the definition of the correlation estimate given by Bendat and Piersol[21, 52]. The Block Hankel matrix defined in SSI-DATA is simply a gathering of a family of matrices that are created by shifting the data matrix

$$\mathbf{Y}_H = \begin{bmatrix} \mathbf{Y}_{(1:N-2s)} \\ \mathbf{Y}_{(2:N-2s+1)} \\ \vdots \\ \mathbf{Y}_{(2s:N)} \end{bmatrix} = \begin{bmatrix} \mathbf{Y}_{Hp} \\ \mathbf{Y}_{Hf} \end{bmatrix} \tag{5.27}$$

The upper half part of this matrix, $\mathbf{Y}_{Hp}$, is called “past” and the lower half part, $\mathbf{Y}_{Hf}$, is called “future”. The total data shift is $2s$ and is denoted “the number of block

rows" (of the upper or lower part of the Block Hankel matrix). The number of rows in the Block Hankel matrix is $2sL$, the number of columns is $N-2s$.

### 5.2.2 The Projections

Overschee and De Moor[24] have introduced the projection as a geometrical tool and explained it in this context. However, one can consider such projection as a conditional mean. Specifically, in SSI-DATA the projection of the future into the past defines the matrix

$$\mathbf{O} = E[\mathbf{Y}_{Hf} \mid \mathbf{Y}_{Hp}] \tag{5.28}$$

The matrix $\mathbf{O}$ is $sL \times sL$. Since we have Gaussian process, Melsa and Sage[53] have shown that this conditional mean can be described by

$$\mathbf{O} = \mathbf{Y}_{Hf}\mathbf{Y}_{Hp}^{T}[\mathbf{Y}_{Hp}\mathbf{Y}_{Hp}^{T}]^{-1}\mathbf{Y}_{Hp} \tag{5.29}$$

The last matrix in this product defines the condition and the first four matrices in the product introduce the covariances between responses at different time lags. Applying Equation (5.24) one can show that any column can be expressed in the following form

$$\mathbf{o}_{col} = \begin{bmatrix} \mathbf{C_d} \\ \mathbf{C_d A_d} \\ \mathbf{C_d A_d^2} \\ \vdots \\ \mathbf{C_d A_d^{s-1}} \end{bmatrix} \mathbf{x_0} = \mathbf{\Gamma_s x_0} \tag{5.30}$$

where $\mathbf{\Gamma_s}$ is called the observability matrix.

### 5.2.3 The Kalman States

Since the Kalman states are simply the initial conditions for all the columns in the matrix **O,** it follows that

$$\mathbf{O} = \mathbf{\Gamma}_s \mathbf{X}_0 \tag{5.31}$$

where the matrix $\mathbf{X}_0$ contains the so defined Kalman states at time lag zero. If we know the matrix $\mathbf{\Gamma}_s$, then we can simply find all the Kalman states directly from Equation (5.31). However, since we do not know this matrix, we have to estimate the states using a different strategy. The trick is to use the singular value decomposition (SVD) of the matrix **O**

$$\mathbf{O} = \mathbf{U}\mathbf{S}\mathbf{V}^{\mathbf{T}} = \mathbf{U}\mathbf{S}^{1/2}\mathbf{S}^{1/2}\mathbf{V}^{\mathbf{T}} \tag{5.32}$$

Now, comparing Equations (5.32) and (5.31), the estimate of the observability matrix and Kalman states at lag zero are given by

$$\begin{aligned} \hat{\mathbf{\Gamma}} &= \mathbf{U}\mathbf{S}^{1/2} \\ \hat{\mathbf{X}}_0 &= \mathbf{S}^{1/2}\mathbf{V}^{\mathbf{T}} \end{aligned} \tag{5.33}$$

The procedure for estimating the matrices $\hat{\mathbf{\Gamma}}$ and $\hat{\mathbf{X}}_0$ in Equation (5.33) is not unique. A certain arbitrary similarity transformation can be shown to influence the individual matrices, but can also be shown not to influence the estimation of the system matrices. The Kalman state matrix just estimated is the Kalman state matrix for time lag zero. After some manipulations, one can show that removing one block row of **O** from the top, and then one block row of $\mathbf{\Gamma}_s$ from the bottom, we can estimate the Kalman state matrix at time lag one; that is, $\hat{\mathbf{X}}_1$. Therefore, by subsequent removal of block rows from **O** all the Kalman states can be defined.

### 5.2.4 Estimation of the System Matrices

The system matrix $\mathbf{A}_d$ can be found from the matrix $\hat{\mathbf{\Gamma}}$ by removing one block from the top and one block from the bottom which yields

$$\hat{\boldsymbol{\Gamma}}_{(2:s)}\hat{\mathbf{A}}_{\mathbf{d}} = \hat{\boldsymbol{\Gamma}}_{(1:s-1)} \tag{5.34}$$

Finally, the estimated system matrix, $\hat{\mathbf{A}}_{\mathbf{d}}$, can be found by regression or least-squares. The estimated observation matrix, $\hat{\mathbf{C}}_{\mathbf{d}}$, can be found simply by taking the first block of the observability matrix as indicated by Equation (5.30), so

$$\hat{\mathbf{C}}_{\mathbf{d}} = \hat{\boldsymbol{\Gamma}}_{(1:1)} \tag{5.35}$$

### 5.2.5 The Model Order

As we have seen earlier, since the number *s* defines the size of the Block Hankel matrix, it also defines the size of the projection matrix **O**. However, this number represents the number of eigenvalues in our model, which defines the model order. The model order letting it equal twice the number of excited modes in the system. If one had performed a preliminary analysis of the measured data, it would be possible to have a priori idea about the model order by counting twice the number of peaks in the spectral analysis. However, in principle, the number of excited modes is unknown. For the SSI-DATA, a typical problem of estimating a parametric model from data is the determination of the dimensions of the state-space or model order.

In order to obtain a reasonable estimate of the model order for a set of measured data, a number of techniques have been developed as guides or aids to SID techniques. Most of these tools require some kind of user interaction, so that the user establishes a maximum model order to be evaluated. Then, data are acquired based upon an assumption that the model order is equal to this maximum and the data is then sequentially evaluated to determine if models order smaller than the maximum adequately describe the data. This is the point at which the user needs to use one (or

some) of the various evaluation aids available to make a decision. If a model with order lower than the actual one is estimated, some of the modes will be missing in the identified system. On the other hand, a higher order model will present some spurious (or noise) modes along with the actual (or structural) modes.

Some of the commonly used techniques are the stability diagram and the mode indication functions. In this thesis we applied a more recent model order evaluation technique involving the estimate of the rank of the matrix of measured data. An estimate of the rank of the matrix of measured data gives a good estimate of the model order of the system. While the rank cannot be calculated in an absolute sense, it can be estimated from the logarithm of the singular value decomposition of the matrix of covariances. For each mode of the system, one singular value should be found by the SVD procedure. The SVD procedure finds the largest singular value first and then successively finds the next largest singular value and so on.

The basic concept is that the singular values should go to zero when the rank of the matrix is exceeded; that is, when no more structural modes are present. However, due to random errors and small inconsistencies in the measured data, the singular values will not become zero but will be very small. Therefore, the rate of change of the singular values is used as an indicator rather than the absolute values. In this sense, each singular value is divided by the previous singular value forming a normalized ratio that will be approximately equal to one if the successive singular values are not changing magnitude. When a rapid decrease in the magnitude of the singular value occurs, the ratio of successive singular values drops as an indicator of rank or model order of the system.

### 5.2.6 Implementation

The SSI-DATA was implemented in a MATLAB® code. The identification process is started by using the subspace method called *N4SID*[23] in the *System Identification Toolbox* of MATLAB®[56].

A common feature when estimating models using *N4SID* is the model order selection plot which opens just after the estimation process has started. As mentioned before, the model order is estimated based on rank estimation. It displays the relative measure of how much each mode (it is related to the model order) contributes to the behavior of the model calculated through the log of the singular values of the matrix of measured data. In general, we look for a gap or sudden drop in the plot, which indicates that higher model orders have little influence upon the system behavior. Figure 19 shows an example in which the range of model orders was defined to be from 1 to 20. Then, the selection plot indicates that model order of two is sufficient to represent the system, indicating that just one excited mode dominates in the system response. As implemented in this thesis, the user need to select the order only once for each set of data describing a different operating conditions, which in our case correspond to a different value of the swirl flow ratio.

The measured dynamic pressure were preprocessed to eliminate linear trends and set their mean value to zero using the *detrend* function in MATLAB®. The data were bandpass filtered around all the frequencies of the theoretical acoustic modes in the LRECS (see Table 3.2). Then, for each one of the filtered modes the peak was determined and the mode was filtered again with a narrower band. The final signal analyzed by SSI-DATA is the summation of all filtered modes.

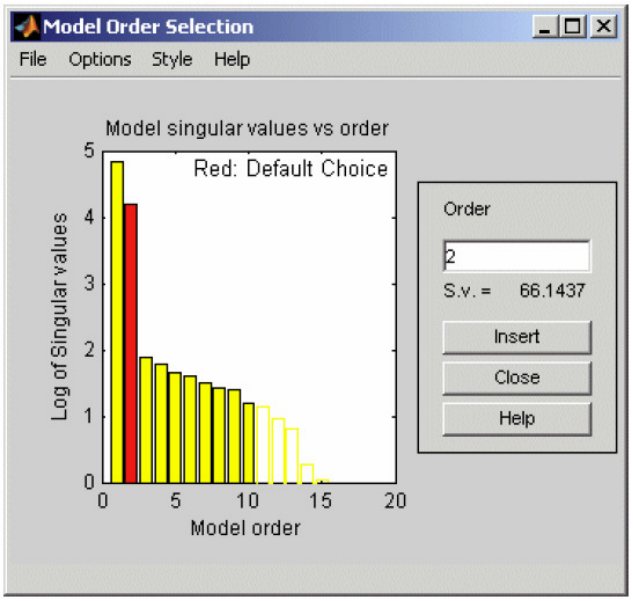


Figure 5.1: Example of the model order selection plot in MATLAB®.

When a subset of data corresponding to a new swirl flow ratio is loaded, the time history and amplitude spectrum are presented on the screen. The code identifies the new control parameter so that sets the range of the model order to 2 to 16 which means that the system could have from 1 to 8 excited modes. That range was chosen taking into account the preliminary information about the system behavior discussed in Chapter 3, which indicates that the largest number of excited modes occurs when the system is stable and eight peaks are present in the spectral analysis.

Several factors such as the signal-to-noise ratio (SNR) in the measured response, and the presence of modes with close frequencies can make the order selection difficult. Consequently, the singular value criteria will select a higher order model and some spurious modes can be estimated. Therefore, to increase the chances that spurious modes are neglected in the parameter estimation, the following additional criteria were implemented as suggested by Asmussen[54]:

1) The eigenvalue of the mode should have a complex conjugate. Structural modes are usually underdamped, so they appear as complex conjugate pairs; and

2) The damping ratio should be below 10%.

### 5.3 SSI-DATA Accuracy

The accuracy of the SSI-DATA technique has been already reported in the literature[25]. However, even though the dynamical model was the same in the cited references as in this linear approximation, the range of frequencies, number of data points and sampling frequency were very different. Consequently, we decided to investigate the accuracy of the estimates using signals with characteristics similar to the ones found in the experimental data from the LRECS.

To investigate the accuracy of the SID technique, several sets of "experimental" data were generated by numerical simulations of the dynamical system using the scheme mentioned in Chapter 4. To limit the number of plots in this work, the analysis was focused on the modes which could be excited in the LRECS. Since the model presents no coupling, we performed simulations of the system response at a fixed frequency and varied the damping ratio, number of data points, and signal-to-noise ratio (SNR) in the response. It should be emphasized that the SNR expresses the ratio between the variance of the signal response ($\sigma^2_{y_k}$) and the variance of the measurement noise ($\sigma^2_{e_k}$).

The following seven frequencies were chosen based on the preliminary analysis in Chapter 3: 600, 1800, 3000, 5000, 8000, and 10000 Hz. The intensity of the additive noise exciting the system was adjusted so that the amplitude of the simulated responses was of the same order of magnitude as the actual ones. This was evaluated via FFT amplitude spectra obtained from pressure sensors for stable operation.

Simulations were performed at fixed sampling frequency ( $f_S$ ) of 48 KHz to match the actual experimental data, and different values of signal-to-noise ratio (SNR). The simulated data corresponding to the given set of values $\tilde{\xi}_n$ , $\tilde{f}_n$ ,and SNR was divided into 20 subsets with *N* data points each. The following values of *N* were tested: 1200; 2400; 3600; 4800; and 6000 data points. The SSI-DATA technique was applied to each subset and averaged values were calculated for the model parameters.

Figure 5.2 shows the results for the estimated damping ratios for a frequency of 8000Hz, when the number of data points in each subset increased from 1200 to 2400. An improvement in the accuracy can be noticed as we compare the results to the straight black line representing the ideal case where simulated and estimated damping ratios have a perfect match. Further increase in the number of data points provided a little improvement in accuracy (less than 5%) which are not plotted to avoid cluttering. However, this small improvement comes at the expense of a much longer computational time. A similar behavior was observed at all other frequencies. Therefore, subsets of 2400 points were chosen to represent a fair trade off between accuracy and computational time.

Figure 5.3 the effect of the SNR upon the accuracy of the estimated. As expected, as the SNR increased the accuracy also increases. For SNR above 100, differences in accuracy at different SNR levels are negligible. At this point we should mention that even though very low values of SNR ratio can present problems when applying any SID technique, preliminary analysis of the experimental data in Chapter 3 showed that at all frequencies of interest the power spectra have clear peaks, indicating that the SNR is larger than 100 (comparing the power or amplitude level of the excited modes to the level

of he background noise in the spectral analysis). Consequently, the SNR was not considered to be a problem for the investigated application of the SID technique.

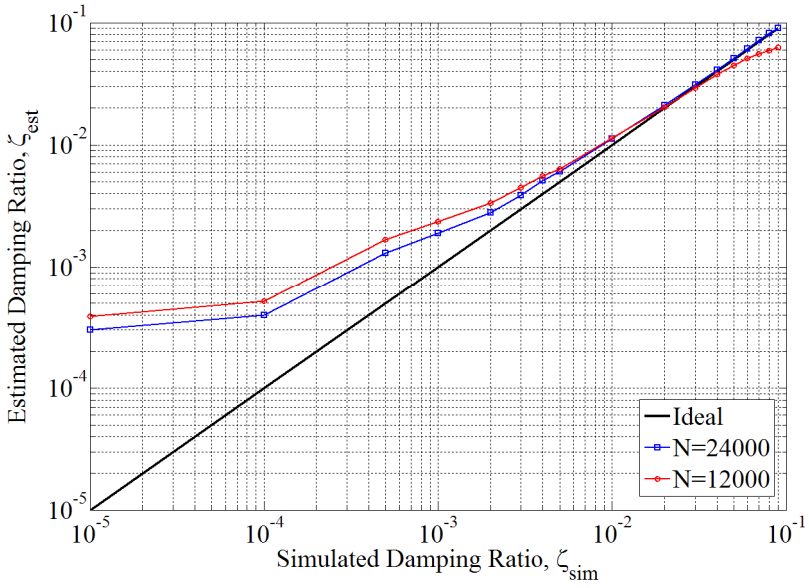


Figure 5.2: Effect of the number of data points in damping estimation for simulated frequency of 8000Hz and SNR = 100.

Figure 5.4 shows the dependence of the estimated frequencies upon changes in simulated damping ratios when the numerical simulations were performed with $SNR = 100$ and the estimations were based on subsets of $N = 2400$ data points. The blue lines represent the simulated frequency (actual values), whereas the green lines represent the estimated values. It shows that for all simulated frequencies and damping ratios the estimated frequencies were overestimated. The maximum error occurred for higher values of damping ratios (close to 0.09) and as the damping decreased the estimated frequencies asymptotically approached a limit value. Notably, the error in the frequency estimation was never above 5%.

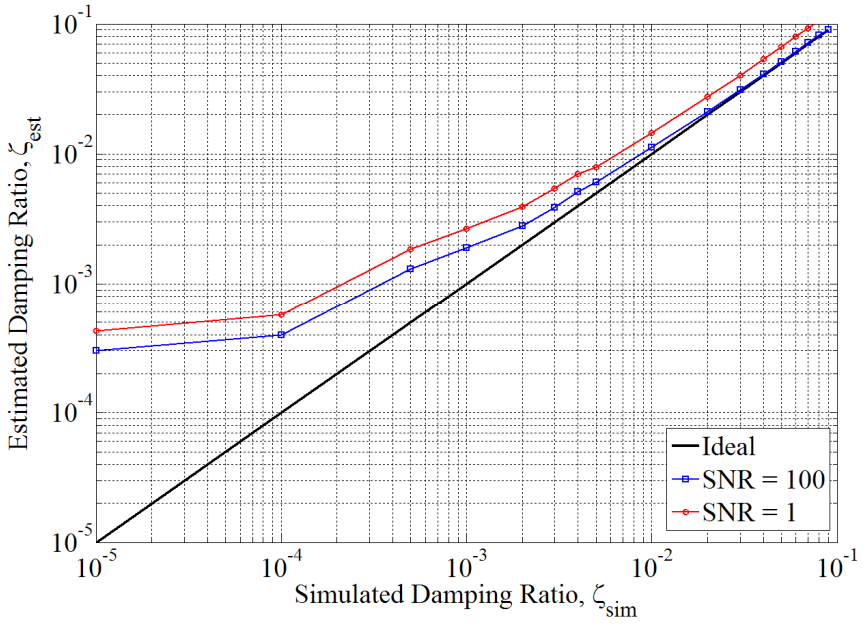


Figure 5.3: Effect of the SNR in damping estimation for simulated frequency of 8000Hz and $N = 2400$.

Figure 5.5 shows the dependence of the estimated damping ratios upon changes in simulated damping ratios (actual values). As a general trend, as the system approaches the stability boundary, the estimates of the damping ratios are less accurate resulting large overestimation of the damping ratios. As we decrease the simulated value of the damping ratio, the estimated damping also decreases but they tend to a certain lower limit whose value is a function of the frequency. The larger the frequency the lower is that limit value.

Investigating the accuracy of the SID techniques, the analysis with numerical simulations can be used to provide some kind of calibration charts. Accordingly, the results presented in Figure 5.5a suggest that an estimated damping ratio of 0.001 for a 600 Hz mode would correspond an actual damping very close to zero (at least below $10^{-4}$). The same value of estimated damping ratio for the 5000 Hz mode would correspond to an actual damping ratio around $6\times10^{-4}$, according to Figure 5.5d.

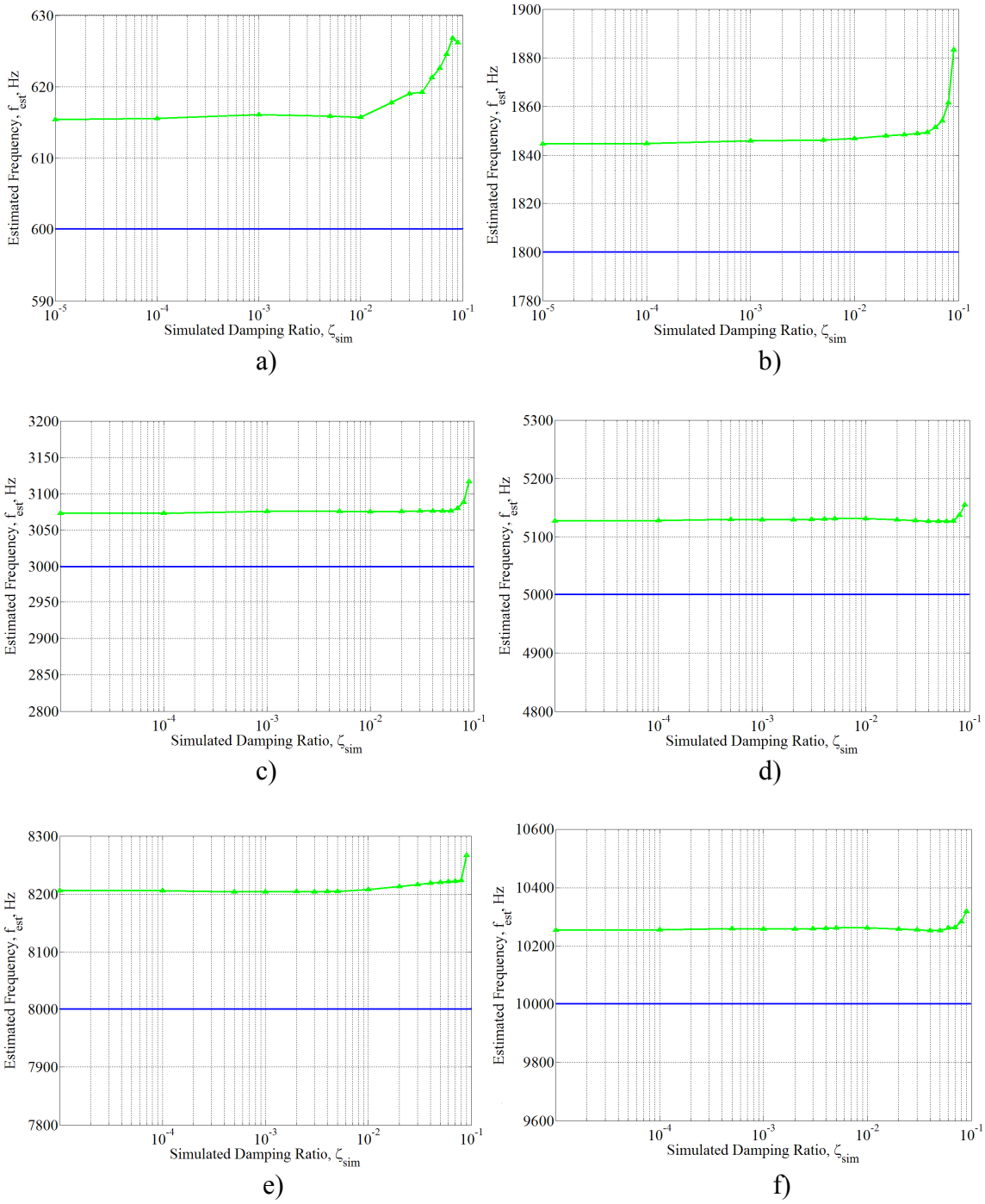


Figure 5.4: Dependence of the estimated frequencies upon changes in simulated damping ratios for $SNR = 100$ and $N = 2400$ and simulated frequencies: a) 600 Hz; b) 1800 Hz; c) 3000 Hz; d) 5000 Hz; e) 8000 Hz; and f) 10000 Hz .

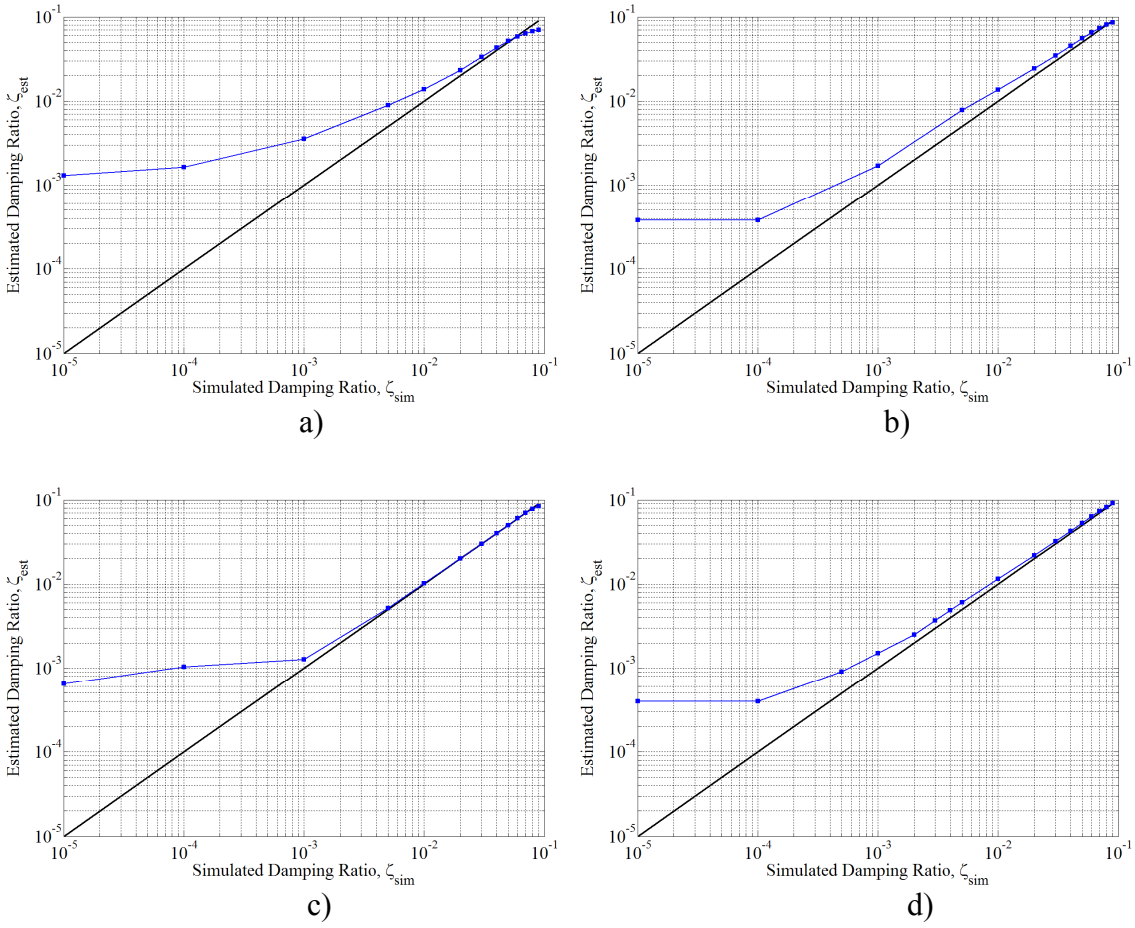


Figure 5.5: Dependence of the estimated damping ratio upon changes in simulated damping ratios for $SNR = 100$, $N = 2400$, and simulated frequencies: a) 600 Hz; b) 1800 Hz; c) 3000 Hz; and d) 5000 Hz.

### 5.3.1 Parametric Noise Investigation

To investigate the effect of parametric noise upon the damping ratio of the linear system, data were generated by numerical simulations of the dynamical system using the scheme discussed in Chapter 4. The model parameters were the same as those used in the investigation of the accuracy of the SSI-DATA technique. However, the system was now excited only by parametric noise ($\Xi_N(t) = \Xi_N^1(t) = 0$ and $\Xi_N^2(t) \neq 0$). Once again, the

intensity of the noise exciting the system was adjusted so that the amplitude of the simulated responses was of the same order of magnitude as the actual ones.

After generating the data by numerical simulations and performing the identification via SSI-DATA to estimate the damping ratios, the intensity of the noise was increased to check the relationship between noise intensity and error in estimation. Table 5.1 shows some of the results.

Table 5.1: Effect of parametric noise upon damping ratio estimates.

| Parametric Noise Intensity | Modal Frequency (Hz) | Simulated Damping Ratio | Estimated Damping Ratio | Effective Damping Ratio (Equation 4.77) |
|---|---|---|---|---|
| $10^4$ | 600 | 0.05 | 0.0496 | 0.049999707 |
| $10^4$ | 1800 | 0.02 | 0.0199 | 0.019999989 |
| $10^4$ | 5000 | 0.005 | 0.00501 | 0.004999999 |
| $10^5$ | 600 | 0.05 | 0.0495 | 0.049997068 |
| $10^5$ | 1800 | 0.02 | 0.0198 | 0.019999891 |
| $10^5$ | 5000 | 0.005 | 0.00507 | 0.004999995 |
| $10^6$ | 600 | 0.05 | 0.0496 | 0.049970682 |
| $10^6$ | 1800 | 0.02 | 0.0196 | 0.019998914 |
| $10^6$ | 5000 | 0.005 | 0.0051 | 0.004999949 |

The results in Table 5.5 indicate that, in most of the cases, the difference between estimated, effective (see Equation 4.77), and “actual” values of the damping ratios are small. In general, for a given frequency, increasing the intensity of the noise decreases the estimated value of the damping ratio. That agrees with the behavior of the effective damping presented in the last column since the correction term given in Equation (4.77) is proportional to the noise intensity. For fixed noise intensity, as the frequency was increased the difference between the estimated and “actual” values decreased. Once

again, this agrees with the behavior of the effective damping presented in the last column since the correction term given in Equation (4.77) is inversely proportional to the frequency cubic. For high values of frequency such as 5000 Hz the correction term is so small, that the estimated value is actually larger than the "actual" value. Overall, the corrections are small within the margin of error of the estimations. Therefore, it is valid the idea of lumping the effect of parametric noise upon the damping ration and work with an effective damping.

### 5.4 Experimental Results and Operational Stability Margin

The SSI-DATA technique was applied to the experimental data discussed in Chapter 3. For a truly linear dynamical system, the effective damping ratio can be used as a operational stability margin parameter, since the system becomes unstable when the damping ratio becomes negative. Therefore, as discussed earlier a zero value for the effective damping ratio characterizes the stability boundary.

For each of the identified modes in the system, a plot should be constructed which shows the dependence of the estimated damping ratios upon the swirl flow ratio parameter. Such plots can be then used to predict if a mode is approaching the stability boundary as we change the swirl flow ratio parameter and which mode tends to be unstable first.

In the preliminary analysis of the experimental data in Chapter 3, it was observed that during stable operation the quarter wave longitudinal mode was dominant. In fact, as the swirl flow ratio decreased the amplitude of the peak corresponding to that mode increased. Other modes exhibited similar behavior, although with much smaller peak

amplitudes. This raises the question: why did the first tangential mode become unstable before the longitudinal mode?

In our simple model, without nonlinearities or mode coupling, the behavior of each mode is totally defined by its damping ratio. Figures 5.6 and 5.7 show the dependence of the estimated effective damping ratios of the longitudinal and tangential modes upon the swirl flow ratio parameter. In both cases the damping decreased as the swirl flow ratio parameter decreased indicating that the modes were becoming unstable. However, as soon as the system reaches the unstable regime, the behavior of the two estimated effective damping ratios become distinct.

Figure 5.6 shows that the estimated effective damping ratio of the longitudinal mode decreases towards a zero value as $K$ decreases. However, as soon as the tangential mode became unstable its amplitude increased suddenly and its harmonics started to be more pronounced in the power spectra, and the longitudinal mode was no longer the dominant mode in the system. Consequently, the estimated damping for the longitudinal mode increased dramatically (to above 10%) and the SSI-DATA could not consider it in the calculations. Thus, we only have damping estimates for the longitudinal mode until the onset of the instability.

Analysis of Figure 5.7 shows that the estimated effective damping ratio for the tangential mode also approaches a zero value as the mode approaches its stability boundary. Nonetheless, the zero value is never reached. Instead, after the onset of instability, the damping remains almost constant at a very small value. This was expected due to the deficiency of the SSI-DATA in estimating the damping ratios as the system

approaches the stability boundary; that is, when the damping becomes much smaller, as previously discussed.

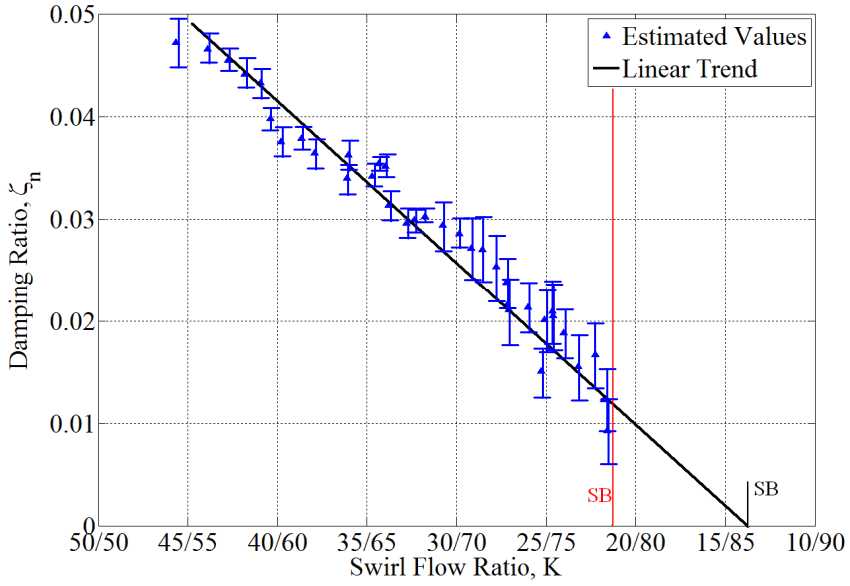


Figure 5.6: Dependence of the estimated damping ratio of the quarter wave longitudinal mode upon changes in control parameter *K*.

In spite of its limitations, the SSI-DATA method can be still applied to estimate the stability margin under stable operating conditions. Considering the plots in Figures 5.6 and 5.7, one can find a straight line $\tilde{\xi}_n = g(K)$ that represents the best fit of the data. Then, we evaluate the value of *K* for which $g(K)=0$. For the longitudinal mode case in Figure 5.6, the result of this procedure provided an approximated value of $K=14/86$, represented by the gray symbol SB. For the tangential mode case in Figure 5.7, we obtained an approximated value of $K=20/80$. That indicates the tangential mode tends to become unstable before the longitudinal mode, as confirmed by the experiment. The stability limit predicted by the tangential mode analysis is close to the actual operational

stability boundary ( $\approx 22/80$ ) indicated by the red line in the plots and the symbol SB in red. This means that the assessment of the operational stability margin or stability boundary by applying the SSI-DATA technique to the simplified linear model is much more accurate than the simple extrapolation of the dynamic pressure data.

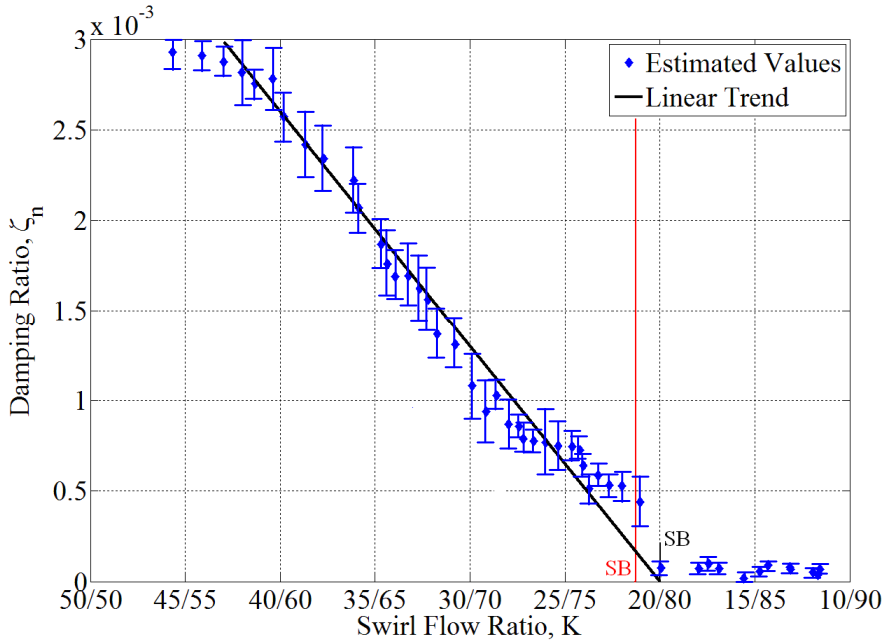


Figure 5.7: Dependence of the estimated damping ratio of the first tangential mode upon changes in control parameter *K*.

It seems that as the longitudinal mode was becoming more unstable (its damping ratio decreased), it provided more oscillatory energy to the system. At a certain operating condition, the system reached the critical amplitude in which the tangential mode was triggered. That could imply coupling between the longitudinal and tangential modes and will be investigated in the Chapter 6.

Besides the lack of accuracy of the SID-DATA technique as the system approaches the stability boundary, there is another reason for not relying on the estimates

under these conditions. As the system becomes less stable, the amplitude of the oscillations increases and nonlinear terms (in the mathematical model) become important before the system reaches the stability boundary. When this happens, the application of the model would be no longer valid.

Under unstable operational conditions the actual system has a negative linear damping ratio but nonlinearities will generate limit cycles. Linear model are not able to predict the amplitude of the limit cycles. Additionally, the multi-stable behavior presented in Figure 3.6 is evidence that the system has nonlinearities and feedback, so that a more accurate estimate of the operational stability margin must be based on nonlinear models. The results from the linear approximation (modal parameters) must be used as guidelines during the implementation of techniques for non-linear system identification.

# CHAPTER 6

# NON-LINEAR SYSTEM IDENTIFICATION

As discussed in Chapter 4, the main issue about non-linear behavior in combustion systems is related to the coupling between combustor acoustics and heat release dynamics. In this Chapter, an empirical nonlinear model for heat release dynamics will be identified from measured input-output data. Then, a system identification technique will be presented which can provide estimates of the parameters of the finite-dimensional dynamical model representing the whole combustor system.

## 6.1 Heat Release Dynamics Model

Deriving a complete, global, nonlinear dynamic model of the heat-release dynamics corresponding to the LRECS system is probably a subject for another thesis. In this work, we followed a common approach to derive (or identify) models for systems such as the flame dynamics where first-principles models can be too complex, and the structure of the system is very hard to model mathematically. A black-box modeling in time domain will be used. It consists of dynamic modeling using input-output data that describes the response of the overall heat release process.

The fundamental idea of input-output modeling is to construct a model from input output experimental data as shown in Figure 6.1. For the flame dynamics case, we are searching for a nonlinear dynamical model. In general, these models can be represented by nonlinear differential equations and state space realizations. For example, an $n^{th}$ order non-autonomous nonlinear model for heat release dynamics can be expressed in the following form:

$$\frac{d^n \dot{Q}'}{dt^n} = g(\dot{Q}', \frac{d\dot{Q}'}{dt}, \ldots, \frac{d^{n-1}\dot{Q}'}{dt^{n-1}}, p', \ldots, \frac{d^m p'}{dt^m}, \boldsymbol{\theta}) \tag{6.1}$$

where $\boldsymbol{\theta} \in \mathbb{R}^p$ is the vector of coefficients (parameters) for the linear and nonlinear terms and $g$ is a non-linear mapping.

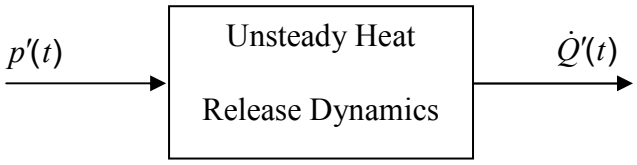


Figure 6.1: Input-output modeling of the heat release dynamics.

It is important to choose an appropriate structure for the model before applying an identification procedure. Experience shows that when the basic structure of the system is correct, it will not take too much time to fine tune the order of the system and search for a best fit to the data. For nonlinear systems, as we will discuss shortly, the form of nonlinearity and structure of the model are remarkably significant.

In some situations, the physics of the problem may unveil the nonlinearity of the system, or at least suggests the basic structure of the model. Under these circumstances, with known or assumed nonlinearities, parametric identification is applied to estimate all linear and nonlinear parameters using pseudo-linear regression, least squares, nonlinear instrumental variables, or prediction-error methods. That will be explained and implemented later in this work.

For a system with unknown nonlinearities, which may include several complex partial differential equations, nonparametric identification is more useful. It uses a functional expansion technique to approximate the unknown nonlinearities through a

nonlinear mapping. It maps the nonlinearity with a set of basis functions so that the coefficient of each basis function is subsequently estimated to find the model that best fits the data.

### 6.1.1 NARX modeling

Assuming that the heat release dynamics can be represented by Equation (6.1) the objective of the input-output black-box modeling is to determine the order of the system, $n$, the number of basis functions (also called regressors), $n+m-1$, and mainly the non-linear mapping, $g$. As the chemiluminescence and pressure data were collected as discrete time series, we represent the system as a Non-linear Autoregressive Model with Exogeneuos input (NARX) given by

$$\dot{Q}'(k) = g(\dot{Q}'(k-1), \dot{Q}'(k-2), \ldots, \dot{Q}'(k-n), p'(k-1), \ldots, p'(k-m-1), \bar{\boldsymbol{\theta}}) \qquad (6.2)$$

Without any a priori information about the system, the identification would be a very time consuming task. We would have to try several different orders and search for the non-linear mapping within families of functions. In this sense, the best approach is to perform some kind of semi-physical modeling, where some additional information about the system can be obtained from previously derived models. Such information can also be collected form preliminary analysis of the measured data, such as spectral and correlation analysis. Next, we present some previous analytical investigations about unsteady heat release dynamics which form the basis for the black-box modeling applied in this work.

In a combustor, the heat release can be perturbed either by flame area fluctuations, or by fluctuations in the mixture. The former can happen when the flame sheet is sensitive to fluctuations in the acoustic velocity ($u'$). These will force the flame to periodically oscillate, varying its total surface area. As the heat release is proportional

to the total surface area of the flame, fluctuations in the acoustic velocity affect the unsteady heat release[55]. The latter can happen either by fluctuations in mixture density, which is related to the acoustic pressure fluctuations ( $p'$ ) or when perturbations in the acoustic field affect the inlet conditions of one of the reactants (fuel or air), prior to mixing, which causes perturbations in the equivalence ratio and consequently perturbations in the unsteady heat release. This case could happen if the flow of one of the reactants into the combustor is not choked. However, the oscillations in the equivalence ratio can also be related to the oscillations in the acoustic velocity[56]. That implies the regressors related to the input should be assumed $p'(k-1)$ and $p'(k-2)$, which, as an approximation, correspond to oscillations in acoustic pressure and velocity, respectively.

The model order can also be estimated from previous analytical investigations. Some finite-dimension models for the flame dynamics in specific combustors have been proposed. Fleifil et al[55] derived the equations for the unsteady heat release dynamics based on the kinematics of the flame and modeled the variation in the flame surface area due to its interaction with an oscillating flow. The flame was represented by a thin sheet moving with a constant burning velocity in a normal direction to its surface relative to the reactants flow. After some manipulations, they obtained a first-order ordinary differential equation relating the unsteady rate of heat release and the velocity fluctuations at the flame location, $u'_f$ . A similar ODE was also derived by Dowling[57], following a different approach for a ducted flame stabilized at a flame holder. These models are described by the following ODE:

$$\frac{d\dot{Q}'}{dt} + b_1\dot{Q}' = b_2 u'_f \tag{6.3}$$

One can notice that in order to obtain a finite-dimensional model that does not include the time delay, a "new" variable, $u'_f$, was introduced. Following the work of Annaswamy et al[58] we can write the following expression for the new variable

$$u'_f(t) = \sum_{i=1}^{N_m} c_i\dot{\eta}_i(t) + \frac{(\gamma-1)}{\gamma\bar{p}}\chi\dot{Q}' \tag{6.3}$$

where $\chi$ represents the combined effects of the flow velocity fluctuations both behind and ahead of the flame. To make the frequency characteristics of the model compatible with the experimental evidence, Dowling[57] suggested a modification in Equation (6.3) and proposed a second-order model to the flame dynamics which can be expressed as

$$\frac{d^2\dot{Q}'}{dt^2} + b_1\frac{d\dot{Q}'}{dt} + b_2\dot{Q}' = b_3 u'_f \tag{6.4}$$

These results suggest that the model order, $n$, should be one or at most two, that is, the dynamics will be represented by a first or second-order differential equation. That defines the order and the set of regressors of the NARX model to be investigated. The fact that a differential equation should represent the heat release model indicates that the nonlinearity is not just a static nonlinearity that only exists at the input or output.

The last, and sometimes more complex task, is the selection of the non-linear mapping. Several models in literature have presented heat release models with cubic non-linearities in the acoustic velocity[59],[60]. A physical explanation for incorporating such non-linearities in the heat release dynamics model has been given as in the work of Rumsey et al[59]. They considered a heat release model given by the inclusion of a cubic non-linearity as

$$\frac{d\dot{Q}'}{dt} + b_1\dot{Q}' = b_2 u' - b_3 u'^3 \tag{6.5}$$

and justified the inclusion by the possibility of producing the 180º phase change observed experimentally and the resulting limit-cycle provided by numerical simulations of the complete finite-dimensional combustor model. Physically, the additional term could be related to changes in the flame kinematics, as suggested by Fleifil et al[60].

Fannin et al[61] proposed a similar model to represent the heat release dynamics; that is,

$$\frac{d\dot{Q}'}{dt} + b_1\dot{Q}' = b_2\dot{\eta} + b_3\dot{\eta}^2 + b_4\dot{\eta}^3 \tag{6.6}$$

In deriving this model the acoustic field was modeled as a single degree-of-freedom oscillator, while the heat release showed a first order relationship with acoustic velocity. In addition, cubic and quadratic nonlinearities have been added to the heat release equation to demonstrate nonlinear interactions. This selection was not based on physical reasoning. In fact, they used a previous result from input-output modeling of thermoacoustic instabilities presented by Fleifil et al[60].

Based on the information just presented, the input-output modeling performed in this work to identify a black-box model for the heat release dynamics in the LRECS was limited to the following set of regressors: $\dot{Q}'(k-1)$, $\dot{Q}'(k-2)$, $p'(k-1)$, $p'(k-2)$, and cubic non-linearities involving the regressors and their cross-terms (e.g, $p'(k-2)^2$, $p'(k-2)^3$, $\dot{Q}'(k-1)^3$, $p'(k-2)\dot{Q}'(k-1)^2$, etc.).

### 6.1.2 Model Identification

The data collected from the pressure transducers were processed to eliminate linear trends and set their means to zero. A bandpass filter was applied to the data from both pressure transducers and optical sensors to eliminate frequencies above 15 KHz and below 200Hz. They were divided into subsets with 2000 points so that for each value of the swirl flow ratio a minimum of 20 subsets could be obtained for each input (pressure) and output (chemiluminescence) signal. During each identification procedure, a subset of data from pressure and chemiluminescence was used for estimation and other subset used for validation purpose.

Since the objective was to detect the non-linearity, all the data used in this part of the investigation correspond to the unstable regime, where the amplitudes of the oscillations are large and non-linear behavior was most likely more pronounced. As an example, Figures 6.2a and 6.2b show the time-history of the data used as input and output in one of the identification runs. The different colors indicate the estimation and validation subsets. Figures 6.3a and 6.3b show the respective amplitude spectra.

The model identification was performed by using the System Identification Toolbox of MATLAB®. Several subsets were analyzed and some of the observations are presented below.

1) The data used in the identification procedure were collected in feedback loop. In this case, there is a tool in the non-linear system identification toolbox which can evaluate the presence of feedback. For all subsets, the presence of feedback was detected. The toolbox also has a utility which estimates the delay (as a number of samples) between input and output. At this point we should recall that some of the flame dynamics

models are based on the acoustic velocity taken at the flame location which corresponds to the acoustic velocity at the injectors' plate minus a convective time delay. Applying the delay to the input regressors usually improved the good fit of the data.

2) Performing system identification via Graphical User Interface of the System Identification toolbox in MATLAB® is much more intuitive and faster. However, the only response that we got on screen is the quality of the fit of the data and the estimated values of the coefficients of the basis functions (regressors) are not provided. These values give an indication of the importance of a certain regressor for the overall behavior of the model. In general, when we eliminated a regressor whose coefficient is negligibly small when compared to the others, the fit of the data decreased, whereas the computational time can be reduced considerably. Therefore, the identification was repeated with the best fit using the command line and the function "*nlarx*", so that the estimated parameters could be stored for analysis and application later in this chapter.

3) For most of the analysis, trying to fit directly the input and output data without any additional data processing led to poor results since the overall fit did not reach values above 46%. Nonetheless, a visible trend could be identified since the best results were obtained for a first order system, using $\dot{Q}'(k-1)$ as the output regressor, and using, $p'(k-2)$ and $p'(k-2)^3$ as the non-linear regressors.

4) The results were much better when we performed the identification after filtering the signals around their modal frequencies. For example, we bandpass filtered the input and output data around the modal frequency corresponding to the excited first tangential mode (largest peak in Figures 6.3a and 6.3b). Then, we applied the SID technique and the results indicated that a first-order system with a cubic and quadratic

non-linearity always provided the best fit (now around 75%). The results indicated the following model as the best fit

$$\frac{d\dot{Q}'_N}{dt} + b_1\dot{Q}'_N = b_2\dot{\eta}_N + b_3\dot{\eta}_N^2 + b_4\dot{\eta}_N^3 \tag{6.7}$$

where the subscript "*N*" in the heat release variable indicates that the identification was performed for an isolated mode.

5) The same procedure was also applied to some of the data corresponding to the stable regime. In this case, with smaller amplitudes of the oscillations we have assumed that the combustor would behave as a linear system in Chapter 5. The results of the identification procedure indicated that either a linear first-order model represented by

$$\frac{d\dot{Q}'_N}{dt} + b_1\dot{Q}'_N = b_2\dot{\eta} \tag{6.8}$$

or a first-order model given by Equation (6.7) provided the same level of fit for the data. Poor fits (around 50%) were obtained with both models.

The results from the model identification suggested that the low-order model represent by Equation (6.7) can represent the heat release dynamics in the LRECS for a single mode. It is identical to the model presented by Fannin et al[61]. Figure 6.4 shows the good agreement between the measured output (heat release) and the predicted response of the model given in Equation (6.7) for the first tangential mode. Applying this model to all data subsets and modes in the unstable regime provided good fits that varied from 68% to 80%.

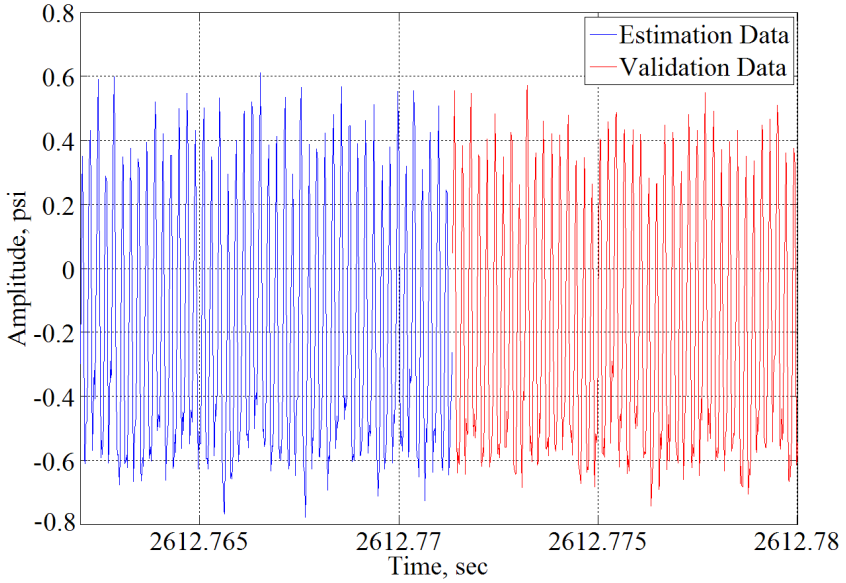


a)

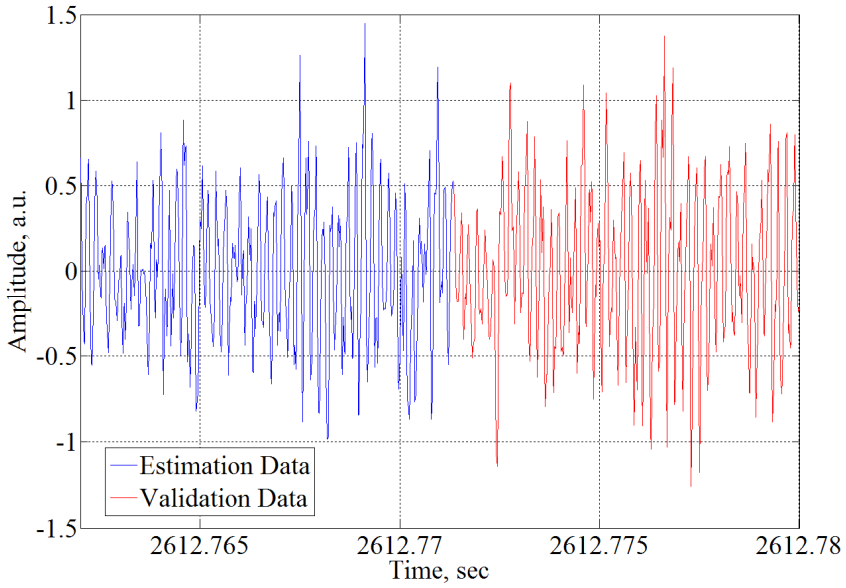


b)

Figure 6.2: Time history of: a) dynamic pressure oscillations; and b) heat release rate oscillations.

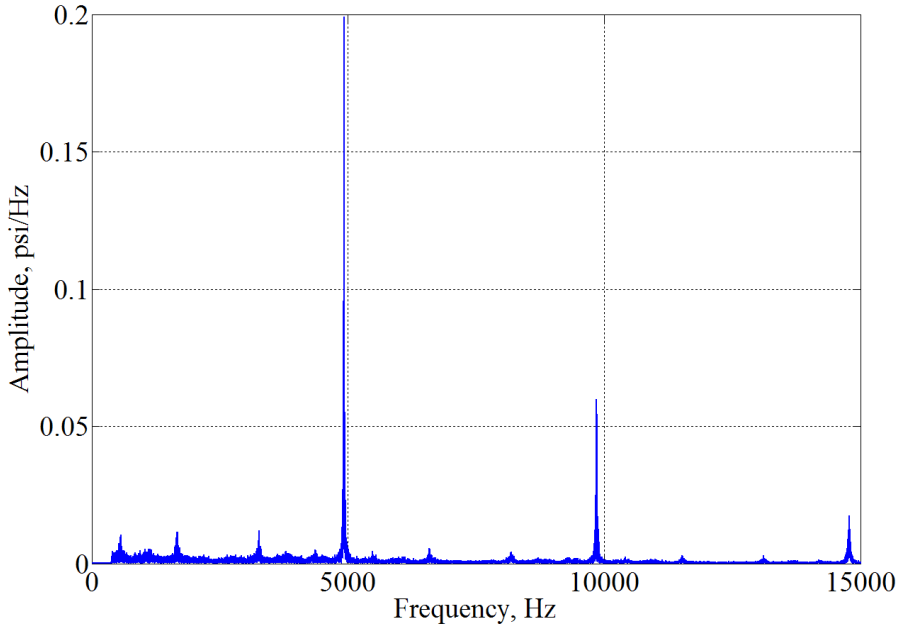


a)

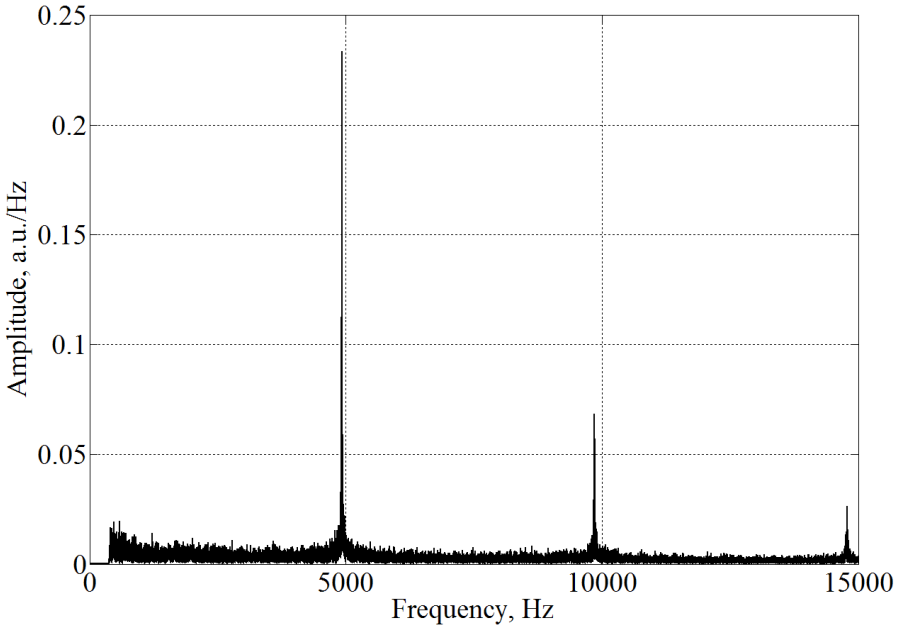


b)

Figure 6.3: Amplitude spectral density from sensors: a) $P_1'$; and b) $FOP_1'$, during unstable operation of the combustor ($\phi = 1; K = 16/84$)

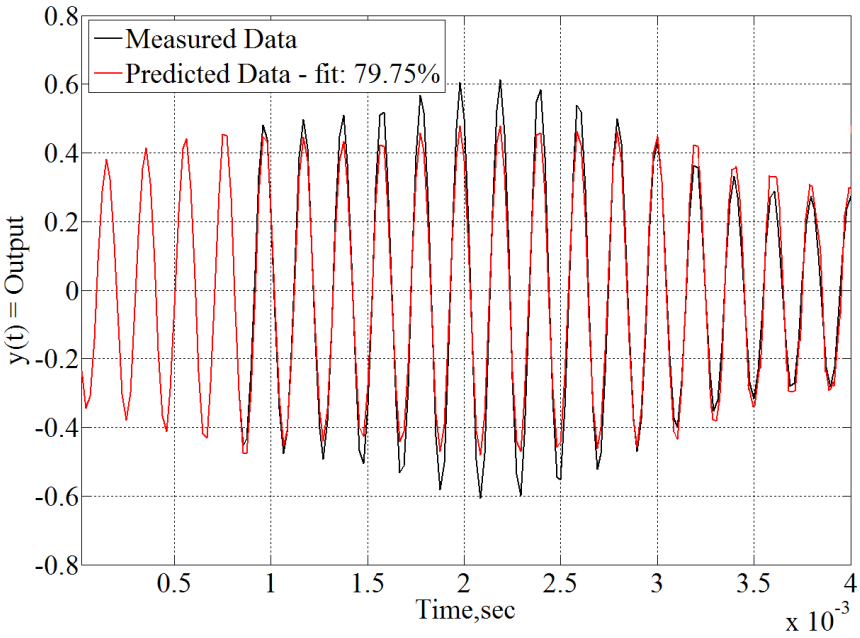


Figure 6.4: Comparison between the measured output and the predicted values given by the identified heat release model.

However, this unsteady heat release dynamic model for a single mode does not provide coupling between modes. Besides, such a model implies a large number of parameters to be estimated. Based on the results collected so far and the work of Rumsey et al.[59], we proposed the following model to describe the unsteady heat release dynamic in this thesis:

$$\frac{d\dot{Q}'_f}{dt} + b_1 \dot{Q}'_f = b_2 u_f + b_3 u_f^3 \tag{6.9}$$

where the subscript "$f$" denotes quantities evaluated at the flame location. The acoustic velocity at the flame location is calculated from Equation (4.38) as

$$u_f(t) = \mathbf{u}'(\mathbf{r}_f, t) = \sum_{m=1}^{\infty} \frac{\dot{\eta}_m(t)}{\gamma k_m^2} \nabla \psi_m(\mathbf{r}_f) \tag{6.10}$$

It is not expected that the model will mimic exactly the time history of the heat release oscillations collected by the optical sensors. So, the choice for this model was based on the performed input-output system identification, guided by information collected from previous analytical and experimental investigations.

At this point we should emphasize that writing the heat release model in the form of Equations (6.9) and (6.10) was a necessary condition for applying the SID technique that will be presented later in this chapter. We are presenting an analytically tractable model for the heat release dynamics for system identification purposes. However, one must recognize the limitations of the model by looking at the assumptions that need to be made for its application.

Rigorously, Equation (6.10) should be written as

$$u_f(t) = \mathbf{u}'(\mathbf{r}_f, t-\tau) = \sum_{m=1}^{\infty} \frac{\dot{\eta}_m(t-\tau_m)}{\gamma k_m^2} \nabla \psi_m(\mathbf{r}_f) \tag{6.11}$$

If we assume that the mode amplitudes are represented by

$$\begin{aligned} \eta_m(t) &= A_m \sin(\omega_m t + \varphi_m) \Rightarrow \\ \dot{\eta}_m(t) &= \omega_m A_m \cos(\omega_m t + \varphi_m) \end{aligned} \tag{6.12}$$

Then,

$$\dot{\eta}_m(t-\tau_m) = \omega_m A_m \cos(\omega_m t + \varphi_m - \omega_m \tau_m) \tag{6.13}$$

Therefore, Equation (6.10) assumes that the time-delays are small. This assumption is not supported by the evidence which shows that a necessary condition for thermoacoustic instabilities is that the combustion time (including the system delays) approximately equals the acoustic time. In this sense, the model in Equation (6.9) is in fact a first order non-linear fit to a real time-delayed system.

## 6.2 Non-linear Dynamical Model

The results discussed earlier in this thesis, indicates that the dynamics of the LRECS can be modeled by the following set of equations:

$$\ddot{\eta}_m + 2\alpha_m \dot{\eta}_m + \tilde{\omega}_m^2 \eta_m + \sum_{i=1}^{N_m}\sum_{j=1}^{N_m}(A_{mij}\dot{\eta}_i\dot{\eta}_j + B_{mij}\eta_i\eta_j) = a_m \frac{d\dot{Q}'_f}{dt} + \sigma_{0,N} W \quad m = 1,2,...,N_m \tag{6.14}$$

$$\frac{d\dot{Q}'_f}{dt} + b_1 \dot{Q}'_f = b_2 u_f + b_3 u_f^3 \tag{6.15}$$

$$u_f = \mathbf{u}'(\mathbf{r}_f, t) = \sum_{m=1}^{N_m} \frac{\dot{\eta}_m(t)}{\gamma k_m^2} \nabla \psi_m(\mathbf{r}_f) = \sum_{m=1}^{N_m} c_m \dot{\eta}_m(t) \tag{6.16}$$

$$p'_j(\mathbf{r}_j, t) = \overline{p} \sum_{m=1}^{N_m} \eta_m(t)\psi_m(\mathbf{r}_j) + e_j(t) = \sum_{m=1}^{N_m} d_{j,m}\eta_m(t) + e_j(t) \tag{6.17}$$

This model is composed of equations describing the combustor acoustics, the heat release dynamics and the coupling between them. The acoustics are described by a stochastically excited set of differential equations (SDEs) in the amplitude of the pressure fluctuations ($\eta_N$). The heat release is a source term in the equations of acoustics and its dynamics is described by a first-order non-linear ordinary differential equation relating the unsteady rate of heat release and the acoustic velocity fluctuations at the flame. The acoustic velocity fluctuations are related to the first derivative of the amplitude of the pressure fluctuations ($\dot{\eta}_N$). This completes the feedback in the system. The model indicates that the rate of heat release, $\dot{Q}'_N$, is also a state variable of the combustor system.

Following the approach presented in Chapter 4, one can represent the dynamical model of the LRECS in finite-dimension by modified versions of Equations (4.93) and (5.13) given by

$$d\mathbf{x}_t = \mathbf{f}(\mathbf{x}_t, \boldsymbol{\theta})dt + \boldsymbol{\sigma}\mathbf{dW}_t \tag{6.18}$$

$$\mathbf{y}_k = \mathbf{h}(\mathbf{x}_k, \boldsymbol{\theta}) + \mathbf{e}_k \tag{6.19}$$

where $\mathbf{h} \in \mathbb{R}^{L \times 2N_m}$ is called the observation function matrix. The subscript "*k*" in Equation (6.19) accounts for the discrete-time characteristic of the measured data.

## 6.3 System Identification Technique

The SID technique implemented to estimate the parameters, $\boldsymbol{\theta}$, of the dynamical model given by Equations (6.18) and (6.19) is based on Predictor Error Method (or maximum likelihood estimation). It can be considered a modified version of the non-linear gray-box model identification tool currently available in the *System Identification Toolbox* of MATLAB®®. The main difference is the use of an iterative extended Kalman filter (EKF). An overview of the method will be provided, but more details can be found in the book of Ljung[20].

### 6.3.1 Maximum Likelihood Estimation

Given the model structure, *maximum likelihood* (ML) estimation of the unknown parameters is performed by finding the parameters that maximize the likelihood function of a given sequence of measurements $\mathbf{y}_0, \mathbf{y}_1, \ldots, \mathbf{y}_k, \ldots, \mathbf{y}_N$. By introducing the notation:

$$\mathbf{Y}_k = [\mathbf{y}_k, \mathbf{y}_{k-1}, \ldots, \mathbf{y}_1, \mathbf{y}_0] \tag{6.20}$$

the likelihood function is the joint probability density[62]:

$$L(\boldsymbol{\theta}; \mathbf{Y}_N) = p(\mathbf{Y}_N | \boldsymbol{\theta}) = \left( \prod_{k=1}^{N} p(\mathbf{y}_k | \mathbf{Y}_{k-1}, \boldsymbol{\theta}) \right) p(\mathbf{y}_0 | \boldsymbol{\theta}) \tag{6.21}$$

where the rule $p(A|B) = p(A \cap B) / p(B)$ has been applied to form a product of conditional probability densities. In order to obtain an exact evaluation of the likelihood

function, the initial probability density $p(\mathbf{y_0}|\boldsymbol{\theta})$ must be known and all subsequent conditional densities must be determined by successively solving Kolmogorov's forward equation and applying Bayes' rule[62]. As a matter of fact, this approach would not be computationally feasible in practice. However, since the diffusion terms in the above model structures do not depend on the state variables (no parametric noise), a simpler alternative can be used. Specifically, an approximate method based on Extended Kalman Filter (EKF) was applied.

The latter approximation can be applied, because the stochastic differential equations considered are driven by Wiener processes and because increments of a Wiener process are Gaussian, which makes it reasonable to assume, under some regularity conditions, that the conditional densities can be well approximated by Gaussian densities. The Gaussian density is completely characterized by its mean and covariance. Thus, by introducing the notation:

$$\hat{\mathbf{y}}_{\mathbf{k|k\text{-}1}} = E[\mathbf{y}_\mathbf{k}|\,\mathbf{Y}_{\mathbf{k-1}},\boldsymbol{\theta}] \tag{6.22}$$

$$\mathbf{R}_{\mathbf{k|k-1}} = V[\mathbf{y}_\mathbf{k}|\,\mathbf{Y}_{\mathbf{k-1}},\boldsymbol{\theta}] \tag{6.23}$$

$$\boldsymbol{\varepsilon}_\mathbf{k} = \mathbf{y}_\mathbf{k} - \ddot{\mathbf{y}}_{\mathbf{k|k\text{-}1}} \tag{6.24}$$

where $\boldsymbol{\varepsilon}_\mathbf{k}$ is the predictor error, $\ddot{\mathbf{y}}_{\mathbf{k|k\text{-}1}}$ is the estimated value in function of the previous state vector, and $\mathbf{R}_{\mathbf{k|k-1}}$ is the matrix of covariances, the likelihood function is given by

$$L(\boldsymbol{\theta};\mathbf{Y_N}) == \left( \prod_{k=1}^{N} \frac{\exp(-\frac{1}{2}\boldsymbol{\varepsilon}_\mathbf{k}^\mathrm{T}\mathbf{R}_{\mathbf{k|k-1}}^{-1}\boldsymbol{\varepsilon}_\mathbf{k})}{\sqrt{\det(\mathbf{R}_{\mathbf{k|k-1}})(\sqrt{2\pi})^l}} \right) p(\mathbf{y_0}\,|\,\boldsymbol{\theta}) \tag{6.25}$$

where, for given parameters and initial states, $\boldsymbol{\varepsilon}_\mathbf{k}$ and $\mathbf{R}_{\mathbf{k|k-1}}$ can be computed by means of an extended Kalman filter as shown in the next section.

Conditioning on $\mathbf{y_0}$ and taking the negative logarithm in Eq. (6.25) provides

$$-\ln(L(\boldsymbol{\theta};\mathbf{Y_N} \mid \mathbf{y_0})) == \frac{1}{2}\sum_{k=1}^{N}\left(\ln(\det(\mathbf{R_{k|k-1}}) + \boldsymbol{\varepsilon}_\mathbf{k}^{\mathbf{T}}\mathbf{R}_{\mathbf{k|k-1}}^{-1}\boldsymbol{\varepsilon}_\mathbf{k}\right) + \frac{1}{2}\left(\sum_{k=1}^{N} l\right)\ln(2\pi) \quad (6.26)$$

The maximum likelihood of the parameters can now be determined by solving the following non-linear optimization problem

$$\hat{\boldsymbol{\theta}} = \arg\min\{-\ln(L(\boldsymbol{\theta};\mathbf{Y_N} \mid y_0))\} \quad (6.27)$$

### 6.3.2 Extended Kalman Filter

The Kalman filter is a recursive predictive filter that is based on the use of state space techniques and recursive algorithms. It estimates the state of a dynamical system, based on two steps: the prediction and the correction. In the first step the state is predicted via the *dynamic model*, and corrected via the *observation model* in the second step. It is an optimal estimator since the error covariance of the estimator is minimized. It is also a recursive filter as the procedure is repeated for each time step using the state of the previous time step as an initial value.

The basic components of the Kalman filter are the state vector, given by $\mathbf{x_t}$ in Equation (6.18), and the dynamical and observation models. The state vector was already defined and contains the state variables of interest. In general, these variables cannot be measured directly and their values are inferred from the measured ones. In applying the Kalman filter, we define the *a priori* value ($\hat{\mathbf{x}}_{\mathbf{k|k-1}}$) of the state vector which is the predicted value before the update, and the *a posteriori* value ($\hat{\mathbf{x}}_{\mathbf{k|k}}$) which is the corrected value after the update.

The dynamic model simply describes the changes of the state vector with time. It is usually represented by a system of differential equations in matrix form. In this work, the dynamic model is given by Equation (6.18). The observation model represents the relationship between the state and the measured data and it is given by Equation (6.19).

When either the dynamic or the observation model is non-linear, the application of the standard Kalman filter is computationally very time consuming and usually leads to "false" minimum in the optimization procedure. One approach for resolving such non-linear problems is to use the Extended Kalman filter (EKF).

We assume that the initial parameters and state vector are known and the following steps are used to calculate $\boldsymbol{\varepsilon}_{\mathbf{k}}$ and $\mathbf{R}_{\mathbf{k|k-1}}$. First, using the initial state vector we evaluate the predictions equations as

$$\ddot{\mathbf{y}}_{\mathbf{k|k-1}} = \mathbf{h}(\ddot{\mathbf{x}}_{\mathbf{k|k-1}}, \boldsymbol{\theta}) \tag{6.28}$$

$$\mathbf{R}_{\mathbf{k|k-1}} = \mathbf{H}.\mathbf{P}_{\mathbf{k|k-1}}.\mathbf{H}^{T} \tag{6.29}$$

where $\mathbf{H} = \left.\frac{\partial h}{\partial \mathbf{x}_{\mathbf{t}}}\right|_{\mathbf{x}_{\mathbf{t}}=\hat{\mathbf{x}}_{\mathbf{k|k-1}}, t=t_k, \boldsymbol{\theta}}$ is called the observation matrix and $\mathbf{P}_{\mathbf{k|k-1}}$ is the covariance matrix of the state vector $\ddot{\mathbf{x}}_{\mathbf{k|k-1}}$.

Then, the prediction error is calculated by the innovation equation

$$\boldsymbol{\varepsilon}_{\mathbf{k}} = \mathbf{y}_{\mathbf{k}} - \ddot{\mathbf{y}}_{\mathbf{k|k-1}} \tag{6.30}$$

And the Kalman gain is calculated by

$$\mathbf{K}_{\mathbf{k}} = \mathbf{P}_{\mathbf{k|k-1}}.\mathbf{H}^{T}.\mathbf{R}^{-1}_{\mathbf{k|k-1}} \tag{6.31}$$

One can then calculate the a posteriori state vector and corresponding covariance matrix at time "*k*" as a function of the present time "*k*" by the following updating equations.

$$\ddot{\mathbf{x}}_{\mathbf{k|k}} = \ddot{\mathbf{x}}_{\mathbf{k|k-1}} + \mathbf{K}_{\mathbf{k}}\boldsymbol{\varepsilon}_{\mathbf{k}} \tag{6.32}$$

$$\mathbf{P}_{\mathbf{k|k}} = \mathbf{P}_{\mathbf{k|k\text{-}1}} - \mathbf{K}_{\mathbf{k}}\mathbf{R}_{\mathbf{k|k\text{-}1}}.\mathbf{K}_{\mathbf{k}}^{\mathbf{-1}} \tag{6.33}$$

Finally, we solve the following state predictions equations to calculate $\ddot{\mathbf{x}}_{\mathbf{k+1|k}}$ and $\mathbf{P}_{\mathbf{k+1|k}}$, which will be substituted into Equations (6.28) and (6.29) to repeat the procedure. In this way, we can estimate the prediction error and the covariance matrix at all discrete time instants.

$$\frac{d\ddot{\mathbf{x}}_{\mathbf{t|k}}}{dt} = \mathbf{f}(\hat{\mathbf{x}}_{\mathbf{t|k}}, t, \boldsymbol{\theta}),\ t \in [t_k, t_{k+1}) \tag{6.34}$$

$$\frac{d\mathbf{P}_{\mathbf{t|k}}}{dt} = \mathbf{F}.\mathbf{P}_{\mathbf{t|k}} + \mathbf{P}_{\mathbf{t|k}}.\mathbf{F}^T + \boldsymbol{\sigma}.\boldsymbol{\sigma}^T,\ t \in [t_k, t_{k+1}) \tag{6.35}$$

## 6.4 System Identification Accuracy

Using the methodology presented in Chapter 4, we simulated the response of the following system of coupled Van der Pol random oscillators

$$\begin{aligned} \ddot{\eta}_1 &= -\tilde{\omega}_1^2\eta_1 + \varepsilon_1(Q - QP^2) + \Xi(t) \\ \ddot{\eta}_2 &= -\tilde{\omega}_2^2\eta_2 + \varepsilon_2(Q - QP^2) + \Xi(t) \\ y &= P + e(t) \end{aligned} \tag{6.36}$$

where $Q = \dot{\eta}_1 + \dot{\eta}_2$ and $P = \eta_1 + \eta_2$. These equations can be written in the form of Equations (6.18) and (6.19) by defining

$$\mathbf{x}_{\mathbf{t}} = [x_1 \quad x_2 \quad x_3 \quad x_4]^T \tag{6.37}$$

where $x_1 = \eta_1$, $x_2 = \eta_2$, $x_3 = \dot{\eta}_1$, and $x_4 = \dot{\eta}_2$. Thus, we have

$$\mathbf{f}_1(\mathbf{x_t},\boldsymbol{\theta})=\begin{bmatrix} x_3 \\ x_4 \\ -\tilde{\omega}_1^2 x_1+\varepsilon_1(x_3+x_4)-\varepsilon_1(x_3+x_4)(x_1^2+2x_1x_2+x_2^2) \\ -\tilde{\omega}_2^2 x_1+\varepsilon_2(x_3+x_4)-\varepsilon_2(x_3+x_4)(x_1^2+2x_1x_2+x_2^2) \end{bmatrix} \tag{6.38}$$

$$\boldsymbol{\sigma}\mathbf{dW_t}=\begin{bmatrix} 0 & 0 & 0 & 0 \\ 0 & 0 & 0 & 0 \\ 0 & 0 & \sigma_\Xi^2 & 0 \\ 0 & 0 & 0 & \sigma_\Xi^2 \end{bmatrix}\mathbf{dW_t} \tag{6.39}$$

$$\mathbf{h}(\mathbf{x_k},\boldsymbol{\theta})=x_1+x_2 \tag{6.40}$$

and $\boldsymbol{\theta}=[\tilde{\omega}_1 \quad \tilde{\omega}_2 \quad \varepsilon_1 \quad \varepsilon_2]$.

A similar system without stochastic excitation has been proposed by Bouziani et al[63] as a model for combustion instabilities. The actual parameters and their estimated values are shown in the Table 6.1. A total of 48,000 samples were collected at sampling frequency of 48 KHz and divided into 10 sets of 4800 data points for estimation.

Table 6.1: Comparison between actual and estimated values of the system parameters.

| System Parameter | Actual Value | Estimated Value | Error (%) |
|---|---|---|---|
| $\tilde{f}_1$ | 600 | 619.8 | 3.30 |
| $\tilde{f}_2$ | 5000 | 5244.5 | 4.89 |
| $\varepsilon_1$ | 15 | 12.9 | 14.0 |
| $\varepsilon_2$ | 40 | 45.4 | 13.5 |
| $\sigma_\Xi^2$ | 400 | 350.4 | 12.4 |
| $\sigma_e^2$ | 0.005 | 0.0054 | 8.0 |

Figure 6.5a presents an example of the simulated and estimated response (time history) for this system. The identified model captures very well the qualitative behavior of the system. Figure 6.5b shows that the amplitude spectral density is also in very good agreement.

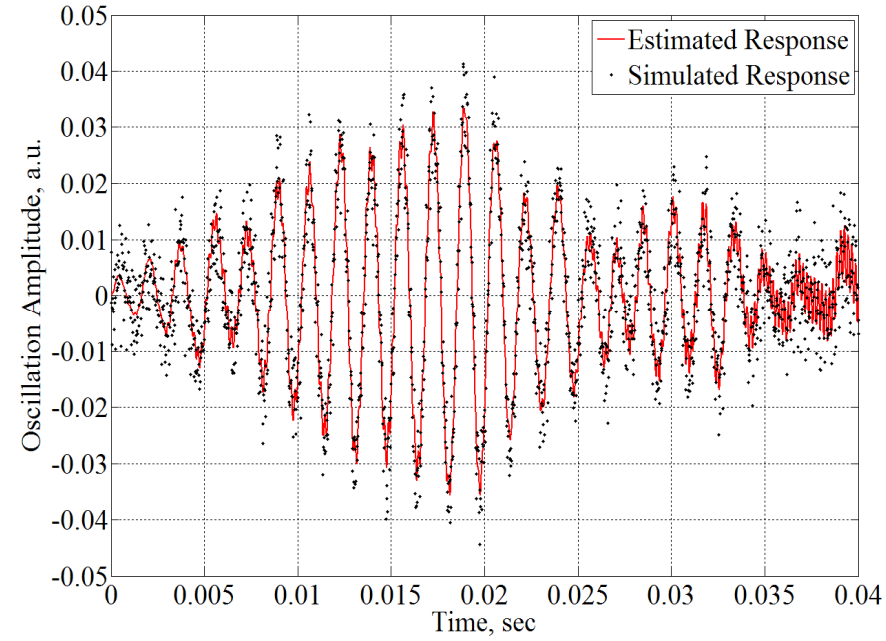


a)

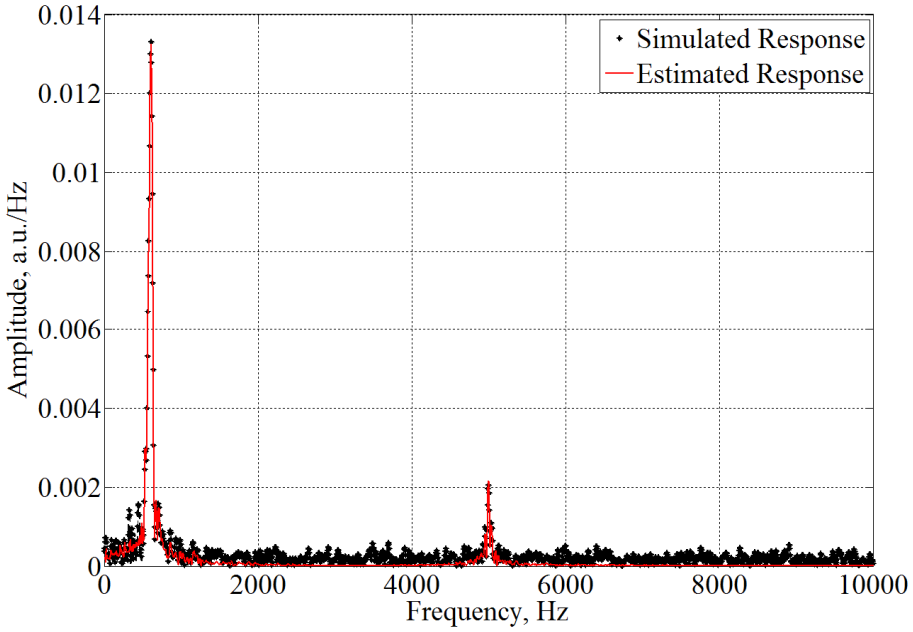


b)

Figure 6.5: System response: a) time history; and b) amplitude spectral density.

However, two important issues needed to be addressed to obtain this good agreement. The first one involves the number of data points used in the estimation. Since the experimental data was collected at sampling frequency of 48 KHz, all numerical simulations were performed at that rate. The results indicated that accurate estimates for non-linear systems can be expected for modes with frequencies up to 10 KHz using sets of at least 4000 data points. Compared to the SSI-DATA technique, the PEM requires much more samples (longer duration of experiments) for good accuracy.

The second issue concerns the evaluation of the initial conditional probability density, which is necessary to start the iterative procedure. This means that it is necessary to provide initial values (guessed) for the model parameters as well as range of values over which the optimization algorithm will search for their correct values. Depending on these initial values and ranges, the algorithm can take a long time to find the answer. There is also a chance that the algorithm might find a local minimum that does not represent the sought solution or become unstable (convergence problems).

## 6.5 Experimental Results

The technique was applied to the experimental data discussed in Chapter 3. Only the dynamic pressure data was used in the identification procedure as the output, characterizing a stochastic identification. In order to obtain estimates as accurate as possible, the data corresponding to a given value of the control parameter (swirl flow ratio) was divided into 10 subsets with 4800 points each. This represents a total of one second of data at the experimental sampling rate.

### 6.5.1 Analysis of Initial Values for Parameters

The model represented by Equations (6.11-6.14) includes a large number of parameters. Consequently, convergence problems in the numerical algorithm applied to estimate those parameters are very likely, unless very good initial values can be provided. To resolve such a problem, a stepwise approach was applied. In this sense, we initially performed the identification of the linear system as explained in Chapter 5. From the preliminary linear analysis the modal effective angular frequencies were found and set as fixed parameters in the non-linear identification. The estimated values of the modal effective damping ratios in the linear identification were used as initial guesses in the non-linear identification and their range set to the interval [-0.1,0.1]. Therefore, the parameters corresponding to the linear part of the model were addressed by the preliminary linear identification.

Since the non-linear parameters are suppose to be responsible for the particular behavior of the system (bifurcation and hysteresis), the non-linear part of the model requires more attention. The non-linear parameters in the model were divided into physical and non-physical parameters. As the name indicates physical parameters are the result of a physically-based modeling and, in principle, they can be expressed as functions of the system properties. So, their initial values and range to be given as input to the identification algorithm can be calculated from those functions. In the other hand, the initial values of the non-physical parameters cannot be calculated and should be estimated via a preliminary black-box modeling.

Once more we emphasize the importance of the physical parameters. During the identification procedure they will be estimated along with the non-physical parameters.

However, the possibility of having a good initial guess for their values based on the expressions relating them to system properties is very helpful. We start our analysis with Equation (6.11). The physical parameters $A_{mij}$ and $B_{mij}$, obtained from the non-linear coupling terms due to gasdynamics (up to second order) are given by

$$A_{mij} = \frac{I_{mij}}{4\gamma E_m^2 k_i^2 k_j^2}[(k_i^2 + k_j^2) - k_m^4 - 4\gamma k_i^2 k_j^2] \tag{6.41}$$

$$B_{mij} = \frac{I_{mij}\overline{a}^2}{2\gamma E_m^2}(\gamma - 1)(k_i^2 + k_j^2) \tag{6.42}$$

where $I_{mij} = \int_0^L \int_0^{2\pi} \int_0^R \psi_m \psi_i \psi_j r dr d\theta dx$, and $E_m^2 = \int_0^L \int_0^{2\pi} \int_0^R \psi_m^2 r dr d\theta dx$,.

Equations (6.41) and (6.42) indicate that $A_{mij}$ and $B_{mij}$ can be calculated based on the geometry of the combustor, boundary conditions of the problem, and thermodynamic properties of the products of combustion. The geometry and boundary conditions will determine the mode shapes given by

$$\psi_i(\mathbf{r}) = \psi_{pmn}(x, r, \theta) = \cos(k_p x)\cos(m\theta)J_m(\kappa_{mn} r) \tag{6.43}$$

while the thermodynamic data (i.e., $\gamma$ and $\overline{a}$) can be found in the Table 3.2. Since the modal frequencies were shown in Table 3.3, the wave numbers can be directly obtained by $k_i = \tilde{\omega}_i / \overline{a}$. Therefore, if one assumes the effect of changes in swirl flow ratio upon the mean properties of the mixture (i.e., density, temperature, etc.) are negligible, those parameters will be constant. Consequently, we should expect that $A_{mij} \neq A_{mij}(K)$ and $B_{mij} \neq B_{mij}(K)$.

For coupling between longitudinal modes those parameters can be calculated analytically. When transverse modes are taken into account the calculations should be

carried out numerically. These calculations involve triple integrals which can be simplified if one realizes that the expression for the mode shapes can be written in the form of separable functions as

$$\psi_i(\mathbf{r}) = \psi_{pmn}(x,r,\theta) = \cos(k_p x)\cos(m\theta)J_m(\kappa_{mn} r) = \mathrm{X}(x).\Theta(\theta).R(r) \qquad (6.44)$$

Table 6.2 shows the values of $A_{mij}$ and $B_{mij}$ considering just the first longitudinal and first tangential modes excited. The corresponding mode shapes are

$$\psi_{1L}(\mathbf{r}) = \psi_{100}(x,r,\theta) = \cos(k_p x) \qquad (6.45)$$

$$\psi_{1T}(\mathbf{r}) = \psi_{010}(x,r,\theta) = \cos(\theta)J_1(\kappa_{10} r) \qquad (6.46)$$

where $k_{1L} = \omega_{1L} / \bar{a}$, $\kappa_{10} = 1.8452 / R$ and $R$ is the radius of the combustor.

Table 6.2: Theoretical values of the parameters $A_{mij}$ and $B_{mij}$ for coupling between first longitudinal and first tangential modes ($\gamma = 1.168$ and $\bar{a} = 893.2 m/s$).

| $A_{mij}$ ($m$=1L) | | $i$ | |
|---|---|---|---|
| | | 1L | 1T |
| $j$ | 1L | -1.0129 | 0 |
| | 1T | 0 | -0.1494 |
| $A_{mij}$ ($m$=1T) | | $i$ | |
| | | 1L | 1T |
| $j$ | 1L | 0 | -11.3278 |
| | 1T | -11.3278 | 0 |
| $B_{mij}$ ($m$=1L) | | $i$ | |
| | | 1L | 1T |
| $j$ | 1L | 1.74E6 | -1.4646 |
| | 1T | -1.4646 | 2.12E7 |
| $B_{mij}$ ($m$=1T) | | $i$ | |
| | | 1L | 1T |
| $j$ | 1L | -0.1988 | 5.14E7 |
| | 1T | 5.14E7 | 173.7638 |

Next, the parameter related to the source term due to unsteady heat release, $a_m$, is analyzed. Equation (4.80) introduced the following definition

$$\frac{\gamma-1}{\bar{p}E_m^2}\iiint_V \psi_m \frac{\partial \dot{Q}'}{\partial t} dV = a_m \frac{\partial \dot{Q}'_f}{\partial t} \tag{6.47}$$

Here we need to be careful, since we have assumed that the heat release is uniformly distributed in a certain region of the combustor near the injector plate. Thus, we can write the heat release as

$$\dot{Q}'(\mathbf{r},t) = \dot{Q}'_f(t)\delta(\mathbf{r}-\mathbf{r}_f) \tag{6.48}$$

where $\mathbf{r}_f$ represents the coordinates of the flame in space. Substituting Equation (6.48) into (6.47) one obtains

$$a_m = \frac{\gamma-1}{\bar{p}E_m^2}\psi_m(\mathbf{r}_f) \tag{6.49}$$

For the longitudinal mode the calculation is straightforward, as shown in Equation (4.80) and repeated below.

$$a_{1L} = \frac{\gamma-1}{\bar{p}E_{1L}^2} A_{ch}\cos(k_{1L}x_f) \tag{6.50}$$

However, for a transverse mode this calculation provides no unique values, since the flame is spatially distributed. This means that $r_f$ and $\theta_f$ are not defined. Since all parameters will be estimated the initial value of the unsteady heat release parameter for the first tangential mode was set equal to the longitudinal mode. Thus, substituting the values given in Table 6.3 into Equation (6.50) one obtains

$$a_{1L} = a_{1T} = 8.75E-5 \tag{6.51}$$

Next, we consider Equation (6.12). The only physical parameter is $b_1$ which can be written as[59]

$$b_1 = 2S_u / R \tag{6.52}$$

where $S_u$ is the burning speed. Fleifil et al[58] have proposed to write the Equation (6.12) as

$$\frac{d\dot{Q}'_f}{dt} + b_1 \dot{Q}'_f = b_4 f(u_f) \tag{6.53}$$

where $f(u_f) = b_2 u_f + b_3 u_f^3$, and the new parameter, $b_4$, is a physical parameter which can be expressed by

$$b_4 = 2S_u \rho_u \Delta q_r / R \tag{6.54}$$

where $\rho_u$ is the density of the reactants and $\Delta q_r$ is the heat release rate per unit mass.

Table 6.3: Thermodynamical and kinematic flow properties and combustor geometry data.

| | | | |
|---|---|---|---|
| Average speed of sound | $\overline{a}$ = | 893.2 | m/sec |
| Combustor Length | $L$ = | 0.325 | m |
| Combustor Radius | $R$ = | 0.052 | m |
| Gama | $\gamma$ = | 1.168 | |
| Mean Pressure | $\overline{p}$ = | 10332.27 | Kg/m$^2$ |
| Axial position of the pressure sensor #1 | $x_{P'_1}$ = | 0 | m |
| Radial position of the pressure sensor #1 | $r_{P'_1}$ = | 0.046 | m |
| Azimuthal position of the pressure sensor #1 | $\theta_{P'_1}$ = | 0 | rad |
| Axial position of the pressure sensor #2 | $x_{P'_2}$ = | 0 | m |
| Radial position of the pressure sensor #2 | $r_{P'_2}$ = | 0.046 | m |
| Azimuthal position of the pressure sensor #2 | $\theta_{P'_2}$ = | 3.14159 | rad |
| Axial position of the optical sensor | $x_f$ = | 0.015 | m |
| Burning speed | $S_u$ = | 0.5 | m/sec |
| Reactants Density | $\rho_u$ = | 0.12 | kg/m$^3$ |
| Heat release rate / unit mass mixture | $\Delta q_r$ = | 4.30E+07 | J/kg |

Therefore, we should consider the values of $b_1$ and $b_4$ when introducing the parameters initial guessed values. The parameters $b_2$ and $b_3$ are non-physical and their initial values were set equal to unity. Besides, the investigation performed by Rumsey et al[59] has shown that $b_2$ and $b_3$ should be small values (between 0 and 10).

In Equation (6.13), the physical parameters are the $c_m$'s. Their values are calculated based on the flame location, so that we have the same issue as for the values of $a_m$. We calculated the value of $c_m$ for the longitudinal mode and we used that value as the initial guess for the value of $c_m$ for the first tangential mode. Thus, we have

$$c_{1T} = c_{1L} = \frac{\sin(k_{1L} x_f)}{\gamma k_{1L}} = 0.0128 \tag{6.55}$$

Finally, in Equation (6.14) the physical parameters are the $d_{j,m}$'s which are fixed; that is, they are not estimated by the SID technique. Their values are calculated based on the location of the pressure transducers (i.e., $d_{j,m} = \psi_m(\mathbf{r}_j)$) whose coordinates are shown in Table 6.3. After substituting the values into the equation we have

$$\begin{aligned} d_{1,1L} &= d_{2,1L} = 1 \\ d_{1,1T} &= 0.5726 \\ d_{2,1T} &= -0.5726 \end{aligned} \tag{6.56}$$

### 6.5.2 Model for Identification

Applying the "rule of thumb" in system identification ("try simple first"), we limited the degrees-of-freedom of the model to the first longitudinal and first tangential modes. The reason for that comes from the preliminary analysis of the experimental data which indicated that these two modes might play important roles on the onset and decay of instability.

The dynamical model with the mentioned modes can be written in the form of Equations (6.18) and (6.19) by defining

$$\mathbf{x_t} = [\, x_1 \quad x_2 \quad x_3 \quad x_4 \quad x_5 \,]^T \tag{6.57}$$

where $x_1 = \eta_{1L}$, $x_2 = \eta_{1T}$, $x_3 = \dot{\eta}_{1L}$, $x_4 = \dot{\eta}_{1T}$, and $x_5 = \dot{Q}'_f$. Thus, we have

$$\mathbf{f(x_t, \theta)} = \begin{bmatrix} x_3 \\ x_4 \\ \{-\tilde{\omega}_{1L}^2 x_1 - 2\alpha_{1L} x_3 - A_{1L1L1L} x_3^2 - B_{1L1L1L} x_1^2 - A_{1L1T1T} x_4^2 - B_{1L1T1T} x_2^2 \\ -2A_{1L1L1T} x_3 x_4 - 2B_{1L1L1T} x_1 x_2 + a_{1L}[-b_1 x_5 + b_4 b_2 (c_{1L} x_3 + c_{1T} x_4) + b_4 b_3 (c_{1L} x_3 + c_{1T} x_4)^3]\} \\ \{-\tilde{\omega}_{1T}^2 x_2 - 2\alpha_{1T} x_4 - A_{1T1L1L} x_3^2 - B_{1T1L1L} x_1^2 - A_{1T1T1T} x_4^2 - B_{1T1T1T} x_2^2 \\ -2A_{1T1L1T} x_3 x_4 - 2B_{1T1L1T} x_1 x_2 + a_{1T}[-b_1 x_5 + b_4 b_2 (c_{1L} x_3 + c_{1T} x_4) + b_4 b_3 (c_{1L} x_3 + c_{1T} x_4)^3]\} \\ -b_1 x_5 + b_4 b_2 (c_{1L} x_3 + c_{1T} x_4) + b_4 b_3 (c_{1L} x_3 + c_{1T} x_4)^3 \end{bmatrix} \tag{6.58}$$

$$\boldsymbol{\sigma} \mathbf{dW_t} = \begin{bmatrix} 0 & 0 & 0 & 0 & 0 \\ 0 & 0 & \ddots & \ddots & 0 \\ 0 & \ddots & \sigma_{\Xi,1L}^2 & \ddots & 0 \\ 0 & \ddots & \ddots & \sigma_{\Xi,1T}^2 & 0 \\ 0 & 0 & 0 & 0 & 0 \end{bmatrix} \mathbf{dW_t} \tag{6.59}$$

$$\mathbf{h(x_k, \theta)} = \begin{bmatrix} d_{1,1L} x_1 + d_{1,1T} x_2 \\ d_{2,1L} x_1 + d_{2,1T} x_2 \end{bmatrix} \tag{6.60}$$

### 6.5.3 Model Parameters Estimation

The dynamical system identification was preformed using a developed MATLAB® code for stochastic non-linear model parameter estimation. As mentioned before, the number of parameters to be estimated is very large. As a consequence, every time we tried to estimate all physical and non-physical parameters at once based on the estimates from linear approximation a convergence problem occurred. To resolve this issue we decided that only the non-physical parameters should be estimated first, which sensibly decreased the number of parameters for estimation.

Thus, in a first run, all physical parameters were set as fixed and the non-physical parameters were estimated along with the damping ratios and noise variances. Next, a new estimation was performed using the just estimated values of the mentioned parameters as their initial values and all parameters were set to be estimated by the SID algorithm, except for $b_4$ which was held fixed (in order to estimate $b_2$ and $b_3$).

Figures (6.6a) to (6.6l) show the dependence of the estimated values of the model parameters due to non-linear coupling by gasdynamics ($A_{mij}$ and $B_{mij}$) upon changes in the swirl flow ratio. In all plots the blue lines represent the initial (guessed) values of the parameters, and the dashed lines (black and red) represents the best fit (polynomial fit) of the data. The vertical lines represent the standard deviation for each estimated value. Due to the scattering in the estimates, there are no clear trends in the results of the best fit. Thus, we consider these parameters independent on *K*.

Figures (6.7a) and (6.7b) show the dependence of the estimated values of the modal frequencies upon changes in the swirl flow ratio. The results indicate that the estimated values of the modal frequencies remain practically constant upon changes in the control parameter *K*. One can note a small scattering in the estimated values in the range of control parameter in which the mode contribution for the total signal is smaller. In this sense, the estimated value of the longitudinal mode frequency is scattered after the onset of tangential instability and vice-versa. One should remember that these estimated values are “effective” values of the natural frequencies which incorporate correction due to contributions such as parametric noise, frequency shift, etc.

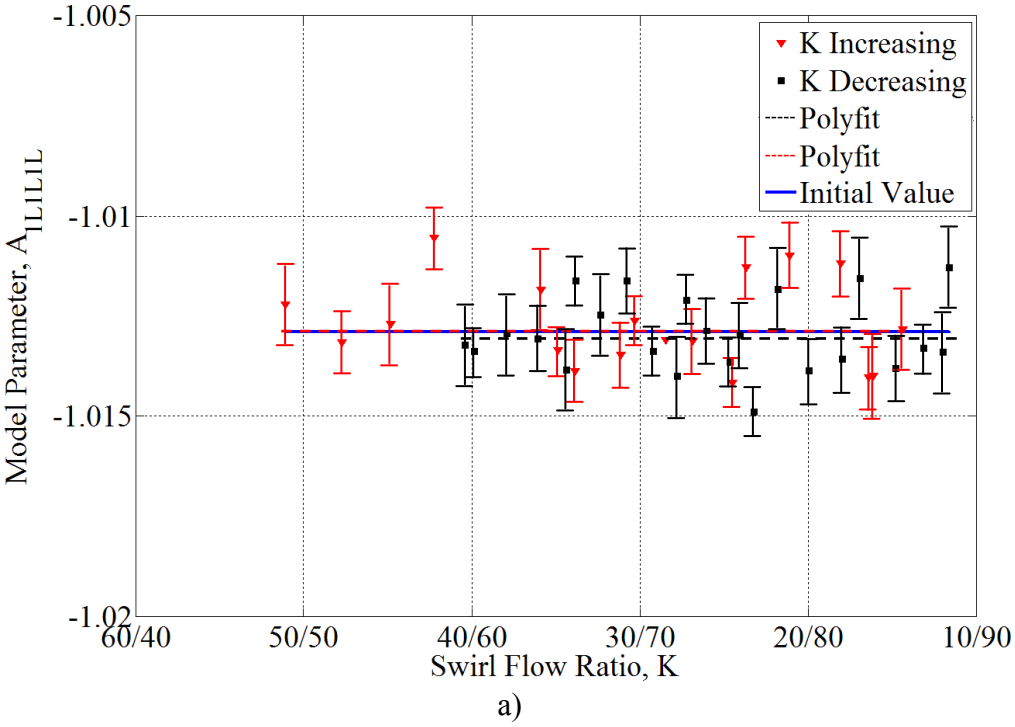


a)

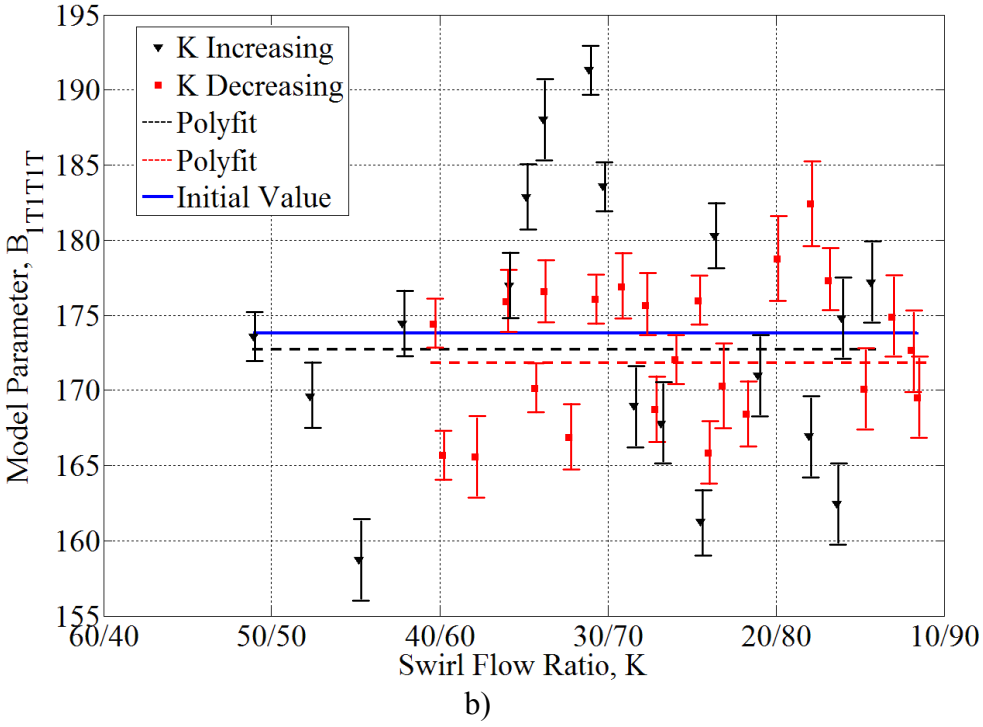


b)

Figure 6.6: Dependence of the estimated parameters from non-linear gasdynamics upon changes in swirl flow ratio: a) $A_{1L1L1L}$; b) $B_{1T1T1T}$; c) $A_{1L1T1T}$; d) $A_{1L1L1T} = A_{1L1T1L}$; e) $A_{1T1L1L}$; f) $A_{1T1T1L} = A_{1T1L1T}$; g) $A_{1T1T1T}$; h) $B_{1L1L1L}$; i) $B_{1L1L1T} = A_{1L1T1L}$; j) $B_{1T1L1L}$; k) $B_{1L1T1T}$; and l) $B_{1T1T1L} = B_{1T1L1T}$.

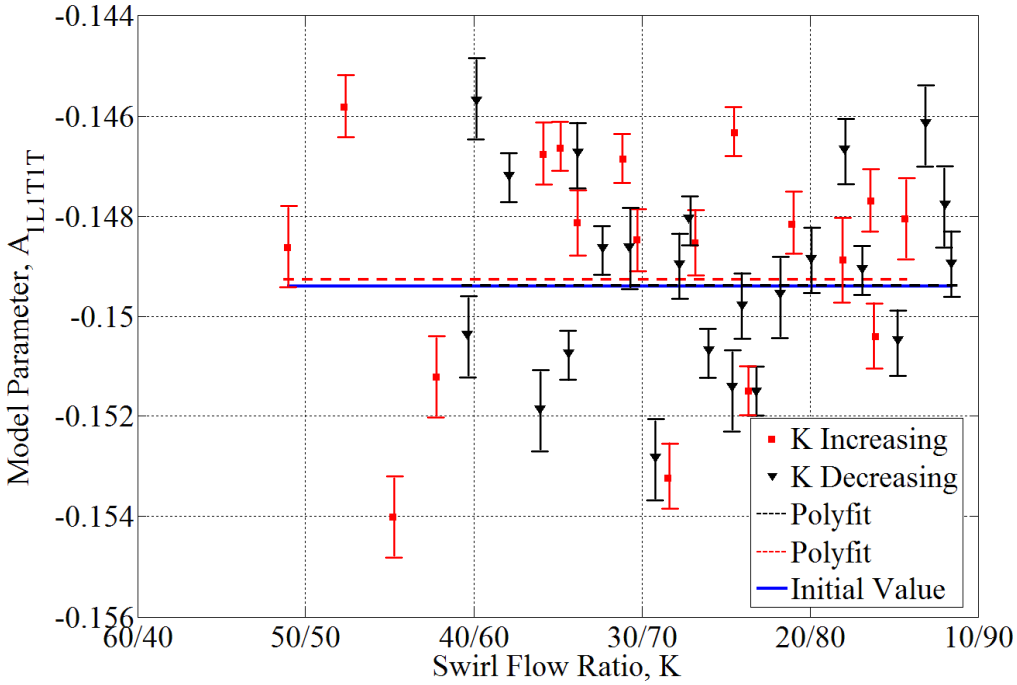


c)

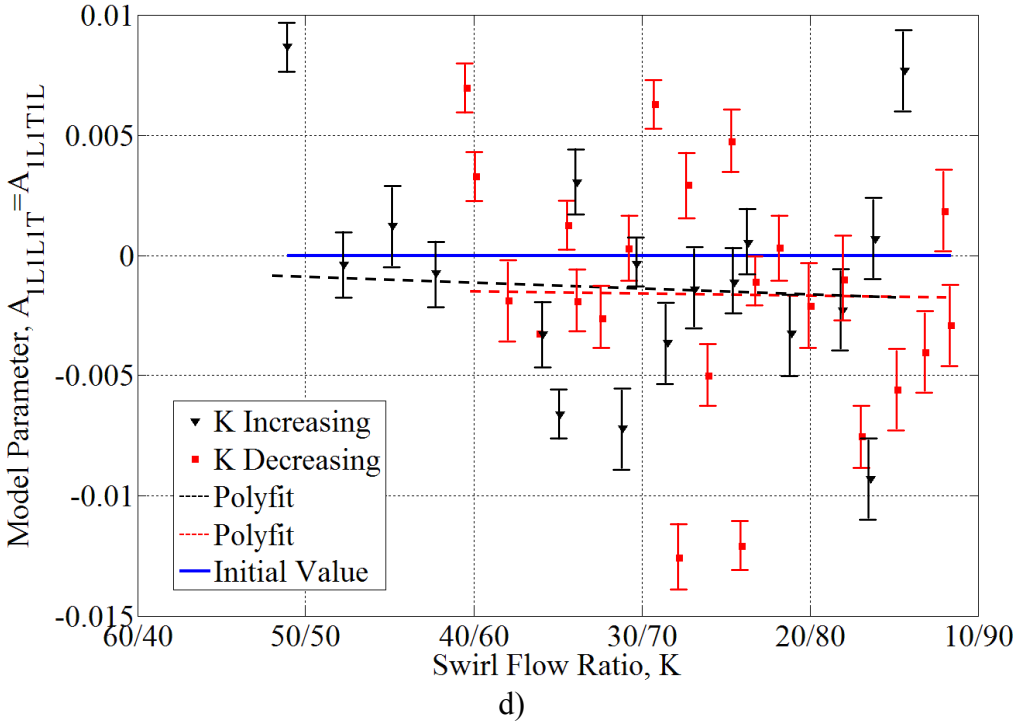


d)

Figure 6.6: continued…

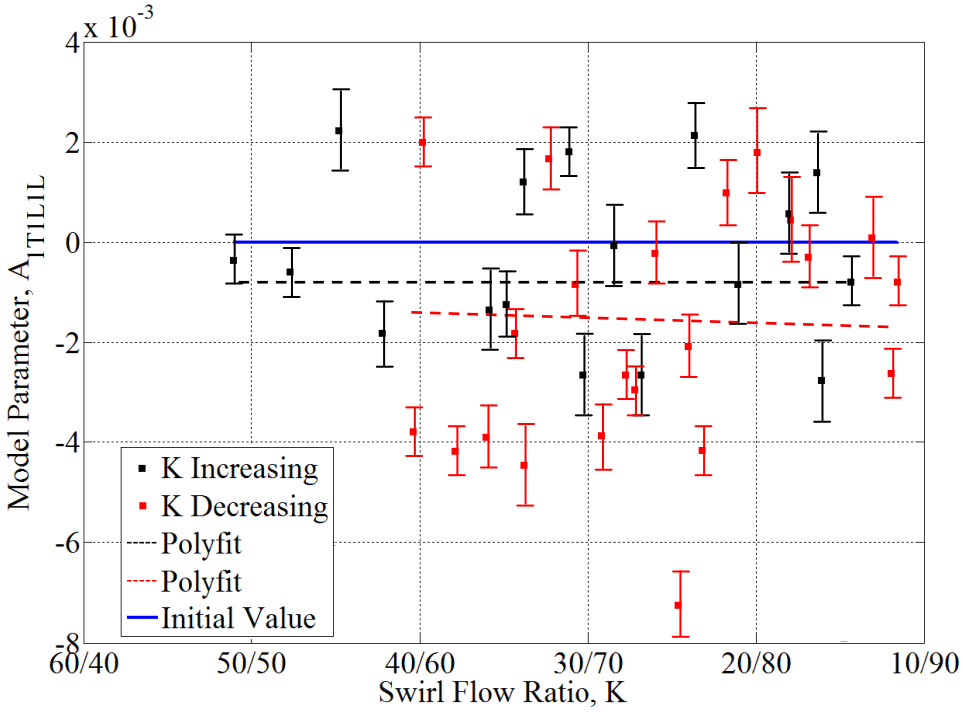


e)

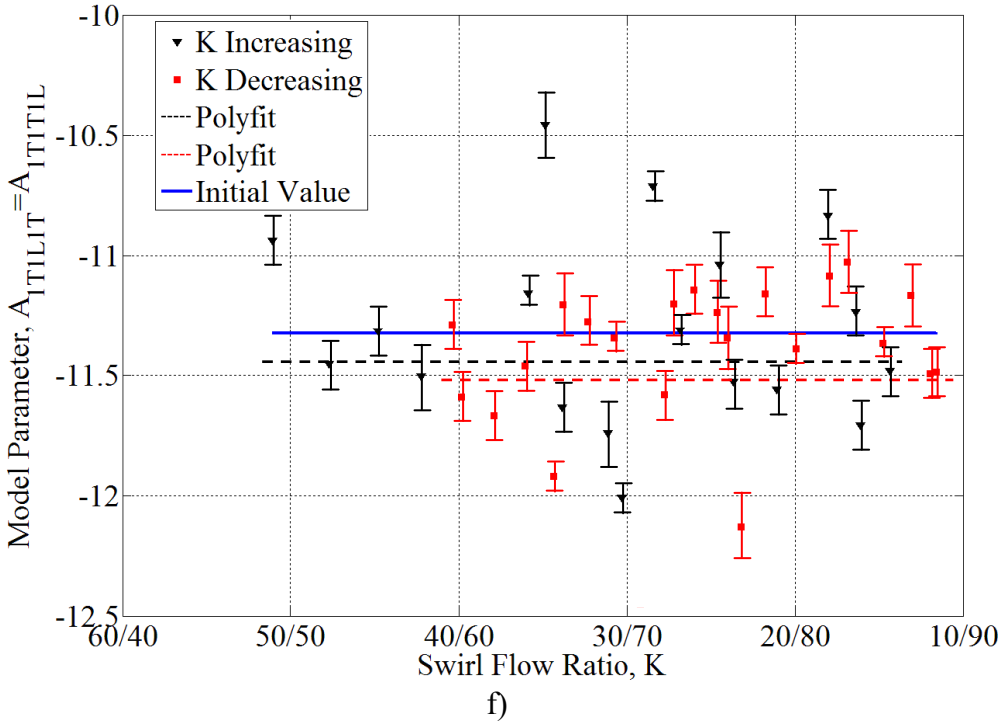


f)

Figure 6.6: continued…

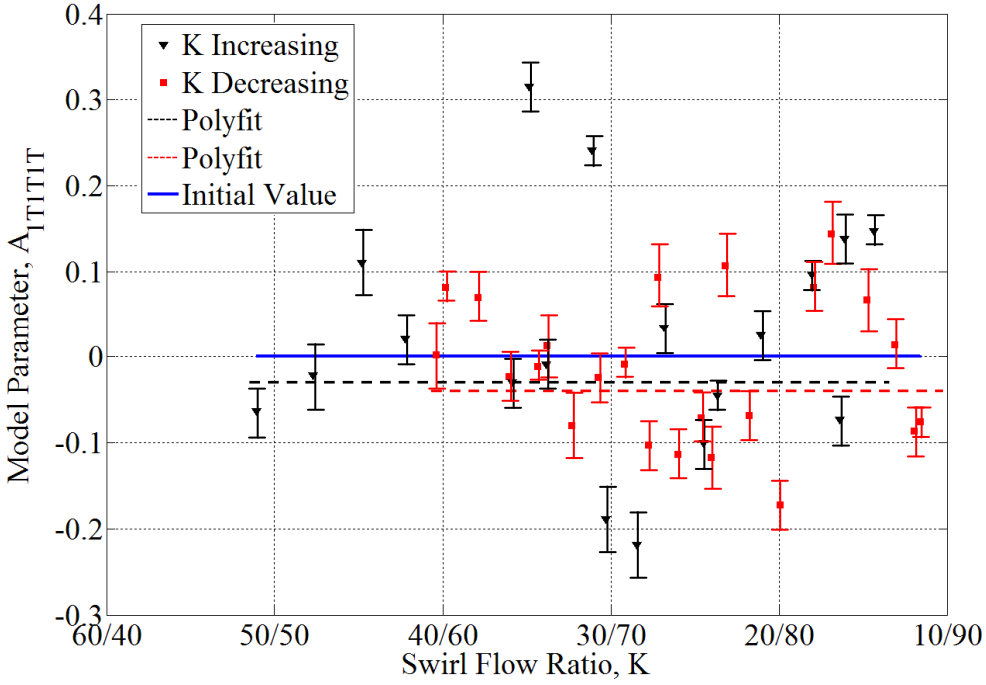


g)

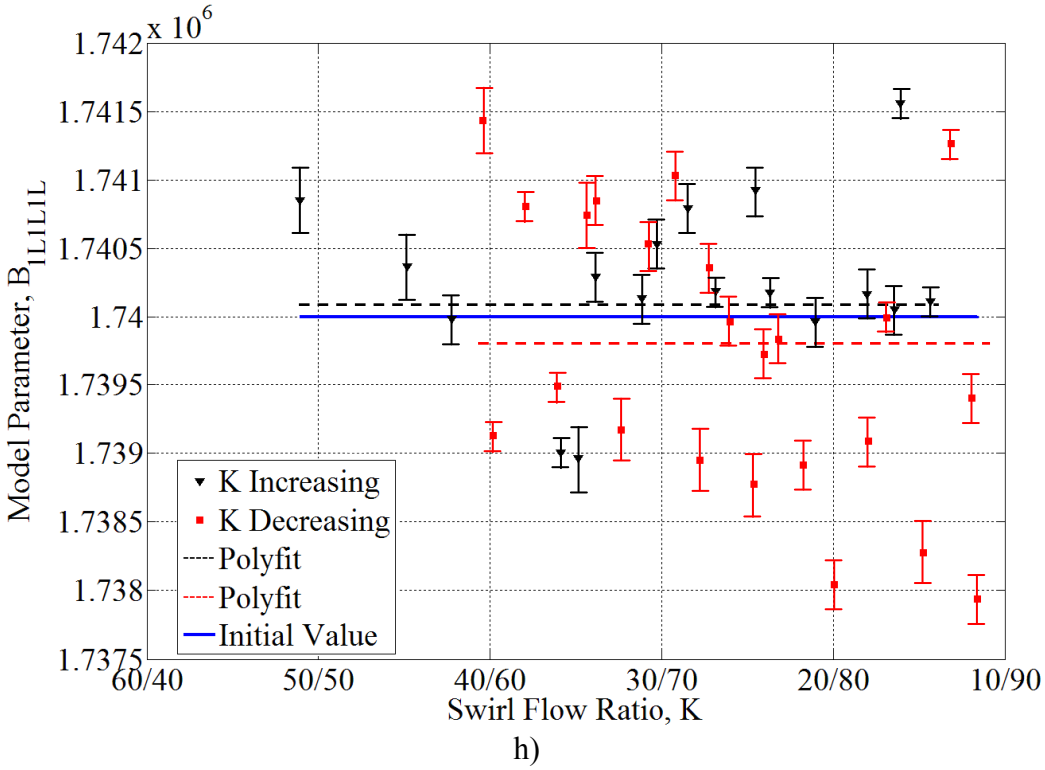


h)

Figure 6.6: continued…

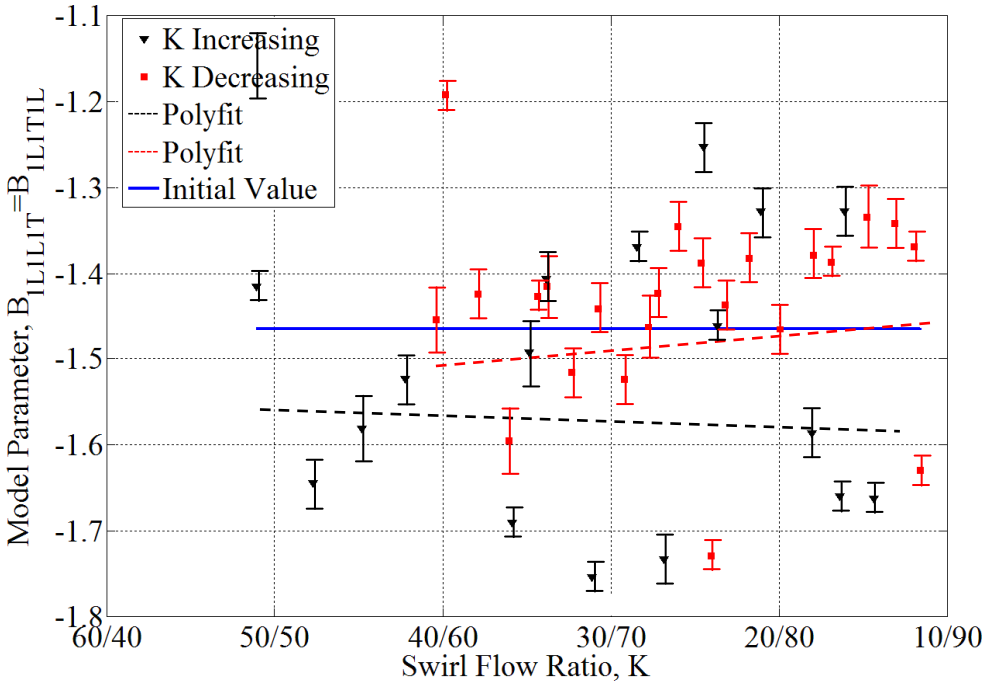


i)

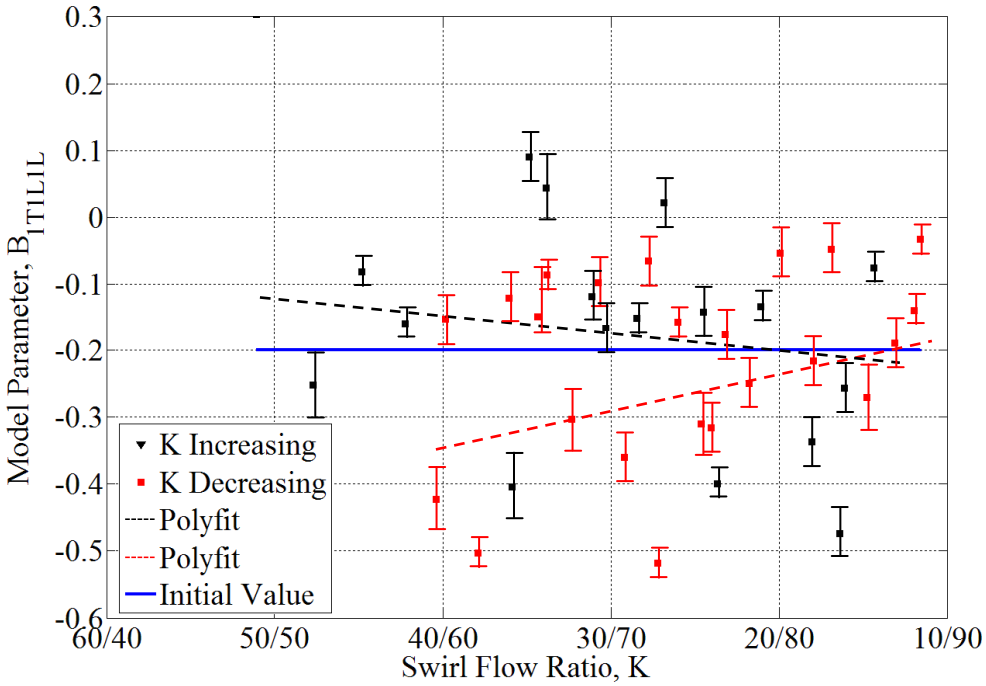


j)

Figure 6.6: continued…

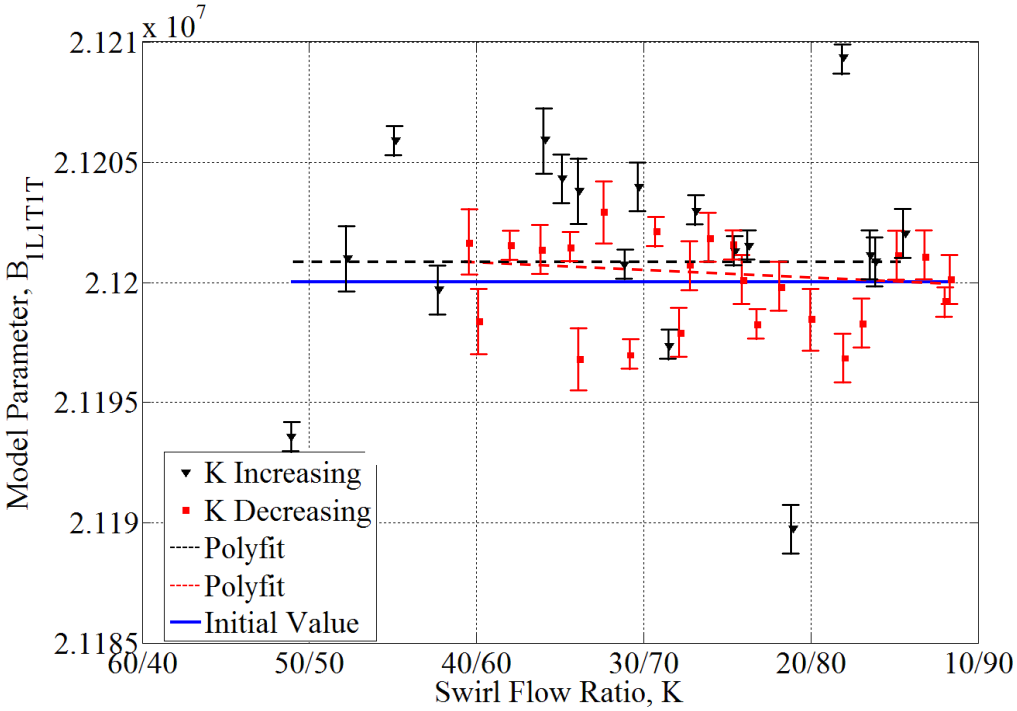


k)

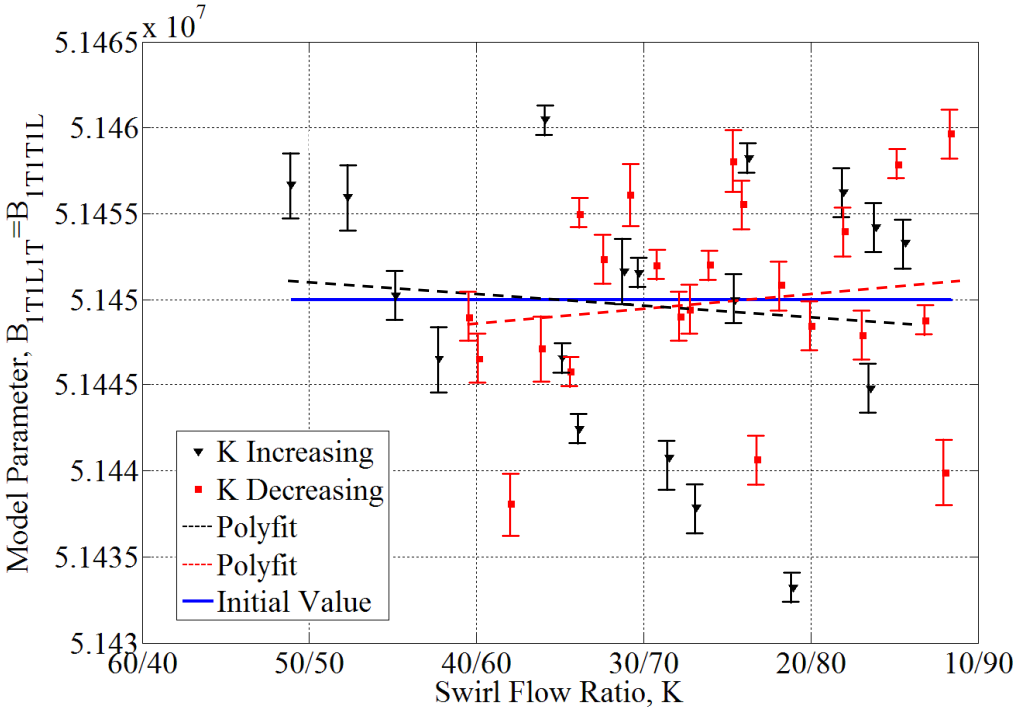


l)

Figure 6.6: continued…

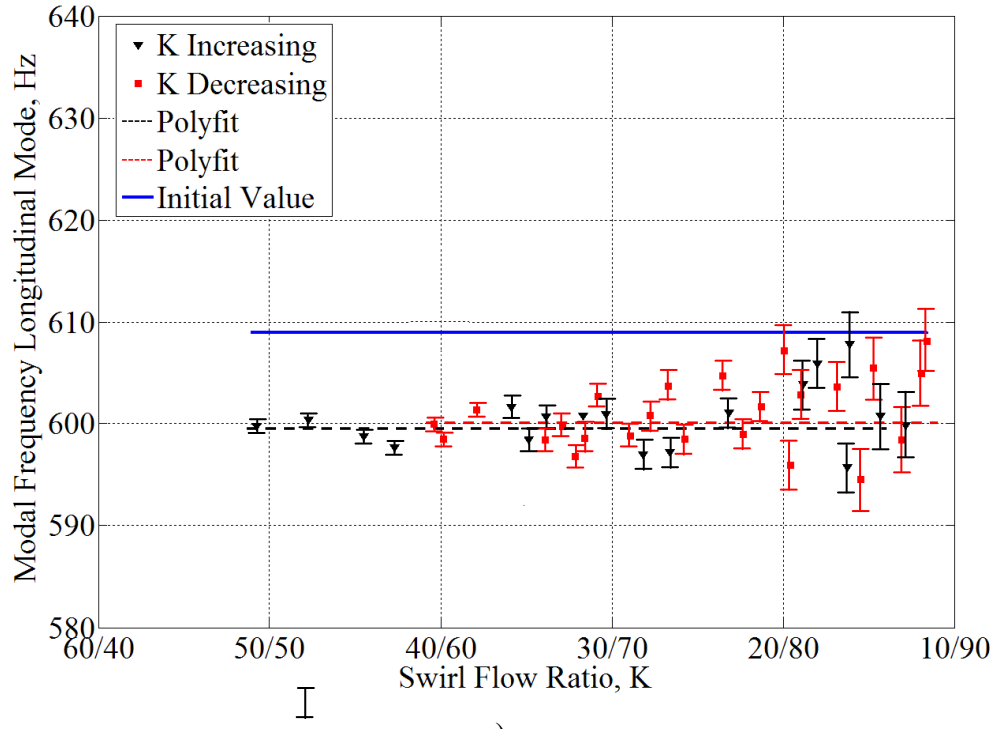


a)

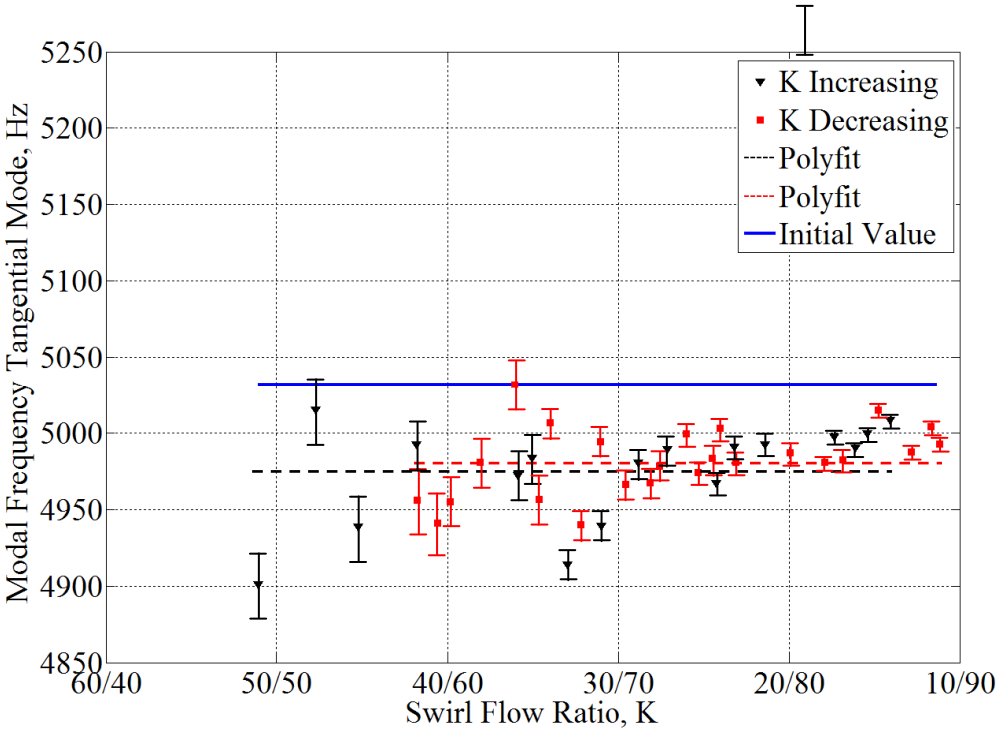


b)

Figure 6.7: Dependence of the estimated modal frequencies upon changes in swirl flow ratio: a) first longitudinal mode; and b) first tangential.

Figures (6.8a) and (6.8b) show the dependence of the estimated values of the modal damping ratios upon changes in the swirl flow ratio. The first observation is that both modes present negative damping, even in the range of control parameter in which the combustor was considered stable. This implies that both modes were under small amplitude limit cycle operation. In general, as the value of the control parameter decreases the damping ratios of both modes also decrease. When the control parameter increases the damping ratios increase. However, in the region of unstable operation; i.e., for value of *K* smaller than 22/78 (after the onset of tangential instability) the estimated damping ratios are approximately constant. Similarly, in the region of stable operation; i.e., for values of K larger than 40/60 (very small amplitude oscillations) the damping ratios are almost constant. This qualitative behavior of the damping ratios is similar to the behavior captured by the linear system identification approach in Chapter 5.

Figures (6.9a) and (6.9b) show the dependence of the estimated values of the parameters related to the source term due to the unsteady heat release, $a_{1L}$ and $a_{1T}$. One can note that the estimated values of both $a_{1L}$ and $a_{1T}$ show a certain tendency to increase as the value of the swirl flow ratio decreases and vice-versa.

Next, the results of the estimates for $c_{1L}$ and $c_{1T}$ are shown in Figures (6.10a) and (6.10b), respectively. Figure (6.10a) indicates that $c_{1L}$ decreases as the swirl flow ratio decreases and vice-versa, whereas Figure (6.10b) indicates that there is no clear dependence of $c_{1T}$ upon changes in the control parameter.

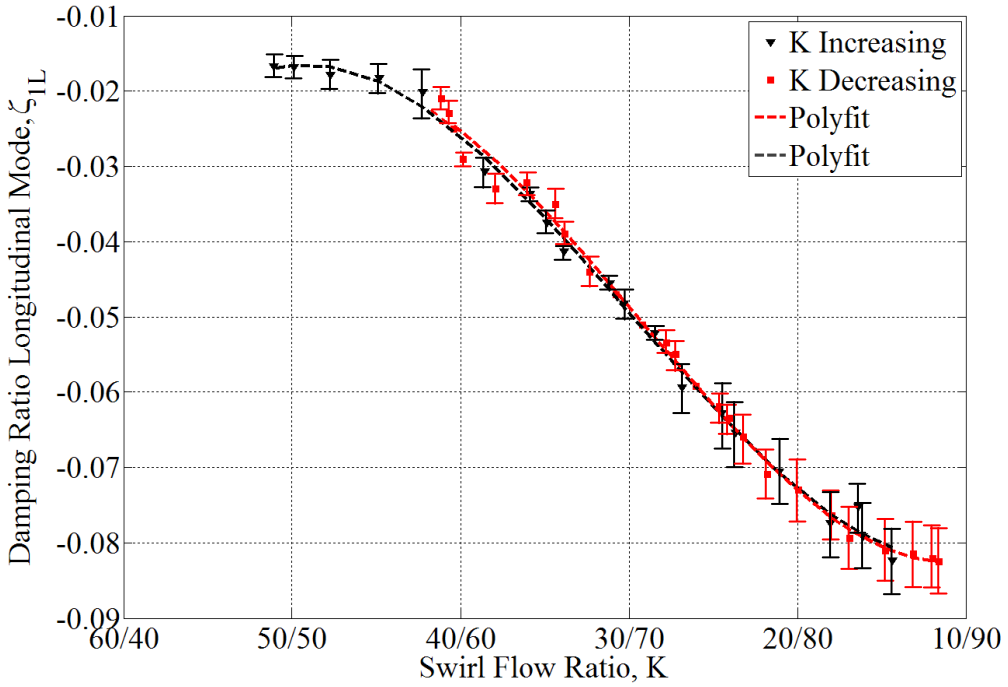


a)

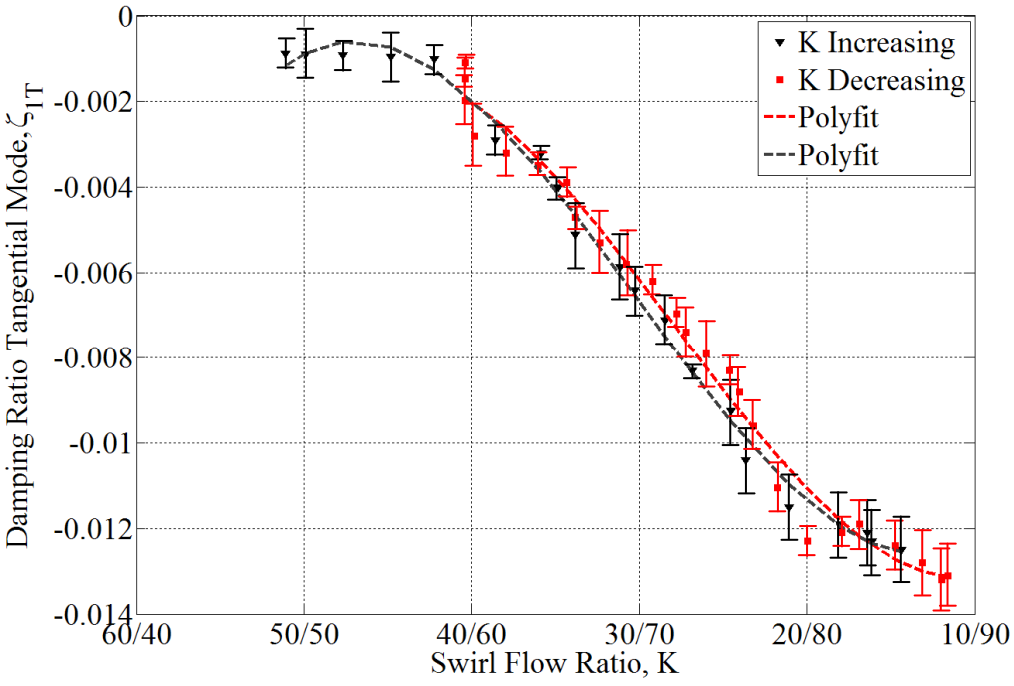


b)

Figure 6.8: Dependence of the estimated modal damping ratios upon changes in swirl flow ratio: a) first longitudinal mode; and b) first tangential.

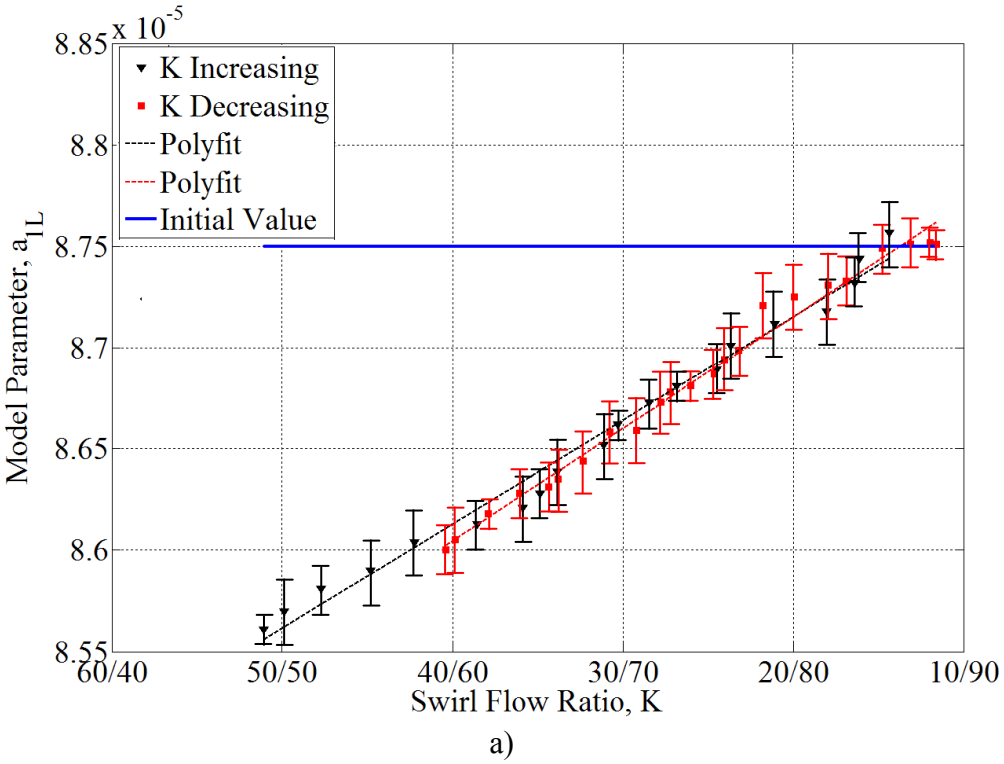


a)

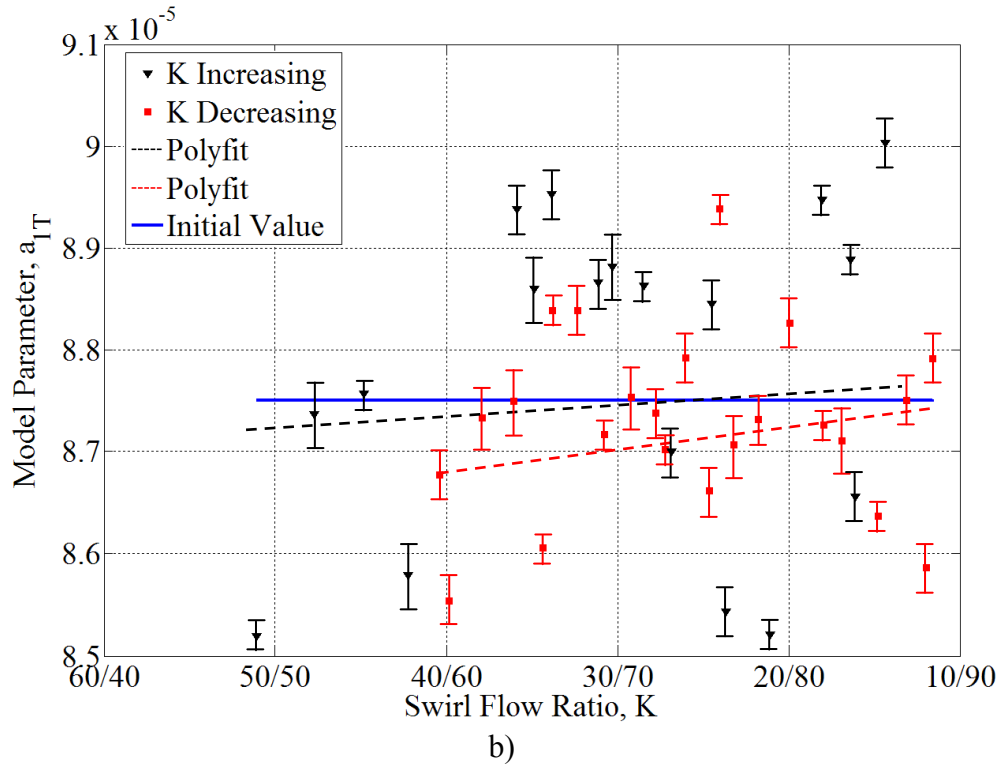


b)

Figure 6.9: Dependence of the estimated model parameters related to the source term due to unsteady heat release upon changes in swirl flow ratio: a) $a_{1L}$ ; and b) $a_{1T}$ .

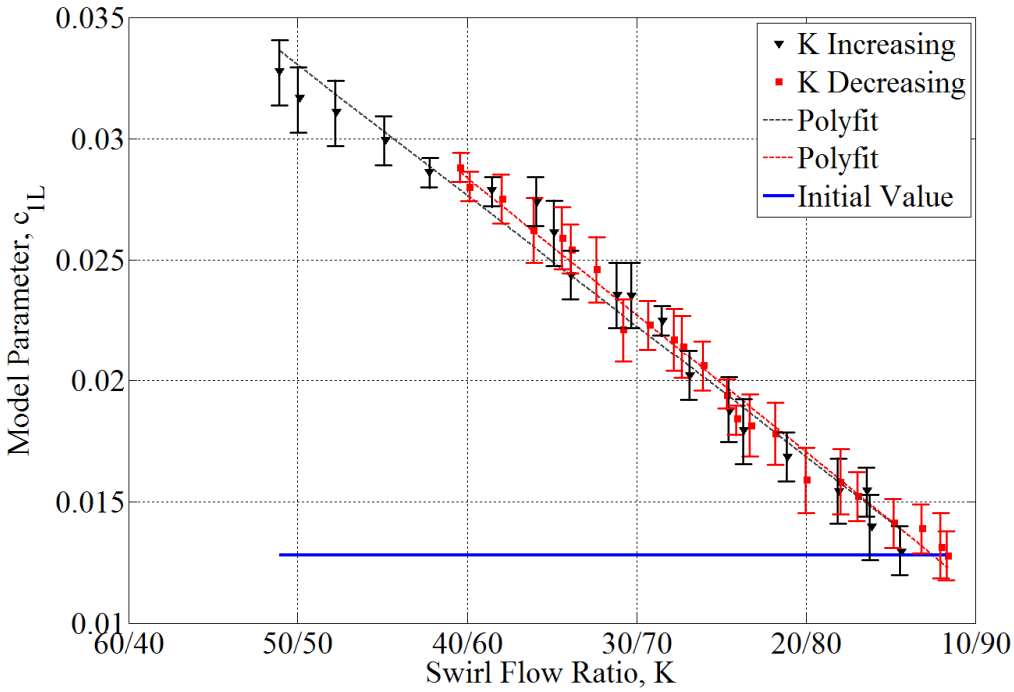


a)

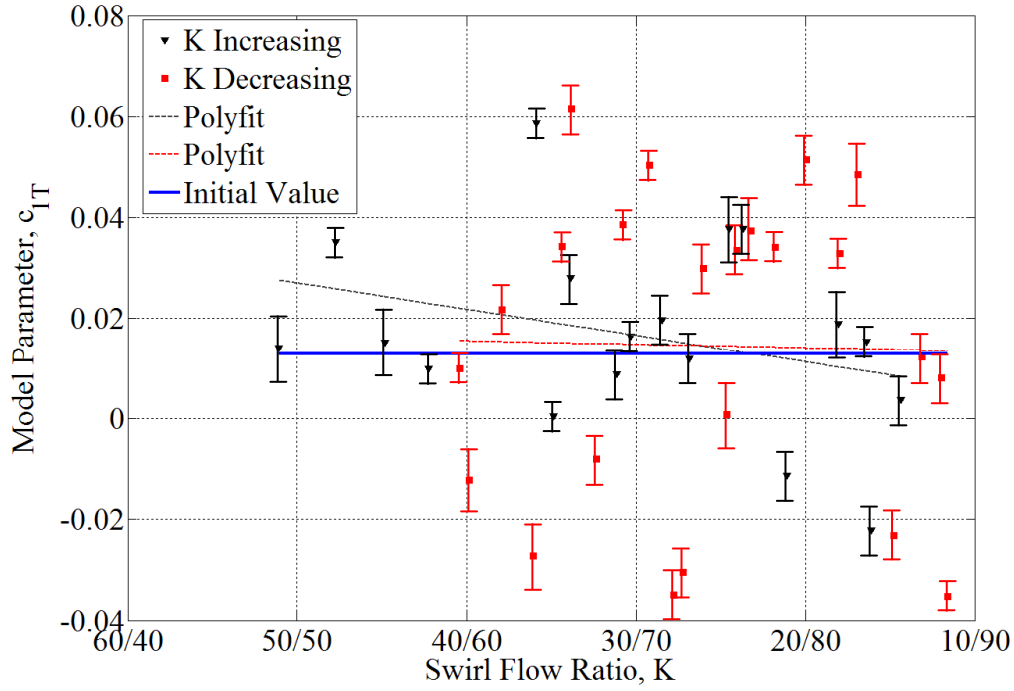


b)

Figure 6.10: Dependence of the estimated model parameters $c_{1L}$ and $c_{1T}$ upon changes in swirl flow ratio: a) $c_{1L}$; and b) $c_{1T}$.

The last physical parameter whose estimates were analyzed is $b_1$. Figure (6.11) shows the dependence of the estimates upon changes in the swirl flow ratio. The results indicate that there is no clear dependence of $b_1$ on the control parameter, $K$. The analysis and physical interpretation for all of these results will be given in the next section.

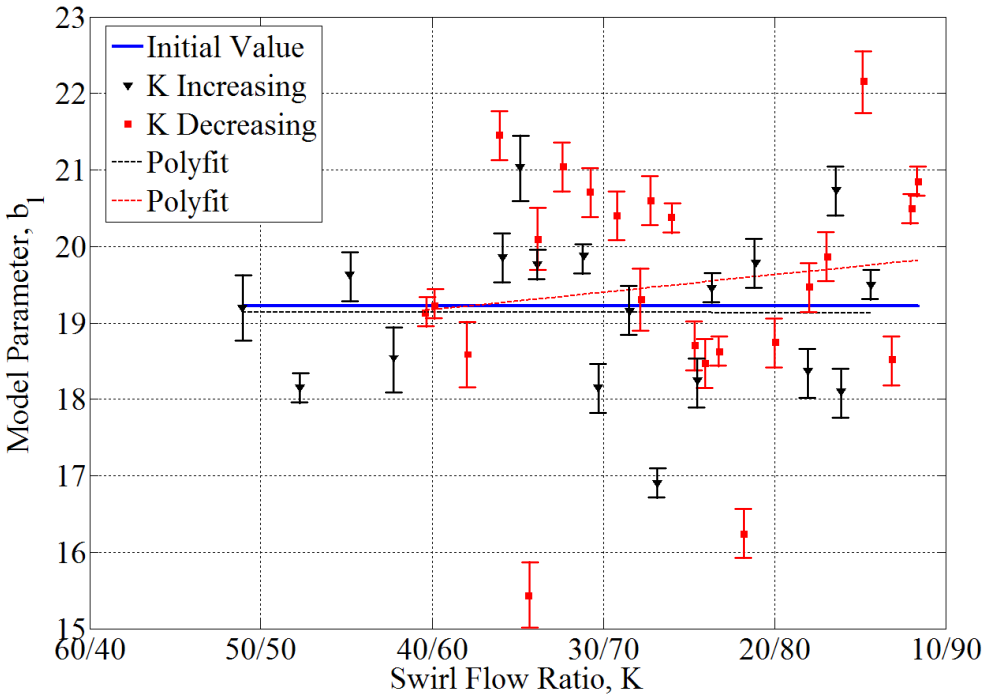


Figure 6.11: Dependence of the estimated model parameters $b_1$ upon changes in swirl flow ratio.

Next, we present the results of the estimates of the non-physical parameters $b_2$ and $b_3$. As mentioned before their initial values were set equal to unity and their range to the interval [0,10]. Figure (6.12a) shows the dependence of the estimates for the parameter $b_2$ upon changes in swirl flow ratio. The results indicate that the estimated value of $b_2$ is independent of the swirl flow ratio and oscillates around the initial value of

unity. Figure (6.12b) shows the dependence of the estimates for the parameter $b_3$ upon changes in swirl flow ratio. The results indicate that the estimated value of $b_3$ is also independent of the swirl flow ratio and oscillates around a mean value close to 10 (the upper boundary of its range).

To make sure that the chosen range for the values of these and all other parameters had no influence upon their estimated values, the parameter estimation procedure was repeated with a wider ranges. The results were qualitatively the same; that is, the estimated value of $b_2$ oscillated around unity and the estimated value of $b_3$ oscillated around a mean value near 10.

### 6.5.4 Analysis of the Results

The main advantage of a gray-box modeling is the possibility of interpreting the results obtained for the model parameters based on the physics of the system. Thus, the results presented for all the estimated physical parameters can be analyzed and one can verify if these results have physical explanation.

We start the analysis with the estimated damping ratios. The first observation is the negative damping ratios for both modes (longitudinal and tangential). That implies the nonlinearities in the system are acting to saturate the amplitude of the oscillations at limit cycle amplitude. This type of behavior has been reported in many investigations in the literature[9-14],[65]. As the swirl flow ratio is decreased the damping ratios also decrease. Thus, physical processes in the system which are responsible for dissipating/removing energy from the unstable modes become less efficient as the swirl flow ratio decreases. Consequently, the limit cycle amplitude reached by each mode increases.

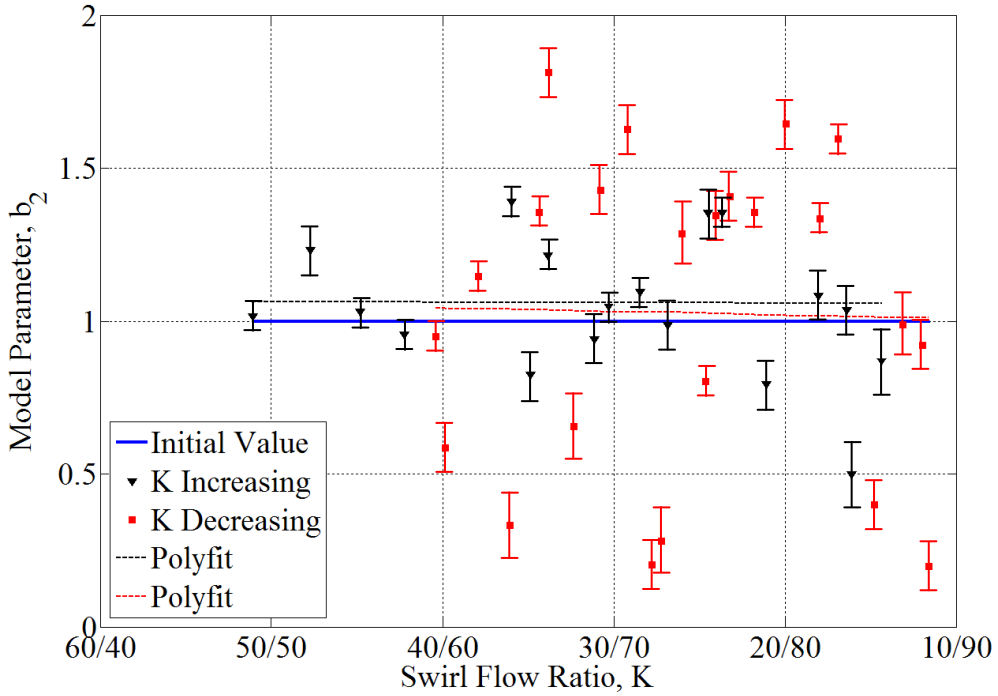


a)

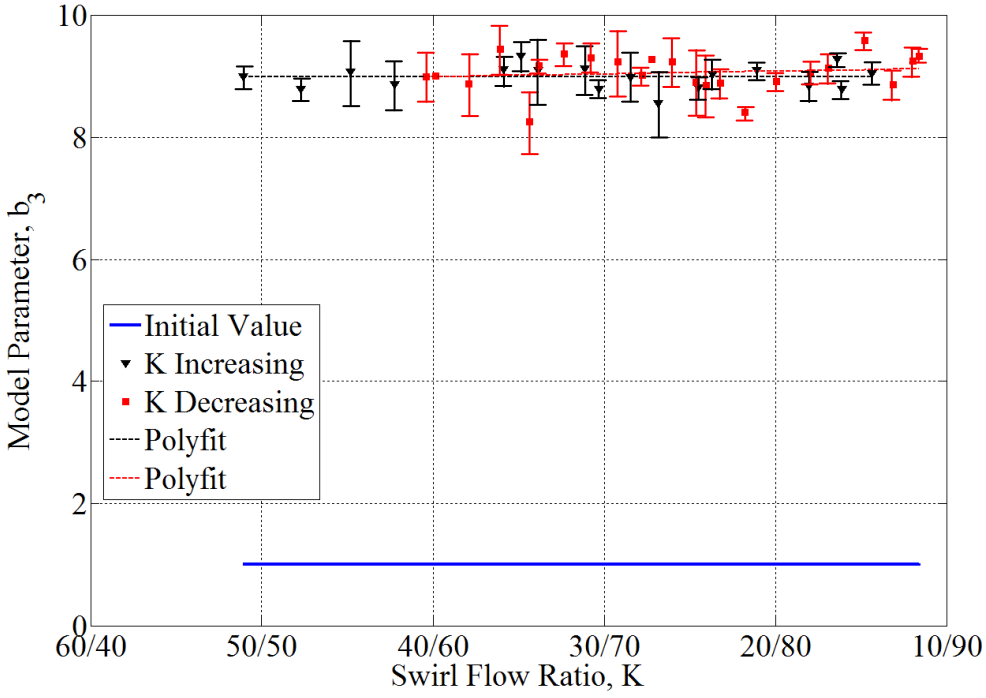


b)

Figure 6.12: Dependence of the estimated model parameters $b_2$ and $b_3$ upon changes in swirl flow ratio: a) $b_2$; and b) $b_3$.

The results shown in the previous section, indicated that the estimated values for the following parameters were approximately independent upon changes in the control parameter $K$: $A_{1L1L1L}$; $B_{1T1T1T}$; $A_{1L1T1T}$; $A_{1L1L1T} = A_{1L1T1L}$; $A_{1T1L1L}$; $A_{1T1T1L} = A_{1T1L1T}$; $A_{1T1T1T}$; $B_{1L1L1L}$; $B_{1L1L1T} = A_{1L1T1L}$; $B_{1T1L1L}$; $B_{1L1T1T}$; $B_{1T1T1L} = B_{1T1L1T}$; and modal natural frequencies ( $\tilde{f}_{1L}$ and $\tilde{f}_{1T}$ ) . This result validates our modeling by which these parameters depend on the geometry and boundary conditions in the combustor. Similarly, the results for the estimated values of the model parameter $b_1$ also show independence upon $K$, in agreement with the expression shown in Equation (6.52).

Next, we analyze the parameters whose values are functions of the coordinates of the flame or heat release location; that is, $a_{1L}$ , $a_{1T}$ , $c_{1L}$ , and $c_{1T}$ . As the parameters $a_{1T}$ and $c_{1T}$ do not have closed form expressions for their calculations, our analysis is based on the results for $a_{1L}$ and $c_{1L}$ . From Equations (6.50) and (6.55) we have

$$\begin{aligned} a_{1L} &\propto \cos(k_{1L}x_f) \\ c_{1L} &\propto \sin(k_{1L}x_f) \end{aligned} \tag{6.58}$$

Since the results indicates that $a_{1L}$ increases as the swirl flow ratio decreases and the opposite happens with $c_{1L}$ , one can assume that the flame location (or the region of concentrated heat release) moves closer to the injector plate ( $x_f$ decreases) as the swirl flow ratio decreases.

The validation of this assumption is performed by comparing the results obtained in this research with the experimental investigation of Lubarsky and Zinn[65]. In their investigation, the stationary and oscillatory heat release distributions along the reaction zone of the LRECS were characterized at different regimes of combustion dynamics. For

this purpose the LRECS was scanned by a step movement of the optical sensor at different regimes of combustion dynamics.

The influence of $K$ variation upon the profiles of the stationary heat release at constant equivalence ratio is shown in the Figure 6.13. It is clearly seen that $K$ value changes the profile of the flame intensity dramatically. One can note that for very low values of swirl flow ratio (e.g., $K$=16/84) the heat release concentrates in a narrow zone about 40mm near the injector face (at these conditions tangential instability was typically observed). On the contrary, at higher swirl flow ratios (e.g., $K$=78/22) the flame intensity profile is flatten and the heat release is concentrated in a wider zone (about 118mm near the injector plate).

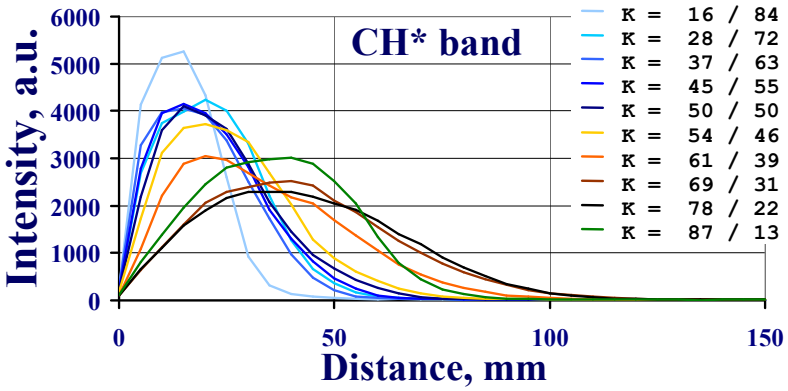


Figure 6.13: Stationary heat release profiles at different values of swirl flow ratio obtained by processing the spectrometer data in the CH* band[65].

The distance in the horizontal axis corresponding to the peaks in the flame intensity profiles can be assumed a measure of the flame location as a function of the swirl flow ratio. In this sense, Figure 6.13 confirms the results of the estimated values of the model parameters $a_{1L}$ and $c_{1L}$, which indicated that the flame location moves closer

to the injector plate as the swirl flow ratio is decreased. However, in the investigation of Lubarsky and Zinn[65] the location of the maximum heat release did not changes gradually with *K* rather revealed kind of step behavior, which was assumed a consequence of the reorganization (rebuilding) of the vortex system holding the flame in the LRECS.

During the derivation of the finite-dimensional model in Chapter 4, we introduced the variable $u_f$, the oscillating acoustic velocity at the flame location, as a way of replacing the time delays in the model. The relationship between the time delay and the coordinate $x_f$ is straightforward. Thus, the results presented in this research confirm the capability of the "smart" injectors of changing the stability characteristics of the LRECS by changing the spray pattern and, ultimately, the combustion time in the system.

### 6.5.5 Operational Stability Margin Assessment

In Chapter 5, the linear system approximation allowed us to assess directly the stability margin of the LRECS by looking at the estimated modal damping ratios; that is, the modal damping ratios were a measure of the stability of the system. The closer the value of a modal damping ratio is to zero, the smaller the stability margin of the combustor regarding that mode. One could assume that the modal damping ratios varied linearly with the swirl flow ratio, so that the assessment of the stability margin as a function of changes in the control parameter *K* was performed.

As for the mentioned linear system approach, the behavior of the combustor described by the non-linear dynamical model in this chapter also depends on the values of its parameters. However, we cannot infer the stability margin of the system by simply looking at the value of any parameter, because there is no indication of which value would correspond to the stability limit. The stability margin needs to be determined by

numerical simulations of the dynamical system response based on the information collected about the model parameters via system identification.

Since the functional dependence of the model parameters upon the swirl flow ratio can be determined from the results presented in the previous section, we can write the dynamical model defined by Equations (6.11-13) as

$$\frac{d\mathbf{x}_t}{dt} = \mathbf{f}(\mathbf{x}_t, \boldsymbol{\theta}(K)) + \mathbf{W}_t \approx \mathbf{F}(\mathbf{x}_t, K) \tag{6.62}$$

Using this approximated representation, the behavior of the combustor system can be studied by applying methods of dynamical systems theory to create bifurcations diagrams. In particular, the current investigation uses the packages MATCONT and CL_MATCONT by Govaerts et al[66] to perform a local continuation of steady-states, periodic solutions, folds and limit cycle curves. The control parameter, *K*, was used as the continuation parameter. The mathematical description of the method as well as its implementation in the form of a MATLAB® toolbox can be found in reference [66].

In writing the functions $\mathbf{F}(\mathbf{x}_t, K)$, the only model parameters presenting a linear dependence upon changes in *K* are $\tilde{\zeta}_{1L}$, $\tilde{\zeta}_{1T}$, $a_{1L}$, and $c_{1L}$. These functional dependences were determined by the best linear fit of these estimated values corresponding to the situation when the swirl flow ratio was decreased from $K \simeq 40/60$ to $K \simeq 22/78$ (before the onset of instability). The reason for that is to verify the capability of the model in predicting such instability when the value of the control parameter is decreased below $K \simeq 22/78$. All other parameters are constant. Figures (6.14a) and (6.14b) show the results of the application of the software of continuation method for this case.

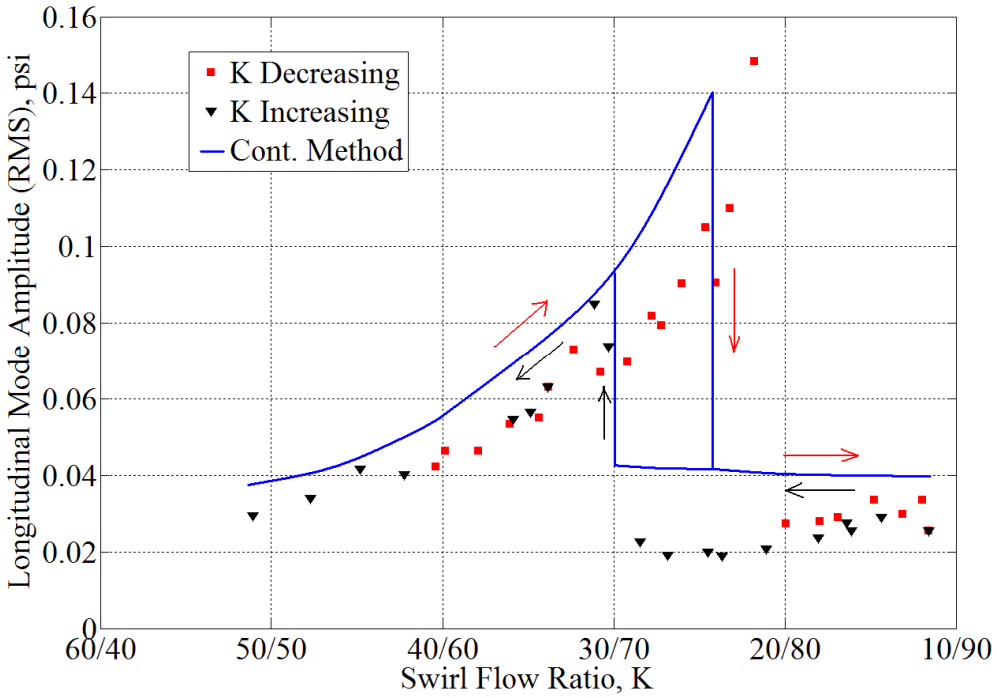


a)

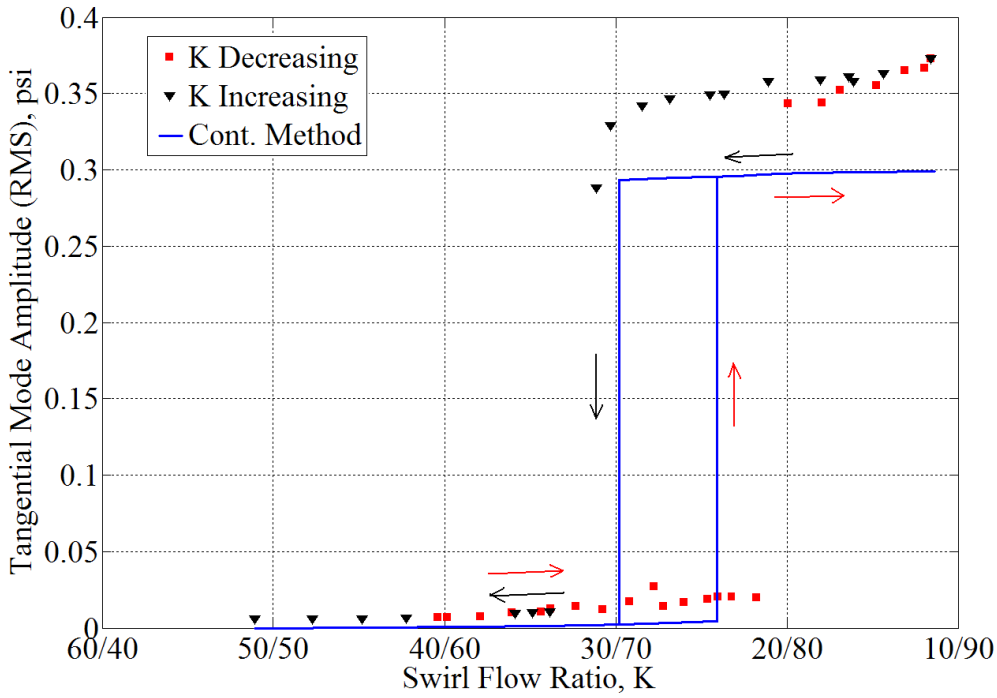


b)

Figure 6.14: Comparison between the predicted modal amplitude via continuation method and the actual values from experimental data: a) longitudinal mode; and b) tangential mode.

The results indicate that the model could capture the qualitative behavior of both modes very well, including the suddenly increasing in the tangential mode amplitude and decreasing of the longitudinal mode amplitude. This behavior has been reported in literature[63] and it is known as *two generators with competitive quenching*. The hysteretic behavior is also captured when the values of $K$ are swept back and forth. The values of the control parameter $K$ corresponding to the points of abrupt changes in amplitudes are also very well predicted. However, the model could not predict correctly the amplitudes of the oscillations.

The amplitudes are overestimated in the case of the longitudinal mode and underestimated for the tangential mode. We suspect that neglecting the stochastic excitation in the application of the continuation method can have an effect upon the predicted values of the amplitudes of the modes. Nevertheless, the results indicate that the methodology developed in this research can be used to predict the unstable behavior of our LRECS based on the application of the SID technique to the experimental data.

# CHAPTER 7

# CONCLUSIONS AND FUTURE WORK

The objective of this thesis was to develop a methodology by which the operational stability margin of a combustor could be assessed from available experimental data by applying modern and robust techniques from dynamical system identification. In this chapter, we present some of the findings and conclusions for this thesis and provide recommendations for future work.

In Chapter 4 we presented the analytical framework to derive a gray-box thermoacoustic model for the LRECS. The model is represented by a set of coupled stochastic differential equations with parametric and additive noise. Then, an analysis based on the method of dissipation energy balancing indicated that the parametric noise terms could be lumped in an effective damping ratio and effective stiffness. This assumption was validated by numerical simulations performed in Chapter 5. The linear coupling terms related to the gasdynamics were neglected. The simplified thermoacoustic model accounted for non-linear coupling due to gasdynamics, stochastic excitation (additive noise), and non-linear forcing due to the unsteady heat release. This is an original contribution of this research, since previous works in the field of system identification applied to combustion systems have not taken all of those effects into account in their models.

In the first application of the developed methodology, we assumed that the dynamics of the LRECS could be approximated by a set of linear oscillators. Thus, in Chapter 5 we presented the SSI-DATA technique implemented to estimate the modal

parameters; that is, effective modal damping ratios and frequencies. In this case, the modal damping ratios is already a measure of the operational stability margin, since a zero value for modal damping ratio implies the modal stability boundary. The application of the SSI-DATA technique to the experimental data revealed that expressing the modal damping ratios as a linear function of the control parameter, *K*, provided good estimates of the value of swirl flow ratio at which the system becomes unstable. Furthermore, the results also pointed out which mode has the largest operational stability margin.

It was shown that the SSI-DATA technique has accuracy issues as the system approaches its stability boundary. The technique overestimates the values of the modal damping ratios as they approach zero. However, there is a doubt about the validity of the linear approximation as the system approaches unstable regime. In fact, as the system approaches instability, the amplitude of the oscillations increase and non-linear effects become important. Thus, this approximation should be applied carefully.

The linear approximation is not able to capture the hysteretic behavior (typically a nonlinearity indication). In real applications, one should avoid operating conditions in the region of bi-stability. Therefore, we extended our methodology to the non-linear stochastically excited system in order to capture the main features of the system behavior shown by the preliminary analysis of the experimental data. At this point, the model for the heat release dynamics played an important role.

The limitation of applicability of the SID technique to finite-dimensional dynamic models required that the heat release model could not include time delays. The heat release model presented in this research was based on previous investigations and on a black-box modeling using the measured dynamic pressure as input and the

chemiluminescence data as output. It provided a finite-dimension system of stochastic differential equations as necessary. However, its derivation was based on the assumption of small time delays which cannot be supported by the necessary condition for combustion instabilities, $\tau_{acous} \approx \tau_{comb}$. Therefore, the proposed model should be considered a first order non-linear approximation of the real time-delayed system.

To estimate the parameters of the finite-dimension model a system identification technique based on the prediction error method (PEM) was implemented which has the extended Kalman filter (EKF) as the tool for reducing the problems with convergence in the numerical algorithm. The technique requires that initial values as well as range of values for the model parameters must be given. In this sense, the gray-box modeling played a fundamental role, since it provided expressions to calculated most of the parameters based on known characteristics of the system (geometry, boundary conditions, thermodynamic properties, etc.).

It was verified that, theoretically, many of the physical parameters did not depend on changes in the swirl flow ratio, and, therefore, should remain constant at all values of *K*. The results of the model parameter estimation confirmed such independence. The results also indicated that the behavior of some of the estimated model parameters can be used to obtain information about the dependence of the flame location upon changes in the control parameter.

The identified model and its parameters were used to predict the behavior of the system upon changes in the parameter K, using a continuation method. The overall behavior of the amplitude of the oscillations of the two modes considered in this research was very well captured. In particular, the results from the bifurcation diagram showed

regions of bi-stability similar to the experimental data. Besides, values of the control parameter $K$ corresponding to the onset and decay of instability were in good agreement with the experimental data.

As a conclusion, the methodology developed in this thesis can be applied to assess the operational stability margin of the LRECS from the experimental data collected before the onset of instability. If it is expected that the combustor will present hysteretic behavior, the linear approximation should be used to obtain initial values for the modal frequencies and damping ratios.

As recommendations for future works, we can enumerate:

1) Better model parameter estimation can be obtained if one excites externally the system (e.g., using a speaker) so that an input is available for the input-output SID technique. Besides, the computational time which is an issue for active control applications can also be reduced;

2) Investigations must be performed to provide a finite-dimension model for the heat release dynamics in which the relationship between the model parameters and the time-delays can be explicitly expressed; and

3) After the improvements mentioned above have been implemented, the implementation of recursive model parameter estimation would allow the application of the developed methodology for on-line operational stability margin assessment.

# APPENDIX A

# EQUATIONS OF MOTION

The equations for the unsteady motion in combustion chambers were derived in the work of Culick[2]. Here we just present the basic concepts applied in the derivation. If both fuel and oxidizer are liquid, the first idea is to lump the liquid fuel and oxidizer together as a single liquid phase. The multi-component gas mixture is represented as a single average gas. Thus, we have the following equations for this two-phase mixture:

- Conservation of Mass:

$$\frac{\partial(\rho_g + \rho_l)}{\partial t} + \nabla.(\rho_g \mathbf{u}_g + \rho_l \mathbf{u}_l) = 0 \tag{A.1}$$

- Conservation of Momentum:

$$\frac{\partial(\rho_g \mathbf{u}_g + \rho_l \mathbf{u}_l)}{\partial t} + \nabla.(\rho_g \mathbf{u}_g \mathbf{u}_g + \rho_l \mathbf{u}_l \mathbf{u}_l) = \nabla.\tau_g \tag{A.2}$$

- Conservation of Energy:

$$\frac{\partial(\rho_g e_{g0} + \rho_l e_{l0})}{\partial t} + \nabla.(\rho_g \mathbf{u}_g e_{g0} + \rho_l \mathbf{u}_l e_{l0}) = \nabla.(\tau_g.\mathbf{u}_g) - \nabla.\mathbf{q}_g + Q \tag{A.3}$$

where the subscripts $g$, $l$, and $0$ refers to gas species, liquid phase and stagnation state, respectively. The internal heat flow, $\mathbf{q}_g$, is approximated by Fourier's law for the gas phase and $Q$ represents heat addition in the gas phase due to combustion processes. The stress tensor is written as the sum of the isotropic pressure and the viscous stress tensor as

$$\tau_g = -p\mathbf{I} + \tau_v \tag{A.4}$$

For a mixture the perfect gases with constant specific heat, the stagnation energy can be written as

$$e_{g0} = C_\upsilon T_g + u_g^2 / 2 \tag{A.5}$$

where $C_\upsilon$ and $u_g$ are mass averaged values over all gaseous species.

If we denote by $w_l$ the rate at which liquid phase is converted to gas we can write the conservation of mass of gas phase as

$$\frac{\partial \rho_g}{\partial t} + \nabla.(\rho_g \mathbf{u}_g) = w_l \tag{A.6}$$

and for the liquid phase

$$\frac{\partial \rho_l}{\partial t} + \nabla.(\rho_l \mathbf{u}_l) = -w_l \tag{A.7}$$

Next, we define the slip velocity between the condensed and gas phase as

$$\delta \mathbf{u}_l = \mathbf{u}_l - \mathbf{u}_g \tag{A.8}$$

Equation (A.1) can be written as

$$\begin{aligned} &\frac{\partial(\rho_g + \rho_l)}{\partial t} + \nabla.(\rho_g \mathbf{u}_g + \rho_l \mathbf{u}_g) = -\nabla.(\rho_l \mathbf{u}_l - \rho_l \mathbf{u}_g) \Rightarrow \\ &\frac{\partial \rho}{\partial t} + \nabla.(\rho\, \mathbf{u}_g) = -\nabla.(\rho_l \delta \mathbf{u}_l) = \mathcal{W} \end{aligned} \tag{A.9}$$

Substituting Equation (A.4) into Equation (A.2) and expanding the resultant expression we have

$$\begin{aligned} &\rho_g \frac{\partial \mathbf{u}_g}{\partial t} + \mathbf{u}_g \frac{\partial \rho_g}{\partial t} + \rho_l \frac{\partial \mathbf{u}_l}{\partial t} + \mathbf{u}_l \frac{\partial \rho_l}{\partial t} + \rho_g \mathbf{u}_g.\nabla \mathbf{u}_g + \rho_l \mathbf{u}_l.\nabla \mathbf{u}_l \\ &+\mathbf{u}_g \nabla.(\rho_g \mathbf{u}_g) + \mathbf{u}_l \nabla.(\rho_l \mathbf{u}_l) = \nabla.(-pI + \tau_\upsilon) \Rightarrow \\ &\mathbf{u}_g \left[ \frac{\partial \rho_g}{\partial t} + \nabla.(\rho_g \mathbf{u}_g) \right] + \mathbf{u}_l \left[ \frac{\partial \rho_l}{\partial t} + \nabla.(\rho_l \mathbf{u}_l) \right] + \rho_g \frac{\partial \mathbf{u}_g}{\partial t} + \rho_l \frac{\partial \mathbf{u}_l}{\partial t} \\ &+\rho_g \mathbf{u}_g.\nabla \mathbf{u}_g + \rho_l \mathbf{u}_l.\nabla \mathbf{u}_l = \nabla.(-pI + \tau_\upsilon) \end{aligned} \tag{A.10}$$

Substituting Equations (A.6) and (A.7) into Equation (A.10) one obtains

$$w_l(-\mathbf{u}_g+\mathbf{u}_l)+\rho_g\frac{\partial \mathbf{u}_g}{\partial t}+\rho_g\mathbf{u}_g.\nabla\mathbf{u}_g+\nabla p=\mathbf{F}_l+\nabla.\tau_\upsilon \Rightarrow$$
$$\rho_g\frac{\partial \mathbf{u}_g}{\partial t}+\rho_g\mathbf{u}_g.\nabla\mathbf{u}_g+\nabla p=\mathbf{F}_l+\nabla.\tau_\upsilon-\sigma \tag{A.11}$$

where $\mathbf{F}_l=-\rho_l\left[\frac{\partial \mathbf{u}_l}{\partial t}+\mathbf{u}_l.\nabla\mathbf{u}_l\right]$ is the momentum equation for the condensed phase, and $\sigma=-\delta\mathbf{u}_l w_l$ is the rate at which momentum is supplied to the newly created gas phase by the gases already present.

Adding $\rho_l\left[\frac{\partial \mathbf{u}_g}{\partial t}+\mathbf{u}_g.\nabla\mathbf{u}_g\right]$ to Equation (A.11) and rearranging the terms one finds

$$\rho\left[\frac{\partial \mathbf{u}_g}{\partial t}+\mathbf{u}_g.\nabla\mathbf{u}_g\right]+\nabla p=\delta\mathbf{F}_l+\nabla.\tau_\upsilon-\sigma \tag{A.12}$$

where $\delta\mathbf{F}_l=-\rho_l\left[\frac{\partial \delta\mathbf{u}_l}{\partial t}+\delta\mathbf{u}_l.\nabla\delta\mathbf{u}_l+\delta\mathbf{u}_l.\nabla\mathbf{u}_g+\mathbf{u}_g.\nabla\delta\mathbf{u}_l\right]$ is the force of interaction between the condensed and gas phases.

With similar manipulations, one can obtain the following energy equation for the temperature of the gas phase,

$$\rho\bar{C}_\upsilon\left[\frac{\partial T_g}{\partial t}+\mathbf{u}_g.\nabla T_g\right]+p\nabla.\mathbf{u}_g=\delta\mathbf{u}_l.\mathbf{F}_l+\tau_\upsilon.\nabla\mathbf{u}_g$$
$$+\mathbf{u}_g.\sigma-\nabla.\mathbf{q}_g+Q+\delta Q_l+w_l\delta e_0 \tag{A.13}$$

where $\delta Q_l=\rho_l\left[\frac{\partial e_l}{\partial t}+\mathbf{u}_l.\nabla e_l\right]$ and $\delta e_0=e_{l0}-e_{g0}$. In analogy to the force interaction between the two phases, we define the heat exchange between the two phases as

$$\delta Q_l=-\rho_l C_l\left[\frac{\partial \delta T_l}{\partial t}+\delta\mathbf{u}_l.\nabla\delta T_l+\delta\mathbf{u}_l.\nabla T_g+\mathbf{u}_g.\nabla\delta T_l\right] \tag{A.14}$$

where $\delta T_l = T_l - T_g$. The mass-averaged specific heat in Equation (A.13) is defined as

$$\bar{C}_\upsilon = \frac{1}{\rho}(\rho_g C_\upsilon + \rho_l C_l) = \frac{C_\upsilon + C_m C_l}{1 + C_m} \tag{A.15}$$

and $C_m = \rho_l / \rho$ is the fraction of mass in unit volume as liquid.

If we drop the subscripts $g$ and the overbars for mass-averaged properties, we can write the conservation equations as follow

- Conservation of Mass: $$\frac{D\rho}{Dt} = -\rho \nabla . \mathbf{u} + \mathcal{W} \tag{A.16}$$

- Conservation of Momentum: $$\rho \frac{D\mathbf{u}}{Dt} = -\nabla p + \mathcal{F} \tag{A.17}$$

- Conservation of Energy: $$\rho C_\upsilon \frac{DT}{Dt} = -p \nabla . \mathbf{u} + \mathcal{Q} \tag{A.18}$$

where

$$\mathcal{W} = -\nabla . (\rho_l \delta \mathbf{u}_l) \tag{A.19}$$

$$\mathcal{F} = \delta \mathbf{F}_l + \nabla . \tau_\upsilon - \sigma \tag{A.20}$$

$$\mathcal{Q} = \delta \mathbf{u}_l . \mathbf{F}_l + \tau_\upsilon . \nabla \mathbf{u} + \mathbf{u} . \sigma - \nabla . \mathbf{q} + Q + \delta Q_l + w_l \delta e_0 \tag{A.21}$$

and the substantial derivative is defined as

$$\frac{D}{Dt} = \frac{\partial}{\partial t} + \mathbf{u} . \nabla \tag{A.22}$$

# REFERENCES


1. Lynch, S., *"Dynamical Systems with Applications using MATLAB®"*. 2004: Birkhauser.

2. Culick, F.E.C. and Yang, V., "*Overview of combustion instabilities in liquid-propellant rocket engines"*. Liquid Rocket Engine Combustion Instability, 1995, AIAA, Washington, DC, USA. p. 3.

3. Higgens, B., *"On the Sound Produced by a Current of Hydrogen Gas Passing Through a Tube"*. Nicholson's J., Vol. 1 (New Series), pp. 129-132, 1802.

4. Rijke, P.L., *"Notice of a New Method of Causing a Vibration of the Air Contained in a Tube Open at Both Ends"*. Phil. Mag., Vol. XVII, pp. 419-422. 1859.

5. Rayleigh, L., *"The Explanation of Certain Acoustic Phenomena",* Royal Institution Proceedings, Vol. VIII, pp. 536-542. 1878.

6. Raun, R.L., et al., *"A Review of Rijke Tubes, Rijke Burners and Related Devices",* Prog. in Comb. Energy and Science, Vol. 19, No. 4, pp. 313-364. 1993.

7. Eckstein, J., *"On the Mechanisms of Combustion Driven Low-Frequency Oscillations in Aero-Engines"*. 2004, Lehrstuhl fur Thermodynamik Technische Universitat Munchen.

8. Williams, F.A., *"Combustion Theory",* 2nd ed. Combustion Science and Engineering Series, Cambridge, Massachusetts: Persues Books. 1985.

9. Crocco, L., "A*spects of Combustion Stability in Liquid Propellant Rocket Motors .1. Fundamentals - Low Frequency Instability with Monopropellants"*. Journal of the American Rocket Society, 1951. **21**(6): p. 163-178.

10. Crocco, L., "A*spects of Combustion Stability in Liquid Propellant Rocket Motors .2. Fundamentals - Low Frequency Instability with Bipropellants - High Frequency Instability"*. Journal of the American Rocket Society, 1952. **22**(1): p. 7-16.

11. Crocco, L. and Cheng, S., "*Theory of Combustion Instability in Liquid Propellant Rocket Motors"*., AGARD Monograph No. 8, Butterworths Scientific Pub., Ltd., London. 1956.

12. Culick, F.E.C., "*Non-Linear Growth And Limiting Amplitude of Acoustic Oscillations in Combustion Chambers"*. Combustion Science and Technology, 1971. **3**(1):

13. Priem, R.J. and D.C. Guentert, *"Combustion Instability Limits Determined by a Nonlinear Theory and a One-Dimensional Model",* NASA TN D-1409, October 1962.

14. Sirignano, W.A., *"A Theoretical Study of Nonlinear Combustion Instability: Longitudinal Mode"*, Department of Aerospace and Mechanical Sciences. 1964, Princeton University.

15. Sirignano, W.A. and L. Crocco, *"A Shock Wave Model of Unstable Rocket Combustors",* AIAA Journal, Vol. 2, No. 7, pp. 1285-1296. 1964.

16. Zinn, B.T. and E.A. Powell, *"Application of the Galerkin Method in the Solution of Combustion Instability Problems",* Proceedings, XIX Congress, International Astronautical Federation. 1968.

17. Harrje, D.T. and F.H. Reardon, "*Liquid Propellant Rocket Combustion Instability"*. NASA Special Publications. 1972.

18. Ljung, L. and P. Lindskog, *"Tools for Semi-physical Modelling",* IFAC System Identification, Copenhagen, Pergamon Press, Oxford. 1199–1204.

19. Bendat, J.S., P.A. Palo, and R.N. Coppolino, "*A general identification technique for nonlinear differential equations of motion"*. Probabilistic Engineering Mechanics, 1992. **7**(1): p. 43-61.

20. Ljung, L., *"System Identification: Theory for the User"*. Second edition, Prentice Hall, Upper Saddle River, NJ, USA, 1999. 1999.

21. Bendat, J.S. and A.G. Piersol, *"Engineering Applications of Correlation and Spectral Analysis"*. Second edition, John Wiley & Sons, New York, USA. 1993.

22. Shih, C.Y., et al., *"Complex mode indication function and its application to spatial domain parameter estimation"*. Mechanical Systems and Signal Processing, 1988. **2**(4): p. 367-377.

23. Cole, H.A., Jr., "*On-line failure detection and damping measurement of aerospace structures by random decrement signatures"*. 1973, NASA

24. Van Overschee, P. and B. De Moor, *"Subspace Identification for Linear Systems: Theory-Implementation-Applications"*. Kluwer Academic Publishers, Dordrecht, The Netherlands. 1996.

25. Peeters, B. and G. De Roeck, "*Stochastic system identification for operational modal analysis: A review"*. Journal of Dynamic Systems Measurement and Control-Transactions of the Asme, 2001. **123**(4): p. 659-667.

26. Roberts, J.B. and M. Vasta, *"Markov modelling and stochastic estimation for non-linear ship rolling in irregular seas"*. Phil. Trans. R. Soc. London, 2000. **358**: p. 1917-1941.

27. Roberts, J.B. and M. Vasta, "*Energy based stochastic estimation of nonlinear oscillators with parametric random excitation".* Meccanica, 2002. **37**(1-2): p. 33-49.

28. Rudinger, F. and S. Krenk, "*Identification of nonlinear oscillator with parametric white noise excitation".* Nonlinear Dynamics, 2004. **36**(2-4): p. 379-403.

29. Agarkov, A.F., et al., *"Injector Flame Stabilization Efeects on Combustion Instability".* 1st International Symposium on Liquid Rocket Combustion Instabilities, Pennsylvania State University, AIAA Progress Series, Vol. 169. 1993.

30. Karmalita, V.A. and V.I. Furletov, "*Autoregression Method for Determining the Decrement and Frequency of the Natural Oscillations of a Gas in a Combustion-Chamber".* Combustion Explosion and Shock Waves, 1987. **23**(6): p. 694-700.

31. Pandit, S.M. and S.M. Wu, *"Time Series and Systems Analysis with Application".* 1 ed. 1983: Krieger Publishing Company. 586.

32. Box, G. E. P., Jenkins, G. M., and Reinsel, G. M., *"Time Series Analysis: Forecasting and Control"*, Wiley Series in Probability and Statistics, Wiley & Sons, 4th edition, 2008.

33. Lieuwen, T., "*Online combustor stability margin assessment using dynamic pressure data".* Journal of Engineering for Gas Turbines and Power-Transactions of the Asme, 2005. **127**(3): p. 478-482.

34. Murugappan, S., et al., *"Optimal Control of a Swirl Stabilized Spray Combustor using System Identification Approach"*, Combustion Science and Technology, 175(1): p.55–81, 2003.

35. Cammarata, L., A. Fichera, and A. Pagano, "*Neural prediction of combustion instability".* Applied Energy, 2002. **72**(2): p. 513-528.

36. Dunstan, W.J., R.R. Bitmead, and S.M. Savaresi, "*Fitting nonlinear low-order models for combustion instability control".* Control Engineering Practice, 2001. **9**(12): p. 1301-1317.

37. Savaresi, S.M., R.R. Bitmead, and W.J. Dunstan, "*Non-linear system identification using closed-loop data with no external excitation: the case of a lean combustion chamber".* International Journal of Control, 2001. **74**(18): p. 1796-1806.

38. Santavicca, D.A. and J.G. Lee, *"Experimental Diagnostics of Combustion Instabilities"*, in *Combustion Instabilities in Gas Turbine Engines*, AIAA, Editor. 2005. p. 481-532.

39. Conrad, T., et al. "*Control of the stability margin in a liquid fueled combustor using a "smart" fuel injector".* 2006. Sacramento, CA, United States: American Institute of Aeronautics and Astronautics Inc.

40. Jones, R.E., et al., *"Combustion Gas Properties - I - ASTM Jet A Fuel and dry Air"*. NASA Technical Paper 2359, October. 1984.

41. Burnley, V.S., *"Nonlinear Combustion Instabilities and Stochastic Sources"*, in *Aeronautics Dept*. 1996, California Institute of Technology: Pasadena, CA.

42. Culick, F.E.C., "*Nonlinear Behavior Of Acoustic Waves In Combustion Chambers - I"*. Acta Astronautica, 1976. **3**(9-10): p. 715-734.

43. Culick, F.E.C., "*Nonlinear Behavior Of Acoustic Waves In Combustion Chambers - Ii"*. Acta Astronautica, 1976. **3**(9-10): p. 735-757.

44. Powell, E.A. and B.T. Zinn, "*Theoretical Investigation of Nonlinear 3 Dimensional Instabilities in Liquid Rockets with Real Nozzles"*. Acta Astronautica, 1974. **1**(7-8): p. 1051-1073.

45. Chu, B.-T. and L.S.G. Kovasznay, *"Nonlinear Interactions in a Viscous heat-conducting compressible gas."* Journal of Fluid Mechanics, 1957. **3**: p. 494-512.

46. Wicker, J.M., M.W. Yoon, and V. Yang, "*Linear and Nonlinear Pressure Oscillations in Baffled Combustion-Chambers"*. Journal of Sound and Vibration, 1995. **184**(1): p. 141-171.

47. Zhu, W. and Y.K. Lin, *"Stochastic averaging of energy envelope"*. Journal of Engineering Mechanics, 1991. **117**: p. 1890-1905.

48. Wong, E. and M. Zakai, *"On the Relation between Ordinary and Stochastic Differentail Equations"*. International Journal of Engeering Science, 3, pp.213-229. 1965.

49. Rudinger, F. and S. Krenk, "*Non-parametric system identification from non-linear stochastic response"*. Probabilistic Engineering Mechanics, 2001. **16**(3): p. 233-243.

50. Higham, D.J., *"An algorithmic introduction to numerical simulation of stochastic differential equations"*. SIAM Journal of Numerical Analysis, 2001. **43**(3): p. 525-546.

51. Andersen, P., *"Identification of Civil Engineering Structures Using Vector ARMA Models"*, in Department of Building Technoloy and Structural Engineering. 1997, Aalborg University, Denmark.

52. Bendat, J.S. and A.G. Piersol, *"Random Data - Analysis and Measurement Procedures."* John Wiley & Sons, 1986. 1986.

53. Melsa, J.L. and A.P. Sage, *"An Introduction to Probability and Stochastic Processes"*. Prentice-Hall Inc. 1973.

54. Asmussen, J.C., R. Brincker, and S.R. Ibrahim, "*Statistical theory of the vector random decrement technique"*. Journal of Sound and Vibration, 1999. **226**(2): p. 329-344.

55. Fleifil, M., et al., *"Response of a laminar premixed flame to flow oscillations: A kinematic model and thermoacoustic instability result"*. Combustion and Flame, 106:487–510. 1996.

56. Peracchio, A.A. and W.M. Proscia, "*Nonlinear heat-release/acoustic model for thermoacoustic instability in lean premixed combustor"*. Journal of Engineering for Gas Turbines and Power-Transactions of the Asme, 1999. **121**(3): p. 415-421.

57. Dowling, A.P., *"Nonlinear sef-excited Oscillations of a ducted flame"*. J. Fluid Mech., vol. 346, pp. 271-290. 1997.

58. Annaswamy, A.M., et al., *"Impact of linear coupling on the design of active controllers for thermoacoustic instability"*. Combustion Science and Technology, 128:131–180. 1997.

59. Rumsey, J.W., et al., *"Low-order Nonlinear Models of Thermoacoustic Instabilities and Model-based Control"*. Proceedings of the 1998 IEEE International Conference on Control Applications, Trieste, Italy 1-4 September. 1998.

60. Annaswamy, A.M., et al., *"An input-output model of thermoacoustic instability and active control design"*. Technical Report 9705, Adaptive Control Laboratory, Department of Mechanical Engineering, M.I.T. , July. 1997.

61. Saunders, W.R., et al., *"Analytical and Practical Considerations for Control of Thermoacoustic Instabilities"*. AIAA Paper 99-0718. 1999.

62. Jazwinski, A.H., *"Stochastic Processes and Filtering Theory". Academic Press, New York, USA*. 1970.

63. Bouziani, F., et al. "*An analytically tractable model for combustion instability*". Decision and Control, and European Control Conference. CDC-ECC '05. 44th IEEE Conference on 2005.

64. Flandro, G.A., J. Majdalani, and J.D. Sims, "*On Nolinear Combustion Instability in Liquid Propellant Rocket Engines"*, 40th AIAA/ASME/SAE/ASEE Joint Propulsion Conference and Exhibit., AIAA, Editor. 2004: Fort Lauderdale, FL.

65. Lubarsky, E. and B.T. Zinn, *"Heat Release Distribution in the LRE Combustor Simulator Operating in Stable and Unstable Modes"*, 46th Aerospace Meeting & Exhibition., AIAA, Editor. 2008: Reno, NV.

66. Govaerts, W., et al., *"MATCONT and CL MATCONT: Continuation toolboxes in MATLAB®"*. 2006.